

**ÉCOLE DOCTORALE MATHÉMATIQUES, SCIENCES DE L'INFORMATION ET DE  
L'INGÉNIEUR – ED269**

**Laboratoire des sciences de l'Ingénieur, de l'Informatique  
et de l'Imagerie (UMR 7357)**

**THÈSE** présentée par :

**Shuting ZHANG**

soutenue le : **16 Décembre 2024**

pour obtenir le grade de : **Docteur de l'université de Strasbourg**

Discipline/ Spécialité : Sciences de l'Imagerie / Télédétection

**Angular Effects of Surface Brightness  
Temperature Observed from Sentinel-  
3A/SLSTR Data**

**THÈSE dirigée par :**

**M. Zhao-Liang LI**

**Mme. Françoise NERRY**

Directeur de recherche, CNRS, France

Directeur de recherche, CNRS, France

**RAPPORTEURS :**

**M. José Antonio SOBRINO**

**Mme. Caixia GAO**

Professeur, Université de Valencia, Espagne

Professeur, CAS, Chine

**AUTRES MEMBRES DU JURY :**

**M. Hua WU**

**Mme. Jélila LABED**

Professeur, UESTC, Chine

Maître de Conférence, UdS, France

## Acknowledgements

First, I would like to express my sincere appreciation and deep respect to my supervisor Dr. Zhao-Liang LI. During my doctoral studies, I faced many challenges and difficulties. I got professional instructions and patient suggestions from him. His wide academic perspective, rigorous research spirit and open-minded personality impressed me so much. Dr. Li and his wife Dr. Zhao also helped me a lot in my daily life and helped me adapt to the environment here. And I also want to give my appreciation to my supervisor Dr. François NERRY. She is so kind and provided many useful suggestions for my research. Her suggestions are valuable to the completion of this thesis. Without her help and encouragement, it would be difficult for me to complete my work.

Second, I am also grateful to Dr. Hua WU, Dr. Caixia Gao, Dr. Jélila LABED and Dr José Antonio SOBRINO for participating in my defense presentation and giving professional advices and kind wishes. And I want to thank Dr. Jihad ZALLAT, Dr. Hervé YÉSOU, Dr. Jean REHBINDER for all the support since I joined the lab.

I would also like to thank all the friends and students I met here in Strasburg: Jing LI, Lei HE, Yanru Yu, Yongxin HU, Hongyu LI, Chen RU, Lirong DING, Xinming ZHU, Qiang LI, Xiaolin ZHU, Fangjie LI, Qianyu LIAO, Shilei LI, Meng LIU, Yitao LI, Yue MA, Shengya GUO, Jiahao LI, Xiaokang HU, Josef WAGNER, Zihao WU and Renato CIFUENTES. With them, it is a journey with cheer and fun in this foreign city.

Special thanks are given to my parents. They are supportive and encouraging of every decision as they always did in the past decades. They are my strongest backing, giving unconditional and selfless love to me in my whole life. Specific thanks are also presented to my husband Dr. Cheng HUANG. It is difficult to make through the years of separation but fortunately we made it with our love and understanding of each other.

It is difficult to quote every name in this section. I appreciate everyone who has provided help in my life. I wish them all the luck.

# Contents

Acknowledgements.....	I
Contents .....	II
List of abbreviations .....	IV
List of figures.....	VIII
List of tables.....	XIII
Résumé.....	XIV
1.Introduction.....	1
1.1 Background.....	1
1.1.1 The algorithms of LST retrieval from satellite TIR data .....	2
1.1.2 The angular effect of brightness temperature .....	7
1.2 Objective and structure of this thesis .....	11
2. Description of data used.....	13
2.1 Sentinel-3A data.....	13
2.2 MCD12Q1 data.....	17
2.3 SRTM data.....	19
2.4 Emissivity spectra database .....	19
2.5 Thermodynamic Initial Guess Retrieval (TIGR) database .....	21
2.6 Köppen-Geiger climate classification map.....	22
2.7 ESA climate change initiative plus soil moisture .....	23
3. Surface brightness temperature retrieval algorithm on Sentinel-3A satellite .....	25
3.1 Development of SW algorithm .....	25
3.2 Establishment of simulation database .....	27
3.3 Determination of SW coefficients for Sentinel-3A SLSTR .....	33
3.4 Uncertainty evaluation in surface brightness temperature.....	35
3.4.1 Uncertainty evaluation resulting from the retrieval model.....	35
3.4.2 Uncertainty evaluation resulting from noise in TOA brightness temperature .....	36
4. Angular effects of surface brightness temperatures observed from SLSTR data....	38
4.1 Study area.....	38
4.1.1 Sites selection.....	38
4.1.2 The location of the study area .....	39
4.2 Results of angular effects of surface brightness temperature .....	42

4.2.1 Land cover types .....	43
4.2.2 Season .....	64
4.2.3 Latitude .....	68
4.2.4 Solar zenith angle.....	70
4.2.5 Climate.....	72
4.3 Causality of angular effects of surface brightness temperature .....	76
4.3.1 Methodology .....	77
4.3.2 Data processing .....	80
4.3.3 Results.....	81
4.3.3.1 The contribution of different factors on $\Delta T_g$ .....	81
4.3.3.2 The influence of the interaction between two determinants on $\Delta T_g$ ....	83
4.3.3.3 Identification of sensitive areas of $\Delta T_g$ influenced by various factors	86
4.4 Conclusion .....	93
5. Conclusions and prospectives .....	96
5.1 The conclusions .....	96
5.2 Prospective.....	97
Reference .....	100
Résumé.....	107
Résumé en anglais.....	107

## List of abbreviations

LST	Land surface temperature
ESA	European Space Agency
CCI	Climate Change Initiative
ECV	Essential Climate Variables
TIR	Thermal infrared
AVHRR	Advanced Very High Resolution Radiometer
VIIRS	Visible Infrared Imaging Radiometer Suite
NOAA	National Oceanic and Atmospheric Administration
TM	Thematic Mapper
ETM+	Enhanced Thematic Mapper Plus
TIRS	Thermal InfraRed Sensor
ATSR	Along Track Scanning Radiometer
ERS	European Remote-Sensing Satellite
MODIS	Moderate-resolution Imaging Spectroradiometer
AATSR	Advanced Along-Track Scanning Radiometer
SEVIRI	Spinning Enhanced Visible and InfraRed Imager
MSG	Meteosat Second Generation
SLSTR	Sea and Land Surface Temperature Radiometer
AHI	Advanced Himawari Imager
VIMS	Visual and Infrared Multispectral Sensor
GF 5	Gao-Fen 5
ECOSTRESS	ECOsystem Spaceborne Thermal Radiometer Experiment on Space Station
ISS	International Space Station
VIRR	Visible and InfraRed Radiometer
AGRI	Advanced Geostationary Radiation Imager
FY	Chinese Fengyun
SC	Single-channel
SW	Split-window
DA	Dual-angle
TES	Temperature and emissivity separation

D/N	Day/night
VZA	Viewing zenith angle
ASTER	Advanced Spaceborne Thermal Emission Reflection Radiometer
GED	Global Emissivity Dataset
RTE	Radiative transfer equation
NEM	Normalization emissivity method
SR	Spectral ratio
MMD	Maximum-minimum apparent emissivity difference method
MIR	Mid-Infrared
TISI	Temperature independent spectral index
MAOS	Multi-Angle Observation System
BRF	Bi-directional reflectance factor
WIDAS	Wide-angle Infrared Dual-model line/area Array Scanner
UAVs	Unmanned aerial vehicles
MSG	Meteosat Second Generation
GMES	Global Monitoring for Environmental Security
OLCI	Ocean and Land Color Instrument
SRAL	SAR Radar ALtimeter
VNIR	Visible and near-infrared
SWIR	Shortwave infrared
TOA	Top of the atmosphere
GLT	Geographic lookup table
EOS	Earth Observing System
LCCS	Land Cover Classification System
SRTM	Shuttle Radar Topographic Mission
NGA	United States Department of Defense's National Mapping Agency
X-SAR	X-Band Synthetic Aperture Radar
USGS	U.S. Geological Survey
JHU	Johns Hopkins University
JPL	Jet Propulsion Laboratory
NPV	Non-photosynthetic vegetation
LSE	Land surface emissivity
TIGR	The Thermodynamic Initial Guess Retrieval

WVC	Water vapor content
T0	Atmospheric temperature
MAT	Mean annual air temperature
MAP	Mean annual precipitation
SM	Soil Moisture
AMI-WS	Active Microwave Instrument Wind Scatterometer
ASCAT	Advanced Scatterometer
SMMR	Scanning Multi-channel Microwave Radiometer
SSM/I	Special Sensor Microwave Imager
AMSR-E	Advanced Microwave Scanning Radiometer for EOS
SMAP	Soil Moisture Active Passive
WGS 84	World Geodetic System 1984
MODTRAN	MODERate resolution atmospheric TRANsmission
AFRL	US Air Force Research Laboratory
SSI	Spectrum Sciences Inc.
MLS	Mid-Latitude Summer
MLW	Mid-Latitude Winter
SAS	Sub-Arctic Summer
SAW	Sub-Arctic Winter
RMSE	Root-mean-square error
ENF	Evergreen needleleaf forests
EBF	Evergreen broadleaf forests
DBF	Deciduous broadleaf forests
MF	Mixed forests
OSH	Open shrublands
WSA	Woody savannas
SVA	Savannas
GRA	Grasslands
WET	Permanent wetlands
CRO	Croplands
URB	Urban and built-up lands
CVM	Cropland/natural vegetation mosaic
SNO	Snow and ice

BSV	Barren or sparsely vegetated
LULC	Land use/land cover
SZA	Solar zenith angle

## List of figures

Fig 1.1 Structure chart of the dissertation.....	12
Fig 2.1 Structure of Sentinel-3 Satellite (Credits: European Satellite Agency). .....	13
Fig 2.2 Track and scanning parameters of the Sentinel-3 SLSTR instrument with the nadir and oblique view (Credits: European Satellite Agency).....	14
Fig 2.3 The spectral response functions at SLSTR S8 and S9.....	16
Fig 2.4 53 Selected emissivity spectra from ECOSTRESS spectral library.....	20
Fig 2.5 Scatterplot of WVC and $T_0$ in the first boundary layer of 60 selected atmospheric profiles. ....	22
Fig 2.6 The Köppen-Geiger climate classification map in five main climate types (tropical, arid, temperate, cold, and polar climates). ....	23
Fig 3.1 Temperature profiles of the MODTRAN model atmospheres .....	28
Fig 3.2 the soil emissivity in the two thermal infrared channels of the SLSTR. The black and red dots represent the soil emissivity at 10.85 $\mu$ m and 12 $\mu$ m, respectively. ....	30
Fig 3.3 Flowchart of generating a simulated dataset .....	30
Fig 3.4 Example of tp5 file .....	32
Fig 3.5 Example of tp7 file .....	33
Fig 3.6 Scatter plots of actual and estimated surface brightness temperature at nadir view (a) and oblique view (b) .....	34
Fig 3.7 Scatter plots of WVC and actual surface brightness temperature. ....	34
Fig 4.1 Geolocation of the selected 42 study sites.....	39
Fig 4.2 Total available scenes of SLSTR Level1 data for each month.....	41
Fig 4.3 (a) Geographic distribution of the study sites. (b-d) Violin plots of the $\Delta T_g$ in evergreen needleleaf forests (ENF) during the day from September 2019 to August 2020. The violins present the distribution of the $\Delta T_g$ with density curves. The upper and lower sides of the black rectangle present the third quartile and first quartile, respectively. The black horizontal line in rectangle indicates the median. The red dotted line represents the mean. The upper and lower boundaries are the maximum and minimum values, respectively. ....	44
Fig 4.4 (a) Geographic distribution of the study sites. (b-d) Violin plots of the $\Delta T_g$ in evergreen broadleaf forests (EBF) during the day from September 2019 to August 2020.....	45

Fig 4.5 (a) Geographic distribution of the study sites. (b-d) Violin plots of the $\Delta T_g$ in deciduous broadleaf forests (DBF) during the day from September 2019 to August 2020.....	46
Fig 4.6 (a) Geographic distribution of the study sites. (b-d) Violin plots of the $\Delta T_g$ in mixed forests (MF) during the day from September 2019 to August 2020.....	46
Fig 4.7 (a) Geographic distribution of the study sites. (b-d) Violin plots of the $\Delta T_g$ in open shrublands (OSH) during the day from September 2019 to August 2020. .	47
Fig 4.8 (a) Geographic distribution of the study sites. (b-d) Violin plots of the $\Delta T_g$ in woody savannas (WSA) during the day from September 2019 to August 2020.	48
Fig 4.9 (a) Geographic distribution of the study sites. (b-d) Violin plots of the $\Delta T_g$ in savannas (SVA) during the day from September 2019 to August 2020.....	49
Fig 4.10 (a) Geographic distribution of the study sites. (b-d) Violin plots of the $\Delta T_g$ in grasslands (GRA) during the day from September 2019 to August 2020. ....	50
Fig 4.11 (a) Geographic distribution of the study sites. (b-d) Violin plots of the $\Delta T_g$ in permanent wetlands (WET) during the day from September 2019 to August 2020. ....	51
Fig 4.12 (a) Geographic distribution of the study sites. (b-d) Violin plots of the $\Delta T_g$ in croplands (CRO) during the day from September 2019 to August 2020. ....	52
Fig 4.13 (a) Geographic distribution of the study sites. (b-d) Violin plots of the $\Delta T_g$ in urban and built-up lands (URB) during the day from September 2019 to August 2020.....	52
Fig 4.14 (a) Geographic distribution of the study sites. (b-d) Violin plots of the $\Delta T_g$ in cropland/natural vegetation mosaic (CVM) during the day from September 2019 to August 2020.....	53
Fig 4.15 (a) Geographic distribution of the study sites. (b-d) Violin plots of the $\Delta T_g$ in snow and ice (SNO) during the day from September 2019 to August 2020. ....	54
Fig 4.16 (a) Geographic distribution of the study sites. (b-d) Violin plots of the $\Delta T_g$ in barren or sparsely vegetated (BSV) during the day from September 2019 to August 2020.....	55
Fig 4.17 (a) Geographic distribution of the study sites. (b-d) Violin plots of the $\Delta T_g$ in evergreen needleleaf forests (ENF) during the night from September 2019 to August 2020.....	56

Fig 4.18 (a) Geographic distribution of the study sites. (b-d) Violin plots of the  $\Delta T_g$  in evergreen broadleaf forests (EBF) during the night from September 2019 to August 2020. ....56

Fig 4.19 (a) Geographic distribution of the study sites. (b-d) Violin plots of the  $\Delta T_g$  in deciduous broadleaf forests (DBF) during the night from September 2019 to August 2020. ....57

Fig 4.20 (a) Geographic distribution of the study sites. (b-d) Violin plots of the  $\Delta T_g$  in mixed forests (MF) during the night from September 2019 to August 2020. ....57

Fig 4.21 (a) Geographic distribution of the study sites. (b-d) Violin plots of the  $\Delta T_g$  in open shrublands (OSH) during the night from September 2019 to August 2020. ....58

Fig 4.22 (a) Geographic distribution of the study sites. (b-d) Violin plots of the  $\Delta T_g$  in woody savannas (WSA) during the night from September 2019 to August 2020. ....59

Fig 4.23 (a) Geographic distribution of the study sites. (b-d) Violin plots of the  $\Delta T_g$  in savannas (SVA) during the night from September 2019 to August 2020. ....59

Fig 4.24 (a) Geographic distribution of the study sites. (b-d) Violin plots of the  $\Delta T_g$  in grasslands (GRA) during the night from September 2019 to August 2020. ....60

Fig 4.25 (a) Geographic distribution of the study sites. (b-d) Violin plots of the  $\Delta T_g$  in permanent wetlands (WET) during the night from September 2019 to August 2020. ....61

Fig 4.26 (a) Geographic distribution of the study sites. (b-d) Violin plots of the  $\Delta T_g$  in croplands (CRO) during the night from September 2019 to August 2020. ....62

Fig 4.27 (a) Geographic distribution of the study sites. (b-d) Violin plots of the  $\Delta T_g$  in urban and built-up lands (URB) during the day from September 2019 to August 2020. ....62

Fig 4.28 (a) Geographic distribution of the study sites. (b-d) Violin plots of the  $\Delta T_g$  in cropland/natural vegetation mosaic (CVM) during the night from September 2019 to August 2020. ....63

Fig 4.29 (a) Geographic distribution of the study sites. (b-d) Violin plots of the  $\Delta T_g$  in snow and ice (SNO) during the night from September 2019 to August 2020. ....63

Fig 4.30 (a) Geographic distribution of the study sites. (b-d) Violin plots of the  $\Delta T_g$  in barren or sparsely vegetated (BSV) during the night from September 2019 to August 2020. ....64

Fig 4.31 The bar chart of the  $\Delta T_g$  in different seasons during daytime at northern hemisphere: (a) spring, (b) summer, (c) autumn, and (d) winter. The length of the blue rectangle represents the mean value, and half the length of the black line represents the standard deviation. ....65

Fig 4.32 The bar chart of the  $\Delta T_g$  in different seasons during nighttime at northern hemisphere: (a) spring, (b) summer, (c) autumn, and (d) winter. The length of the blue rectangle represents the mean value, and half the length of the black line represents the standard deviation. ....66

Fig 4.33 The bar chart of the  $\Delta T_g$  in different seasons during daytime at southern hemisphere: (a) spring, (b) summer, (c) autumn, and (d) winter. The length of the blue rectangle represents the mean value, and half the length of the black line represents the standard deviation. ....67

Fig 4.34 The bar chart of the  $\Delta T_g$  in different seasons during nighttime at southern hemisphere: (a) spring, (b) summer, (c) autumn, and (d) winter. The length of the blue rectangle represents the mean value, and half the length of the black line represents the standard deviation. ....68

Fig 4.35 Variation of mean and standard deviation of  $\Delta T_g$  at northern and southern hemisphere, respectively. The points show the mean value of  $\Delta T_g$  in high-, mid-, low-latitude at northern and southern hemisphere, respectively. And the shaded upper and lower ends are the range of mean  $(\Delta T_g) \pm \text{STD}$ . ....69

Fig 4.36 Heatmap of the mean and standard deviation of  $\Delta T_g$  during (a) daytime and (b) nighttime in high-, mid-, low-latitude at northern and southern hemisphere, respectively. Color represents standard deviation, circle indicates the mean value of  $\Delta T_g$ , and triangle means no value. ....70

Fig 4.37 Variation of mean and standard deviation of  $\Delta T_g$  at different solar zenith angles. The triangles show the mean value of  $\Delta T_g$  in each  $10^\circ$  interval of the solar zenith angles, and the color-shaded bands upper and lower are the range of mean  $(\Delta T_g) \pm \text{STD}$ . ....71

Fig 4.38 A density plot of solar zenith angle and  $\Delta T_g$  in high-, mid-, low-latitude, for (a), (c), (e) at northern and for (b), (d), (f) southern hemisphere, respectively. Red

indicates a higher distribution density of  $\Delta T_g$ , while blue indicates a lower distribution density of  $\Delta T_g$ . .....72

Fig 4.39 Mean  $\Delta T_g$  of tropical during daytime and nighttime, for (a) and (b) at northern hemisphere, and for (c) and (d) at southern hemisphere, respectively. ....73

Fig 4.40 Mean  $\Delta T_g$  of arid during daytime and nighttime, for (a) and (b) at northern hemisphere, and for (c) and (d) at southern hemisphere, respectively. ....74

Fig 4.41 Mean  $\Delta T_g$  of temperate during daytime and nighttime, for (a) and (b) at northern hemisphere, and for (c) and (d) at southern hemisphere, respectively..75

Fig 4.42 Mean  $\Delta T_g$  of cold during daytime and nighttime, for (a) and (b) at northern hemisphere. ....76

Fig 4.43 Mean  $\Delta T_g$  of polar during daytime and nighttime, for (a) and (b) at northern hemisphere, and for (c) and (d) at southern hemisphere, respectively. ....76

Fig 4.44 Flow chart for the analysis on the determinants of  $\Delta T_g$ .....80

Fig 4.45 The contribution of the selected determinants to  $\Delta T_g$ . ....83

Fig 4.46 Interactions between determinants of spatial differentiation on  $\Delta T_g$ , (a) and (b) for daytime of northern/southern hemisphere, (c) and (d) for nighttime of northern/southern hemisphere, respectively. ....86

Fig 4.47 Mean values of  $\Delta T_g$  in different subregions for each determinant during daytime at northern hemisphere.....88

Fig 4.48 Mean values of  $\Delta T_g$  in different subregions for each determinant during daytime at southern hemisphere.....89

Fig 4.49 Mean values of  $\Delta T_g$  in different subregions for each determinant during nighttime at northern hemisphere. ....91

Fig 4.50 Mean values of  $\Delta T_g$  in different subregions for each determinant during nighttime at southern hemisphere. ....92

## List of tables

Table 2.1 Specifications of SLSTR sensor. ....	15
Table 2.2 Land cover types and their description by IGBP classification strategy in MCD12Q1 product. ....	18
Table 2.3 Climate classes and their defining criteria. ....	23
Table 3.1 The coefficients of SW algorithm at nadir and oblique view .....	34
Table 4.1 Detailed information of the selected 42 study sites. ....	40
Table 4.2 Information of available SLSTR Level1 data of the selected 42 study sites. .....	42
Table 4. 3 Determination of the interaction type between two independent variables and the dependent variable. ....	78
Table 4.4 Discrete intervals of dependent variables .....	81
Table 4.5 Statistics on the contribution of individual factor to $\Delta T_g$ .....	83

## Résumé

La température de la surface terrestre (LST) est une variable clé en météorologie et en géosciences. Elle est fréquemment utilisée pour évaluer les processus d'échange entre la surface terrestre et l'atmosphère, contraindre les bilans énergétiques de surface, estimer l'évapotranspiration et surveiller le changement climatique à l'échelle mondiale et régionale (Anderson et al., 2012, Li et al., 2022). Dans le cadre du projet Climate Change Initiative (CCI) de l'Agence spatiale européenne (ESA), la LST est l'un des indicateurs des variables climatiques essentielles (ECV) (Malakar et al., 2018). Elle est également précieuse pour l'étude des îlots de chaleur urbains, la gestion de la production agricole, ainsi que la prévision et la surveillance des risques naturels.

L'étude de l'utilisation des données satellitaires pour obtenir la température de surface a commencé au début des années 1960. La télédétection par satellite est le seul moyen possible d'obtenir une LST précise avec une résolution spatiale et temporelle élevée à l'échelle régionale et mondiale (Li et al., 2013). Au cours des décennies suivantes, nombre de capteurs infrarouges thermiques (TIR) capables de détecter la température de surface ont été intégrés sur différents satellites avec une bonne performance. Bien que de nombreux produits LST de satellites en orbite polaire obtenus par les capteurs susmentionnés soient déjà disponibles pour les utilisateurs, la variation des angles d'observation pendant le balayage du satellite introduit des différences directionnelles dans le rayonnement thermique de surface. La plupart des recherches sur la directionnalité du rayonnement thermique sont basées sur des expériences menées à partir de plates-formes terrestres ou aériennes. En ajustant les angles d'observation, ces études acquièrent des données sur la température de brillance et analysent les variations de la température de brillance de la surface. Généralement, la directionnalité des surfaces homogènes est attribuée à l'émissivité. Cependant, la principale limite de ces études est que les données ne peuvent être acquises que pour de courtes durées et sur de petites zones. Étant donné que la température de brillance de la surface change continuellement en fonction des conditions atmosphériques et de l'éclairement, les données satellitaires acquises à différents moments ne peuvent pas être directement utilisées pour analyser les effets angulaires sur la température de brillance de la surface. Par conséquent, il y a moins d'observations directes à partir de plates-formes satellitaires. Sentinel-3A/SLSTR, cependant, peut fournir des observations en temps réel à grande échelle, à long terme et sous plusieurs angles, ce qui le rend

particulièrement adapté à l'étude des effets angulaires sur la température de brillance de la surface. La recherche sur les effets angulaires devrait permettre d'améliorer encore la précision de l'extraction de la température de surface.

Depuis les années 1970, les chercheurs ont proposé diverses hypothèses et méthodes pour explorer les méthodes d'extraction de la LST dans le TIR. Les algorithmes d'extraction de la LST les plus largement utilisés à l'heure actuelle comprennent l'algorithme à canal unique (SC), l'algorithme split-window (SW), l'algorithme à double angle (DA), l'algorithme de séparation de la température et de l'émissivité (TES) et l'algorithme jour/nuit (D/N). L'algorithme split-window a été utilisé pour estimer la LST dans cette étude, en raison de sa simplicité, de sa grande efficacité et de son efficacité dans les corrections atmosphériques. Une autre raison est que l'algorithme split-window est sensible à la variété de l'angle zénithal d'observation, ce qui en fait une méthode adaptée pour évaluer l'influence des effets d'angle sur la température de brillance de la surface terrestre.

Sur la base de l'algorithme précédent de détermination de la LST, une hypothèse typique est que la surface terrestre présente une émission thermique isotrope. En raison de la présence généralisée de pixels mixtes hétérogènes et non isothermes à la surface de la Terre, le rayonnement thermique de surface présente des caractéristiques directionnelles significatives. Les caractéristiques directionnelles du rayonnement thermique de surface ont été observées la première fois par Fuchs et al. (1967) lors d'une expérience sur le terrain, où les températures de surface des cultures en rangées observées sous différents angles variaient de 1 à 3 K, ce qui indiquait un effet angulaire évident. Depuis lors, au cours des dernières décennies, les scientifiques ont utilisé des capteurs TIR à bord de diverses plateformes d'observation pour étudier la directionnalité du rayonnement thermique sur différents types de surfaces et de structures. Ces études ont confirmé l'effet angulaire sur la température de brillance de la surface. Actuellement, seuls les capteurs de la série ATSR (ATSR-1, ATSR-2, AATSR, SLSTR) fournissent des observations en temps réel à différents angles ( $0^\circ$  et  $55^\circ$ ). Li et al. (2001) ont analysé une image ATSR-2 et ont constaté que la variation angulaire de la température de brillance au sol est très sensible aux incertitudes atmosphériques, la méthode SW démontrant une plus grande précision par rapport à la méthode SC. Coll et al. (2019) ont utilisé les données AATSR pour étudier les différences de température de brillance entre les observations au nadir et à l'avant,

constatant qu'au-dessus des terres, la différence maximale se produit en été, atteignant environ 8 K, tandis que les différences de température de brillance à la surface de la mer étaient plus petites et moins variables dans le temps et la saison.

Sentinel-3A/SLSTR peut acquérir des données d'observation multi angulaires en temps quasi réel, ce qui permet d'étudier les effets angulaires de la température de surface. L'étude des effets angulaires devrait permettre d'améliorer la précision de l'extraction de la température de la surface terrestre. Cette recherche adopte les données SLSTR TIR comme source principale de données et obtient la température de brillance de la surface en utilisant l'algorithme SW pour analyser l'effet angulaire de la température de brillance de la surface. Le schéma principal est le suivant :

(1) Générer une base de données simulée et déterminer l'algorithme SW pour obtenir la température de brillance de surface.

(2) Comparer les différences de températures de brillance de surface entre les vues nadir et obliques obtenues à partir des données SLSTR de la sonde sentinelle-3A.

(3) Analyser les facteurs possibles pour expliquer les effets angulaires des températures de brillance de surface entre les observations nadir et obliques.

Le second chapitre est consacré aux données utilisées dans cette étude. Les données de Sentinel-3A ont été utilisées pour déterminer la température de surface au nadir et en vue oblique. Sentinel-3A a été lancé le 16 février 2016 dans le cadre d'une mission importante du programme GMES (Global Monitoring for Environmental Security). Le capteur SLSTR à bord de Sentinel-3A est un radiomètre imageur à balayage conique, hérité de la série d'instruments (A)ATSR. L'instrument SLSTR est conçu avec deux angles d'observation indépendants : le nadir et un angle zénithal de 55°. La fauchée au nadir est d'environ 1400 km, tandis que la fauchée oblique est d'environ 740 km. L'instrument SLSTR comprend neuf canaux, qui s'étendent des longueurs d'onde du visible à l'infrarouge thermique, dont trois canaux dans le visible et le proche infrarouge (VNIR), trois canaux dans l'infrarouge à ondes courtes (SWIR) et trois canaux MIR/TIR (centrés sur 0,555, 0,659, 0,865, 1,375, 1,610, 2,25, 3,74, 10,85, et 12,0  $\mu\text{m}$ ). Dans cette thèse, les deux derniers canaux TIR ont été utilisés pour obtenir la température de brillance de la surface.

Le produit SLSTR de niveau 1 d'octobre 2019 à septembre 2020 a été sélectionné pour récupérer et analyser l'effet angulaire sur la température de brillance de surface. Les flags de nuages extraits des données SLSTR niveau 1 ont été utilisés pour

sélectionner les données sans nuages dans une plage de 3×3 km. Seules les données de haute qualité (valeur = 0) ont été utilisées. Nous avons téléchargé 27352 scènes diurnes et 27384 scènes nocturnes. Le produit SLSTR niveau 1 n'ayant pas été corrigé géométriquement, les images de chaque bande doivent subir une correction géométrique basée sur la table de recherche géographique (GLT) avant d'extraire la température de brillance de surface.

Le jeu de données MCD12Q1, un produit MODIS Level 3 land cover type généré à partir des observations des satellites Terra et Aqua à une résolution spatiale de 500 m, a été utilisé dans cette thèse pour identifier les zones d'étude. Les données de la Shuttle Radar Topographic Mission (SRTM) ont été utilisées dans cette étude pour obtenir des données d'élévation globales et pour filtrer l'uniformité de l'élévation. Dans cette étude, la bibliothèque spectrale ECOSTRESS version 1.0 a été utilisée pour déterminer les émissivités pour la base de données de simulation. Au total, 53 spectres ont été sélectionnés (41 échantillons de sol, 4 échantillons de végétation et 8 échantillons d'étendues d'eau, de neige et de glace) pour obtenir l'émissivité de la surface terrestre (LSE). La base de données Thermodynamic Initial Guess Retrieval (TIGR) a été utilisée comme paramètres d'entrée pour établir une base de données de simulation atmosphérique. Comme seules les conditions de ciel clair ont été prises en compte pour la détermination des LST, les profils atmosphériques nuageux de la base de données TIGR ont été exclus. La carte de classification climatique de Köppen-Geiger a été appliquée pour analyser l'effet angulaire de la température de surface. Ce système divise le globe en cinq grands types de climat : tropical (A), aride (B), tempéré (C), froid (D) et polaire (E) (Beck et al., 2018). Le produit ESA CCI Soil Moisture (SM) Level 3 a été utilisé pour explorer les principaux facteurs moteurs de l'effet angulaire de la température de brillance de surface au cours de l'étude.

Le troisième chapitre présente la méthodologie utilisée pour cette étude. L'algorithme SW est appliqué aux températures de brillance TOA du satellite Sentinel-3A pour obtenir la température de brillance de surface. Les températures de surface peuvent être obtenues à l'aide de la méthode split-window en combinant deux canaux infrarouges adjacents pour réduire les effets atmosphériques. Ce chapitre se concentre sur quatre thèmes clés. La première section de ce chapitre couvre le processus de dérivation de l'équation de transfert radiatif pour l'algorithme SW de la température de brillance de surface. L'algorithme SW a été dérivé de la théorie du transfert radiatif, en

incorporant des hypothèses spécifiques (Coll et Caselles, 1997). La radiance mesurée reçue par les capteurs thermiques infrarouges provient principalement de la surface de la Terre et de l'atmosphère. Pour obtenir l'équation SW, il est également nécessaire de simplifier en linéarisant la fonction de Planck autour d'une température de référence. Pour ce faire, il faut supposer que la température atmosphérique équivalente, la température de brillance à l'altitude de la Terre et la température de brillance à la surface sont proches l'une de l'autre. De plus la température atmosphérique équivalente dans les canaux TIR 10,85 et 12,0  $\mu\text{m}$  peut être exprimée à l'aide d'une relation linéaire (Coll et al., 1994a ; Coll et al., 1994b ; Zheng et al., 2019). Dans des conditions sans nuages, en supposant un équilibre thermique local, l'équation générale de transfert radiatif peut être exprimée sous la forme de l'Eq (1), sans tenir compte de la radiance de diffusion solaire.

$$T_g = a_0 + a_1 T_i + a_2 (T_i - T_j) + a_3 (T_i - T_j)^2 \quad (1)$$

où  $a_0$ ,  $a_1$ ,  $a_2$  et  $a_3$  sont des constantes qui dépendent des conditions atmosphériques ;  $T_i$  et  $T_j$  sont les températures de brillance TOA dans les canaux TIR 10,85 et 12,0  $\mu\text{m}$  ;  $T_g$  est la température de brillance de la surface.

Le code de transfert radiatif atmosphérique MODerate resolution atmospheric TRANsmission (MODTRAN) a été utilisé pour simuler l'atmosphère et dériver les paramètres atmosphériques. Étant donné que l'extraction de la température de surface à partir de données infrarouges thermiques n'est applicable que dans des conditions de ciel clair, les profils atmosphériques dans des conditions de ciel clair de la base de données TIGR2000 ont été sélectionnés. Au total, 60 profils atmosphériques avec une teneur en vapeur d'eau atmosphérique comprise entre 0,06 g/cm<sup>2</sup> et 6,5 g/cm<sup>2</sup> ont été sélectionnés parmi les profils atmosphériques sans nuages, qui couvrent presque toutes les conditions atmosphériques à l'échelle mondiale. Ces 60 profils sont utilisés comme entrées dans MODTRAN pour simuler les paramètres atmosphériques.

La température de l'air ( $T_0$ ) dans la couche inférieure de chaque profil atmosphérique est comprise entre 230 et 320 K. Pour mieux simuler la corrélation entre  $T_0$  et  $T_g$ , l'entrée  $T_g$  a été modifiée en fonction de  $T_0$  pour chaque profil. Lorsque  $T_0$  dépasse 280 K,  $T_g$  varie de  $T_0 - 5$  K à  $T_0 + 10$  K, avec un intervalle de 5 K. Lorsque  $T_0$  est inférieur ou égal à 280 K,  $T_g$  varie de  $T_0 - 5$  K à  $T_0 + 5$  K, avec le même intervalle. Dans les simulations, l'émissivité moyenne a été fixée pour varier de 0,94 à 1,0, avec

un intervalle de 0,02. L'émissivité du sol pour les deux canaux infrarouges thermiques du SLSTR varie de 0,959 à 0,981. Parallèlement, la différence d'émissivité est comprise entre -0,02 et 0,02, avec un pas de 0,005. Par conséquent, l'ensemble des données de simulation comprend 8 316 cas différents.

Les paramètres atmosphériques pour deux canaux infrarouges thermiques issus de MODTRAN sont utilisés pour dériver la radiance de surface et la température de brillance de surface. Les coefficients de l'algorithme split-window pour les données SLSTR ont été déterminés par une analyse de régression des moindres carrés en combinaison avec les données simulées. Les coefficients de l'algorithme SW ont été obtenus à partir des canaux TIR nadir et oblique, respectivement.  $a_0$ ,  $a_1$ ,  $a_2$ , et  $a_3$  dans l'équation (1) et présentés dans la table 1.

Table 1 Les coefficients de l'algorithme SW.

Vue d'observation	$a_0$	$a_1$	$a_2$	$a_3$
Nadir	-5.58	1.02	0.37	0.41
Oblique	-5.49	1.02	0.11	0.57

Selon l'équation de l'algorithme SW dans l'Eq (1), l'incertitude totale de la température de brillance de surface est composée des contributions du modèle d'obtention de la température de brillance de surface ( $\delta(sim)$ ) et de la température de brillance TOA ( $\delta(bt)$ ). Les sources d'incertitude sont supposées être indépendantes (Hulley et al., 2012a ; Jiménez-Muñoz et Sobrino, 2006).

Pour calculer l'incertitude de la température de brillance de surface associée à l'incertitude du modèle, on suppose qu'il n'y a pas d'incertitudes dans les paramètres d'entrée, y compris le profil atmosphérique, la radiance TOA. Seule l'incertitude de l'algorithme lui-même est prise en compte. L'incertitude du modèle est caractérisée par la RMSE entre la température de brillance de surface obtenue par l'algorithme SW et la température de brillance de surface utilisée dans les simulations de transfert radiatif MODTRAN.  $\delta(sim)$  est de 0,74 K au nadir et de 1,23 K à l'oblique.  $\delta(bt)$  est de 1,44 K au nadir et de 1,14 K à l'oblique. L'incertitude totale  $\delta(T_g)$  des observations nadir et obliques est de 1,62 K et 1,68 K, respectivement.

Le quatrième chapitre définit tout d'abord la zone d'étude. Bien que l'algorithme d'obtention de la température de surface suppose que le rayonnement thermique de la surface est isotrope, les pixels hétérogènes et mixtes sont largement présents. Par conséquent, la sélection de pixels avec des types de couverture terrestre uniformes dans

la zone d'étude pourrait réduire les erreurs. Cette étude utilise les données de classification de l'occupation du sol MCD12Q1 pour analyser l'homogénéité spatiale des types d'occupation du sol en 2018. Pour couvrir la diversité des types écologiques et climatiques mondiaux, un total de 42 sites ont été répartis dans le monde entier, allant des régions froides de l'hémisphère nord à l'Antarctique (forêts sempervirentes à feuilles aiguilles (ENF), forêts sempervirentes à feuilles larges (EBF), forêts à feuilles larges caduques (DBF), forêts mixtes (MF), arbustes ouverts (OSH), savanes boisées (WSA), savanes (SVA), prairies (GRA), zones humides permanentes (WET), terres cultivées (CRO), terres urbaines et bâties (URB), mosaïque terres cultivées/végétation naturelle (CVM), neige et glace (SNO), terres stériles ou à végétation clairsemée (BSV)).

Sur la base des zones d'étude sélectionnées, il est nécessaire d'éliminer les valeurs aberrantes en appliquant la moyenne plus ou moins trois fois l'écart-type. Si le nombre de pixels traités dans une zone d'étude sélectionnée est inférieur à 1 %, la scène entière sera exclue de la suite de l'analyse. Les données restantes se composent de 1 910 et 2 996 scènes de jour et de nuit, respectivement.

Ensuite, l'amplitude et les caractéristiques de  $\Delta T_g$  à travers les différents types de couverture terrestre sont observées. Le SBT à  $0^\circ$  et  $55^\circ$  a été comparé sur 42 sites à travers 14 types de couverture terrestre différents (ENF, EBF, DBF, MF, OSH, WSA, SVA, GRA, WET, CRO, URB, CVM, SNO, BSV) de septembre 2019 à août 2020 mensuellement. Les résultats montrent que, indépendamment du jour ou de la nuit et dans les hémisphères nord et sud, les différences de température de brillance de surface vont de -3 K à 9 K. Les effets angulaires sur la température de brillance de surface sont généralement présents sur les surfaces terrestres. Pendant la journée, SNO présente le plus petit  $\Delta T_g$  moyen, principalement autour de 0 K, tandis que URB et BSV montrent les plus grandes différences, allant de 0 K à 6 K. Les variations saisonnières du  $\Delta T_g$  pendant la journée sont prononcées, avec la plus grande différence observée en été (jusqu'à 6 K) et la plus petite en hiver, allant de 0 K à 4 K. La nuit, les  $\Delta T_g$  de la plupart des sites sont plus faibles et ne varient pas avec les saisons, ce qui indique que l'effet angulaire sur le SBT est moins important la nuit. Pour le même type de couverture terrestre à des latitudes similaires, il y a peu de différence dans les  $\Delta T_g$  à différentes longitudes.

L'analyse explore l'influence de la saison. Dans l'ensemble, le  $\Delta T_g$  pendant la journée au printemps et en été est plus élevé qu'en automne et en hiver dans l'hémisphère nord. Le  $\Delta T_g$  nocturne est plus faible que le  $\Delta T_g$  diurne. Par ailleurs, la différence saisonnière de  $\Delta T_g$  pendant la nuit n'est pas aussi importante que pendant la journée. Cela s'explique par le fait que l'angle zénithal du soleil est plus faible en été qu'en hiver dans l'hémisphère nord, et que  $\Delta T_g$  est négativement lié à l'angle zénithal du soleil. Les schémas de variation saisonnière des quatorze types de couverture terrestre présentent une tendance cohérente. L'EBF a le  $\Delta T_g$  le plus élevé pendant les quatre saisons de l'année. MF et SNO ont les  $\Delta T_g$  annuels les plus faibles au cours de la période étudiée. L'intégrité des données n'est pas aussi bonne que dans l'hémisphère nord. Sur la base des données existantes, il apparaît que la variation saisonnière de  $\Delta T_g$  pendant la journée dans l'hémisphère sud n'est pas significative. En comparaison avec  $\Delta T_g$  pendant la journée, la fluctuation saisonnière de  $\Delta T_g$  pendant la nuit dans l'hémisphère sud est légèrement apparente. La différence été-hiver de  $\Delta T_g$  pendant la nuit peut atteindre 3 K ou 4 K pour la plupart des types de couverture terrestre.

Pour analyser la distribution de  $\Delta T_g$  en fonction du changement de latitude, les données globales sont séparées en six zones de latitude différentes de 0, 30 et 60 degrés, qui sont des zones de basse, moyenne et haute latitude dans l'hémisphère nord et l'hémisphère sud, respectivement. Le  $\Delta T_g$  moyen se situe entre -0,5 K et 4 K, la valeur minimale apparaissant dans les zones de haute latitude de l'hémisphère sud. Dans les zones de basse latitude des hémisphères nord et sud,  $\Delta T_g$  est élevé, avec une valeur d'environ 3,5 K. Dans la zone de latitude moyenne de l'hémisphère nord,  $\Delta T_g$  est d'environ 2 K, un peu plus bas que dans la zone de latitude moyenne de l'hémisphère sud, avec une valeur d'environ 2,8 K.  $\Delta T_g$  est d'environ 1 K dans la zone de haute latitude de l'hémisphère nord, tandis que  $\Delta T_g$  est inférieur à 0 K dans la zone de haute latitude de l'hémisphère sud. Dans la zone de haute latitude de l'hémisphère nord, l'écart-type de  $\Delta T_g$  est manifestement plus faible que dans les cinq autres zones.

La relation entre l'angle zénithal solaire dans chaque intervalle de  $10^\circ$  et  $\Delta T_g$  est examinée. La valeur du  $\Delta T_g$  moyen reste positive dans tous les cas. En général, la valeur moyenne de  $\Delta T_g$  montre une tendance à la baisse avec l'augmentation de l'angle zénithal solaire, allant d'environ 6 K à 0 K. En particulier, dans les cas où l'angle zénithal solaire se situe entre  $20^\circ$  et  $70^\circ$ ,  $\Delta T_g$  présente une tendance directe à la baisse. Dans les cas où l'angle zénithal est supérieur à  $70^\circ$ ,  $\Delta T_g$  reste stable, ce qui indique que l'effet angulaire

de la température de brillance est négligeable lorsque l'angle zénithal est élevé. L'écart-type de  $\Delta T_g$  est d'environ 1,5 K dans la plupart des cas, sauf lorsque l'angle zénithal est de  $20^\circ$ . En comparant les  $\Delta T_g$  dans les zones de basses, moyennes et hautes latitudes, il apparaît que les  $\Delta T_g$  dans les zones de hautes latitudes sont plus faibles que dans les zones de moyennes et basses latitudes.

La relation entre le climat pour 5 types de climat et  $\Delta T_g$  est examinée. La différence de la moyenne  $\Delta T_g$  pendant le jour et la nuit est plus élevée dans la zone climatique aride que dans la zone tropicale. Dans la zone tempérée, ENF, DBF, CRO et CVM présentent des fluctuations saisonnières similaires à celles de la zone aride. Pour EBF et URB, le  $\Delta T_g$  moyen au printemps est un peu plus élevé qu'en été. Cela pourrait s'expliquer par le fait que la végétation dans les zones EBF et URB est relativement stable par rapport aux autres types de couverture terrestre. De plus, la variation saisonnière est perceptible dans la zone froide pendant la journée. Il n'y a qu'un seul type de couverture terrestre distribué dans la zone de climat polaire, et c'est le SNO. Le  $\Delta T_g$  est presque négligeable dans cette zone climatique. Le maximum de  $\Delta T_g$  est inférieur à 1 K. La fluctuation saisonnière est également inapparente. Par rapport à la moyenne globale de  $\Delta T_g$  pendant la journée, la moyenne de  $\Delta T_g$  pendant la nuit est nettement plus faible, tous les points de données étant répartis entre 0 K et 2 K.

Afin d'explorer les principaux facteurs de la variabilité spatiale de  $\Delta T_g$  au cours de la période étudiée, GeoDetector a été utilisé pour analyser  $\Delta T_g$  et ses facteurs potentiels. GeoDetector est une méthode statistique utilisée pour détecter l'hétérogénéité spatiale des variables et révéler leurs facteurs d'entraînement (WANG et al., 2010). L'avantage de cette méthode est qu'elle permet de détecter les facteurs de différenciation spatiale de la variable dépendante, ainsi que l'impact des interactions entre les facteurs (WANG et HU, 2012). GeoDetector se compose de quatre modules : détecteur de facteurs, détecteur d'interactions, détecteur de risques et détecteur écologique, parmi lesquels le détecteur de facteurs, le détecteur de risques et le détecteur écologique sont utilisés pour explorer les facteurs moteurs de la variabilité spatiale de  $\Delta T_g$  dans cette étude.

Dans cette étude, le détecteur de facteurs est utilisé pour explorer le facteur déterminant de la différenciation spatiale de  $\Delta T_g$  et la contribution des facteurs déterminants sur  $\Delta T_g$ . SZA est le déterminant dominant avec une contribution écrasante à  $\Delta T_g$  pendant la journée dans l'hémisphère nord et l'hémisphère sud. La saison est le deuxième déterminant le plus important avec une valeur q d'environ 0,35. Le NDVI et

le DEM sont les déterminants les plus faibles en termes de contribution à  $\Delta T_g$  pendant la journée. Cela peut s'expliquer par le fait que la zone d'étude a été choisie à une altitude relativement uniforme. Pendant la nuit, il n'y a pas de déterminant unique qui l'emporte sur les autres dans la contribution au  $\Delta T_g$ . Les quatre déterminants (LULC, climat, saison et latitude) ont une valeur q similaire. Le SM est le déterminant le plus faible pendant la nuit, tant dans l'hémisphère nord que dans l'hémisphère sud. En comparant les résultats de l'hémisphère nord et de l'hémisphère sud, la contribution des déterminants est plus élevée dans l'hémisphère sud que dans l'hémisphère nord, ce qui indique que dans l'hémisphère sud,  $\Delta T_g$  est plus facilement influencé par des facteurs extrinsèques.

Le détecteur d'interaction est utilisé pour analyser si l'interaction entre les déterminants de la différenciation spatiale de la température de brillance de surface renforcera ou affaiblira leur effet sur  $\Delta T_g$ . L'interaction des déterminants montre que la contribution de deux déterminants combinés est plus élevée que celle d'un seul déterminant. Il existe deux types d'interaction entre deux déterminants dans cette étude, l'amélioration bifactorielle et l'amélioration non linéaire. Pendant la journée, dans l'hémisphère nord comme dans l'hémisphère sud, c'est la SZA qui contribue le plus au  $\Delta T_g$  en tant que déterminant unique. Les combinaisons de la SZA avec d'autres déterminants montrent également une contribution importante, la plupart des combinaisons montrant un schéma d'amélioration bifactorielle, à l'exception de la combinaison avec la latitude. Les saisons sont le deuxième niveau qui présente une plus grande promotion dans les contributions au  $\Delta T_g$  lorsqu'elles sont combinées avec d'autres déterminants. Le modèle d'amélioration non linéaire est plus courant dans l'hémisphère nord que dans l'hémisphère sud. Pendant la nuit, dans l'hémisphère nord, aucun déterminant ne contribue de manière dominante à  $\Delta T_g$  et la moyenne des valeurs q est la plus faible dans les quatre catégories. Bien que le climat, la latitude et l'LULC soient les déterminants ayant les valeurs de q les plus élevées, leurs combinaisons entre elles ne montrent pas d'améliorations significatives des valeurs de q. La combinaison la plus forte est celle entre LULC et SM, avec une valeur q de 0,53, suivie par la combinaison entre le climat et la saison, avec une valeur q de 0,52. Pendant la nuit, si l'on considère les valeurs globales de q dans l'hémisphère nord et dans l'hémisphère sud, la combinaison entre la saison et l'LULC ou le climat est la plus forte de toutes les combinaisons. En termes de contribution globale, la combinaison entre la saison et

l'LULC présente la meilleure performance parmi toutes les combinaisons dans toutes les catégories.

Le détecteur de risque peut calculer la valeur moyenne de la variable dépendante pour chaque catégorie en fonction de différents déterminants, et déterminer s'il existe une différence significative entre deux catégories. La distribution des  $\Delta T_g$  du SNO est significativement différente de celle des autres types d'UTC. Les  $\Delta T_g$  varient de manière significative dans l'intervalle SM [0,4, 0,5]. L'écart entre les  $\Delta T_g$  au printemps et à l'automne est très important. De même, le climat et la latitude ont également un impact significatif sur  $\Delta T_g$  montrent un gradient descendant. La corrélation entre  $T_g$  et SZA est négative. Les  $\Delta T_g$  dans les différentes plages de NDVI présentent des tendances opposées à celles de la SZA. Dans les plages de NDVI adjacentes, la corrélation entre les  $\Delta T_g$  est bonne. La valeur globale de  $\Delta T_g$  pendant la nuit est plus faible que pendant la journée, de sorte que le gradient de  $\Delta T_g$  dans les différentes plages de déterminants est relativement faible.

La cinquième section résume les résultats précédents et les remarques finales, et propose les perspectives suivantes. Dans cette recherche de thèse, nous avons utilisé un algorithme de fenêtre divisée pour récupérer la température de luminosité de la surface terrestre à partir de deux angles de vue : le nadir et la vue oblique. La différence de température de surface entre les différents angles de vue a été analysée en fonction des saisons, des types de couverture terrestre et des positions géographiques. Les facteurs d'influence de l'effet angulaire et leurs corrélations ont également été examinés.

Toutefois, il reste plusieurs travaux à réaliser dans le cadre de recherches futures. En ce qui concerne les algorithmes, un algorithme classique de split-window a été utilisé dans cette étude pour obtenir la température de brillance de surface. Les coefficients de l'algorithme de fenêtre fractionnée sont uniformes dans toute la gamme de vapeur d'eau. Un algorithme de split-window plus avancé avec des coefficients segmentés pour différentes valeurs de vapeur d'eau pourrait être utile pour une récupération plus précise de la température de brillance de surface. Les algorithmes basés sur le TIR ont souvent une erreur et un biais élevés sur les surfaces stériles/à faible végétation en raison des paramètres physiques et radiatifs particuliers. L'écart négatif peut parfois atteindre plusieurs degrés pendant la journée. Pour améliorer la précision de l'estimation de la température de surface dans ces conditions, un ensemble particulier de coefficients peut s'avérer utile.

La validation de la température de brillance de surface sous deux angles est difficile. Normalement, la LST peut être évaluée à l'aide de mesures in situ collectées par des radiomètres IRT. Mais ces radiomètres sont souvent positionnés pour une vue au nadir. Il est difficile d'obtenir des mesures in situ à partir d'une vue oblique. C'est pourquoi il est urgent de mettre en place des sites in situ avec des observations à double angle. La validation R-biased est une autre méthode couramment utilisée pour évaluer la précision de la LST. Il est probable qu'elle soit applicable à la validation des observations à double angle à l'avenir. Le modèle DART (Discrete Anisotropic Radiative Transfer) est un modèle de transfert radiatif tridimensionnel complexe qui peut construire une surface naturelle à partir de données géo morphiques, simulant le processus de transfert radiatif entre la surface et l'atmosphère dans les bandes TIR. Il joue un rôle important dans l'analyse des effets des pixels mixtes et des ondulations du terrain sur le rayonnement. Il est également applicable à la simulation du rayonnement à partir d'une vue nadir et oblique. La comparaison entre la température de brillance de la surface simulée et observée peut également aider à améliorer la compréhension des effets angulaires sur différents terrains. Cela permettrait d'obtenir des estimations plus précises de l'effet angulaire et fournirait une base pour la normalisation angulaire et la détermination de la température des composants.

# 1.Introduction

## 1.1 Background

Land surface temperature (LST) is a key variable in meteorology and geosciences (Dash et al., 2010; Li et al., 2023). It is frequently prescribed for assessing land surface-atmosphere exchange processes, constraining surface energy budgets, estimating evapotranspiration, and monitoring climate change at both global and regional scales (Anderson et al., 2012; Bright et al., 2017; Friedl, 2002; García-Santos et al., 2019; He et al., 2020; Kalma et al., 2008; Keenan and Riley, 2018; Li et al., 2022; Li et al., 2023; Tang et al., 2022; Li et al., 2013). As part of the European Space Agency's (ESA) Climate Change Initiative (CCI) project, LST is one of the indicators of the Essential Climate Variables (ECV) (Malakar et al., 2018). It is also valuable for studying urban heat islands, managing agricultural production, and forecasting and monitoring natural hazards (Chen et al., 2022; Hu et al., 2020; Hu et al., 2019; Liu et al., 2022; Masoudi and Tan, 2019; Peng et al., 2018; Zhou et al., 2018).

The study of using satellite data to retrieve surface temperature began in the early 1960s. Satellite remote sensing is the only possible means to obtain accurate LST with the high spatial and temporal resolution at regional and global scales (Li et al., 2013). Over the following decades, the number of thermal infrared (TIR) sensors capable of detecting surface temperature has been carried on different satellites with a fine performance, e.g., The Advanced Very High Resolution Radiometer (AVHRR)/Visible Infrared Imaging Radiometer Suite (VIIRS) on board the National Oceanic and Atmospheric Administration (NOAA) polar-orbiting satellite series, the Thematic Mapper (TM)/Enhanced Thematic Mapper Plus (ETM+)/Thermal InfraRed Sensor (TIRS) on board Landsat satellite series, Along Track Scanning Radiometer (ATSR) on board European Remote-Sensing Satellite (ERS), the Moderate-resolution Imaging Spectroradiometer (MODIS) on board Terra and Aqua satellites, the Advanced Along-Track Scanning Radiometer (AATSR) on board the Envisat satellite, the Spinning Enhanced Visible and InfraRed Imager (SEVIRI) on board Meteosat Second Generation (MSG) satellite series, Sea and Land Surface Temperature Radiometer

(SLSTR) on board Sentinel-3, the Advanced Himawari Imager (AHI) on board Himawari satellites, Visual and Infrared Multispectral Sensor (VIMS) on board Gao-Fen 5 (GF 5) satellite, ECOsystem Spaceborne Thermal Radiometer Experiment on Space Station (ECOSTRESS) on board the International Space Station (ISS) , and Visible and InfraRed Radiometer (VIRR)/ Advanced Geostationary Radiation Imager (AGRI) on board Chinese Fengyun (FY) satellite series. SLSTR is the upgraded dual view scanning radiometer of (A)ATSR. The acquisition of TIR data with two observation angles brings new sources and opportunities for LST retrieval and angular effect studies.

Although lots of polar-orbiting satellite LST products obtained by the above sensors are already available to users, the variation in observation angles during satellite scanning introduces directional differences in surface thermal radiation. Most researches on the directionality of thermal radiation are based on experiments conducted from ground or airborne platforms. By adjusting observation angles, these studies acquire brightness temperature data and analyze variations in surface brightness temperature. Typically, the directionality of homogeneous surfaces is attributed to emissivity. However, the main limitation of such studies is that data can only be acquired for short durations and over small areas. Since surface brightness temperature continuously changes with atmospheric conditions and illumination, satellite data acquired from different observation times cannot be directly used to analyze angular effects on surface brightness temperature. As a result, there are fewer direct observations from satellite platforms. Sentinel-3A/SLSTR, however, can provide large-scale, long-term, multi-angle real-time observations, making it particularly suitable for studying angular effects on surface brightness temperature. Research on angular effects is expected to further enhance the accuracy of surface temperature retrieval.

### 1.1.1 The algorithms of LST retrieval from satellite TIR data

Since the 1970s, researchers have proposed various hypotheses and methods to explore methods for TIR LST retrieval. The most widely used LST retrieval algorithms at present includes single-channel (SC) algorithm, split-window (SW) algorithm, dual-angle (DA) algorithm, temperature and emissivity separation (TES) algorithm, and day/night (D/N) algorithm.

## SC Algorithm

The SC algorithm takes the radiation of a single thermal infrared band within the atmospheric window obtained by satellite sensors as the data source. Under the condition of known surface emissivity, it obtains atmospheric parameters, such as atmospheric upward and downward radiation and atmospheric transmittance, through atmospheric temperature and humidity profiles and atmospheric transmission models, by performing atmospheric correction on the thermal infrared image, and finally uses the radiative transfer equation to obtain LST. Atmospheric profile can be acquired from sounding data, atmospheric vertical detection instruments, and meteorological reanalysis data. For situations where there is spatial and temporal inconsistency between satellite data and atmospheric profiles, spatio-temporal interpolation methods can be used to obtain atmospheric parameters for satellite image pixels.

In order to reduce the errors caused by atmospheric profiles, Qin et al. (2010) simplified SC algorithm based on a series of assumptions, making it possible to obtain LST using Landsat/TM data with only 3 parameters: land surface emissivity, atmospheric transmittance and average atmospheric temperature. Following researchers brought up a simple and universal SC algorithm, referred to as JM&S algorithm, which can obtain LST by taking atmospheric water vapor content as the only input parameter (Jimenez-Munoz and Sobrino, 2003). In the researches published in 2009, Jimenez-Munoz et al used 4 atmospheric profile database and redefined the coefficients of algorithm for Landsat remote sensing data (Jimenez-Munoz et al., 2009). The Advanced Spaceborne Thermal Emission Reflection Radiometer (ASTER) Global Emissivity Dataset (GED) were used in SC algorithm to calculate land surface emissivity and improved the accuracy of LST retrieval over barren or sparsely vegetated areas for Landsat 8 data (Duan et al., 2019; Malakar et al., 2018). Considering the 3-D geometry structure and adjacency effects, a radiative transfer equation (RTE)-based single-channel algorithm was developed to retrieve LST from the Landsat 8 TIR data in mountainous and urban areas (Ru et al., 2022; Zhu et al., 2021).

SC algorithm is mainly used for satellites with only one thermal inferred channel, e.g., Landsat satellite series, HJ-1 satellite. The disadvantage of SC algorithm is that the error is relatively high in conditions where atmospheric water vapor content is at a high level.

## SW Algorithm

SW algorithm combines the brightness temperature of two adjacent thermal infrared bands (usually 11  $\mu\text{m}$  and 12  $\mu\text{m}$ ) to eliminate the influence of the atmosphere on the basis of different characteristics of atmospheric absorption (mainly due to differences in atmospheric water vapor) in the atmospheric window at 10-13  $\mu\text{m}$  band. Initially, this method was used for the retrieval of sea surface temperature (SST), with an accuracy of better than 1 K.

Price (1984) improved the split-window algorithm by introducing the surface emissivity parameter and applied this method to the retrieval of LST. Becker and Li (1990) proposed a local split-window algorithm for AVHRR data at channel 4 and 5 with the emissivity of two TIR channels were known. Coll et al. (1994) first proposed a quadratic term split-window algorithm, considering the influence of the atmosphere on the coefficients is nonlinear. Similarly, Sobrino et al. (1994) considered the influence of land surface emissivity and the ratio of atmospheric transmittance at two channels. Given the known surface emissivity, the retrieval accuracy of AVHRR LST is 0.4 K. Based on the local split-window algorithm, Wan and Dozier (1996) proposed a universal split-window algorithm, which is insensitive to the uncertainty of emissivity and sensor errors. Qin et al. (2001) simplified the split-window algorithm to estimate LST by only two parameters, atmospheric transmittance and surface emissivity. Chen et al. (2017) improved the quadratic term split-window algorithm for Gaofen-5 satellite, reducing the retrieval error of LST under cases with low-emissivity surface but increasing the retrieval error of LST under a high humid atmosphere. A split-window algorithm, in which surface emissivity is estimate using ASTER GED products, was proposed for different sensors, such as VIIRS, SLSTR, VIRR (Wang et al., 2019; Zhang et al., 2019; Li, et al., 2023). Zheng et al. (2019) proposed an algorithm based on SLSTR data, which uses the split-window algorithm to estimate daytime LST and incorporates mid infrared channel data to estimate nighttime LST. This method improves the inversion accuracy of SLSTR LST at nighttime. A typical nonlinear split window algorithm used in this study is shown below:

$$T_s = a_0 + a_1T_i + a_2(T_i - T_j) + a_3(T_i - T_j)^2 \quad (1.1)$$

where  $T_s$  is LST;  $a_k$  ( $k=0,1,2,3$ ) are constants depend on the spectral response function  $g_i$  and  $g_j$ , the emissivity  $\varepsilon_i$  and  $\varepsilon_j$ , the atmospheric water vapor content WVC and

the viewing zenith angle VZA, so  $a_k$  can be expressed as Eq (1.2).  $T_i$  and  $T_j$  are the brightness temperatures at the top of the atmosphere for TIR channels.

$$a_k = f_k(g_i, g_j, \varepsilon_i, \varepsilon_j, WVC, VZA) \quad (1.2)$$

Due to the simple forms and high accuracy, split-window algorithms are the most commonly used LST retrieval methods and applied to multiple sensors including AVHRR, MODIS, VIIRS, AATSR, SLSTR, VIRR, and AGRI.

### **DA Algorithm**

The principle of multi-angle algorithm is similar to that of SW algorithm. Utilizing the difference in atmospheric absorption caused by different atmospheric paths observed from different angles of the same object, it eliminates atmospheric influence by combining the brightness temperature obtained from different angles in a linear or nonlinear form (Chedin et al., 1982). DA algorithm is initially used for SST retrieval. Prata (1993) developed a DA algorithm for LST retrieval based on ATSR data. The development of multi-angle algorithms is mainly based on the development of dual-angle sensors, e.g., ATSR-1 onboard ERS-1, ATSR-2 onboard ERS-2, AATSR onboard ENVISAT, and SLSTR onboard Sentinel-3A. These sensors can provide observation from two angles: nadir observation with zenith angle at 0-21.6 degrees, and oblique observation with zenith angle at 52-55 degrees. Sobrino et al proposed a nonlinear multi-angle algorithm to reduce the influence of atmospheric water vapor content, and validated the accuracy in subsequent studies (Sobrino et al, 2004, Sobrino et al, 2005). Li et al. (2023) compared the accuracy of multi-channel algorithms and DA algorithm for LST retrieval based on SLSTR data. The accuracy of LST retrieval using the DA algorithm shows the highest uncertainty influenced by variations in surface emissivity and brightness temperature.

The brightness temperature at different observation angles is easily affected by factors such as emissivity and terrain, resulting in angular effects. This makes DA algorithms only applicable over homogeneous surfaces such as lake or sea, and difficult to apply to actual LST retrieval processes.

### **TES Algorithm**

Temperature and emissivity separation (TES) algorithm was initially proposed for ASTER and later applied to LST retrieval in MxD21, VIIRS VPN21 and ECO2LSTE LST products (Gillespie et al., 1998; Hulley and Hook, 2011; Hulley et al., 2012a; Islam

et al., 2017). TES algorithm consists of 3 models: normalization emissivity method (NEM), spectral ratio (SR) and maximum-minimum apparent emissivity difference method (MMD). NEM is used to estimate LST and emissivity. SR is used to calculate the ratio of emissivity and average emissivity of all bands, during which the spectral features of emissivity at each band remains. Finally, MMD is used to determine the optimal surface emissivity and to obtain LST.

The advantage of TES algorithm is that the LST and surface emissivity can be retrieved simultaneously and it is applicable for most surface types. Atmospheric correction must be applied in advance (Jiménez-Muñoz et al., 2014). The disadvantage is that the accuracy is relatively low in conditions that atmospheric water vapor content is high or difference in emissivity spectra is inconspicuous (Malakar and Hulley, 2016; Sabol et al., 2009). Zheng et al. (2019) proposed the SW-TES algorithm, combining the advantages of both SW and TES algorithms to retrieve LST. In this method, SW algorithm is utilized for atmospheric correction, while TES algorithm is utilized for simultaneously retrieval LST and surface emissivity. This combined algorithm presents higher accuracy compared to traditional algorithms. Building on this, Ru et al. (2023) considered the 3-D structure of urban environments to enhance the accuracy of urban land surface temperature retrieval.

### **Physics-Based D/N Algorithm**

Wan and Li (1997) proposed the physics-based D/N algorithm to estimate LST and emissivity simultaneously using MODIS daytime and nighttime observations at 3 Mid-Infrared (MIR) bands (band 20, 22, and 23) and 4 TIR bands (band 29, 31, 32, and 33). The physics-based D/N algorithm was inspired by the D/N temperature independent spectral index (TISI) method (Becker and Li, 1990b). It requires accurate atmospheric profile in advance. This algorithm uses multi-temporal information and assumes that there is no significant change in the surface emissivity during the adjacent day and night observations to solve the underdetermined problem. The main assumptions of day/night algorithm include:

- (1) Land surface is Lambert reflector and its emissivity is constant in daytime and nighttime;
- (2) Atmospheric temperature at bottom layer and atmospheric water vapor content acquired from MODIS atmospheric profile is sufficient to describe atmospheric condition;

(3) The bi-directional reflection factor is similar at 3 MIR bands.

There are 14 nonlinear functions in this algorithm, which are built based on day/night observations from 7 MODIS bands. The unknowns in the functions are: land surface emissivity of 7 bands, LST at daytime and nighttime, atmospheric temperature at bottom layer and atmospheric water vapor content at daytime and nighttime, and bidirectional reflection factor. Using statistical regression and least square fitting, LST and surface emissivity can be obtained simultaneously. The physics-based D/N algorithm is applied in the production of MxD11B1 LST product.

The split-window algorithm was used to estimate LST in this study, due to its simplicity, high efficiency and effectiveness in atmospheric correction. Another reason is that split-window algorithm is sensitive to the variety of viewing zenith angle, making it a feasible method to evaluate the influence of angle effects on land surface brightness temperature.

### 1.1.2 The angular effect of brightness temperature

Based on previous LST retrieval algorithm, a typical hypothesis is that the land surface exhibits isotropic thermal emission. Due to the widespread presence of heterogeneous and non-isothermal mixed pixels on the Earth's surface, surface thermal radiation exhibits significant directional characteristics. The directional characteristics of surface thermal radiation were first discovered by Fuchs et al. (1967) in a field experiment, where surface temperatures of row crops observed at different angles varied by 1-3 K, indicating a clear angular effect. Since then, over the past few decades, scientists have used TIR sensors onboard various observation platforms to study the thermal radiation directionality across different surface types and structures. These studies have further confirmed the angular effect on surface brightness temperature. Based on the observation platforms, surface brightness temperature can be obtained from ground-based, airborne and spaceborne observations.

#### **Ground-based observations**

Kimes (1980) observed soybean fields and found that the brightness temperature difference between the top and bottom of the canopy reached up to 11 K. Further studies on row crops such as cotton, wheat, and sunflowers showed that the largest brightness temperature difference, up to 16 K, occurred perpendicular to the row direction (Kimes, 1981; Kimes and Kirchner, 1983; Paw et al., 1989). Lagouarde et al. (1995) conducted

simultaneous observations at two angles above corn, alfalfa, grass, and bare soils with different roughnesses from a height of 2 m. The directional differences of brightness temperature range from -4 K to 3.5 K, largely depending on the type of surface. Chehbouni et al. (2001) observed vegetation canopies and found that the brightness temperature difference between vertical and inclined observations could be as high as 5 K, with large discrepancies in soil and vegetation temperatures observed at different times. To meet a requirement of quick acquiring multi-angle data, the Multi-Angle Observation System (MAOS) was designed with the ability to automatically collect multi-angle bi-directional reflectance factor (BRF) and directional thermal radiance of land surface in the same footprint synchronously (Yan et al., 2012). Limited by the observation height of no more than 5 m, the footprint is usually smaller than 2.5 m × 2.5 m. Adderley et al. (2015) used panoramic time-sequential thermography data recorded by a thermovision A40M thermal infrared camera at a height of 17.95 m. This dataset captured the temperature of representative urban surface within a 360° swath over 24 hours. The effective anisotropy is pronounced during the daytime, reaching up to 3.5 K, while at night it exhibits minimal anisotropy, with values below 1 K. Cao et al. (2018) expanded the footprint by installing sensors on a 30-meter-high tower. Multi-angle observations of row-planted corn canopies revealed an inconspicuous hotspot effect obstructed by the sensor, where brightness temperature varying with the zenith angle. Morrison et al. (2023) combined ground-based multi-angle observations and detailed 3D surface modeling to assess the impact of modelled LST anisotropy. During daytime, a change in view angle of 47° resulted in an LST difference of up to 5.1 K for the realistic building model, also found in idealized model.

Ground-based observations can provide multi-angle experimental designs but are limited by the inability to cover large areas. And it is difficult to observe study areas with complex surface structures. In order to avoid the influence of changing solar and weather conditions during the observation period, multi-angle measurements of ground objects should be completed as quickly as possible.

### **Airborne observations**

Compared with ground-based observations, airborne observations can obtain data from a wider range of areas. Lagouarde et al. (2000) conducted multi-angle airborne observations in France and found that forests behaved like isothermal pixels, with the maximum brightness temperature difference between oblique and nadir observations

reaching 4 K within an observation angle range of  $0^\circ$  to  $60^\circ$ . In a study of vineyards with row structures, a close correlation between brightness temperature anisotropy and row structure was found (Lagouarde et al., 2014). Liu et al. (2012) conducted multi-angle observations of cornfields (including intercropped wheat) using airborne Wide-angle Infrared Dual-model line/area Array Scanner (WIDAS) and found that the brightness temperature difference between bare soil and vegetation could be as high as 20 K. In urban areas, the directional nature of thermal radiation can constrain the accuracy of urban surface temperature inversion, and in recent years, research on urban thermal radiation directionality has been gradually emerging (Voogt and Oke, 2003). In cities, the temperature difference between different observation angles can reach 9-10 K, with the lower differences in thermal radiation directionality occurring during nighttime (Lagouarde et al., 2008; Lagouarde et al., 2010; Voogt et al., 2008). In recent years, the rapid development of technology has made unmanned aerial vehicles (UAVs) as a new platform for close-range (tens to hundreds of meters) multi-angle measurements. Bian et al. (2021) used UAV data with the maximum viewing zenith angle of  $57.5^\circ$  and  $17.5^\circ$  in the flight and cross-flight directions, combined with 3D modified model, to simulate the brightness temperatures directional anisotropy and thereby deliver fine-scale brightness temperatures. Jiang et al. (2022) analyzed variations in directional brightness temperature by using UAV-based multi-angle observations. In urban surface, the variations in directional brightness temperature range from -3 to 12 K, mainly depending on viewing zenith angle and viewing azimuth angle.

Airborne platforms enable large-scale, multi-angle observations, but traditional airborne platforms require prior airspace approval. Moreover, weather conditions during the approved flight window may not be suitable, and the associated costs are high. UAVs are more cost-effective and offer greater flexibility in flight duration, though long-term observations remain challenging.

### **Spaceborne observations**

Spaceborne observations of surface brightness temperatures are mainly achieved using sensors with large zenith angles or dual-angle sensors. Rasmussen et al. (2011) used data from the Meteosat Second Generation (MSG) geostationary satellite to analyze temperature differences caused by different observation angles, showing that

these differences vary with time and season, with a maximum difference of 3 K. Ren et al. (2011) used the MOD11B1 product from MODIS to analyze the relationship between emissivity and observation angle for grassland, crops, and bare soil. By incorporating directional emissivity into land surface temperature retrieval, they found that the temperature difference from the original temperature product ranged between -1 K and 3 K. Hu et al. (2016) analyzed MODIS surface temperature products for Chicago and New York, identifying strong angular effects on surface temperatures during the daytime and weaker effects at nighttime. Shi et al. (2023) collected eleven years of MODIS land surface temperature products for Hefei, covering the months from May to September. The study revealed significant diurnal variations in urban thermal radiation directionality, with values reaching up to 4.6 K during the daytime in highly urbanized areas, and 2.6 K at night. Wang et al. (2021) utilized both airborne and satellite observation data in Toulouse. The anisotropy of satellite scales exhibited seasonality, with solar elevation determining the different anisotropy distribution patterns in summer and winter. During summer daytime, the MODIS LST differences across all viewing angles reached up to 6.6 K and 4.9 K for Terra/Aqua, respectively. Similar levels of anisotropy were observed in winter, with values of 6.1 K and 4.0 K for Terra/ Aqua, respectively. Compared to airborne measurements, model simulations underestimated the magnitude of anisotropy.

Currently, only the ATSR series sensors (ATSR-1, ATSR-2, AATSR, SLSTR) provide real-time observations at different angles ( $0^\circ$  and  $55^\circ$ ). Li et al. (2001) analyzed an ATSR-2 image and found that the angular variation of ground brightness temperature is highly sensitive to atmospheric uncertainties, with the SW method demonstrating greater accuracy compared to the SC method. Coll et al. (2019) used AATSR data to study the brightness temperature differences between nadir and forward observations, finding that over land, the maximum difference occurs in summer, reaching about 8 K, while sea surface brightness temperature differences were smaller and less variable over time and season.

Cao et al. (2019) systematically reviewed and summarized the observation and modeling of thermal radiation directionality, confirming through ground-based, airborne, and spaceborne observations that surface radiation directionality significantly impacts surface temperature accuracy. Compared to ground-based, airborne observations, satellite platforms enable large-scale, long-term observations globally.

Sentinel-3A/SLSTR can acquire multi-angle, near real-time observation data, making it suitable for studying the angular effects of surface brightness temperature. By investigating angular effects, the accuracy of land surface temperature retrieval is expected to improve further.

## 1.2 Objective and structure of this thesis

This research adopts SLSTR TIR data as the main data source and retrieves surface brightness temperature using SW algorithm, and analyzes the angular effect of surface brightness temperature. The main content is shown as follows:

- (1) Generate a simulated database and determine the SW algorithm for retrieving surface brightness temperature.
- (2) Compare the differences of surface brightness temperatures between nadir and oblique views obtained from sentinel-3A SLSTR data.
- (3) Analyze the possible factors to explain angular effects of surface brightness temperatures between nadir and oblique observations.

According to the research objectives, this thesis is organized into five chapters.

This thesis first gives a brief overview of the recent history of LST retrieval and observation of angular effects. The second chapter describes data used in this study. The third chapter introduces the methodology used for this study. The fourth chapter presents the findings of this research, focusing on the angular effects observed from SLSTR nadir and oblique data and analyses the results. The fifth section summarizes the findings and gives concluding remarks and prospectives. The organizational structure of this study is shown in the figure below.

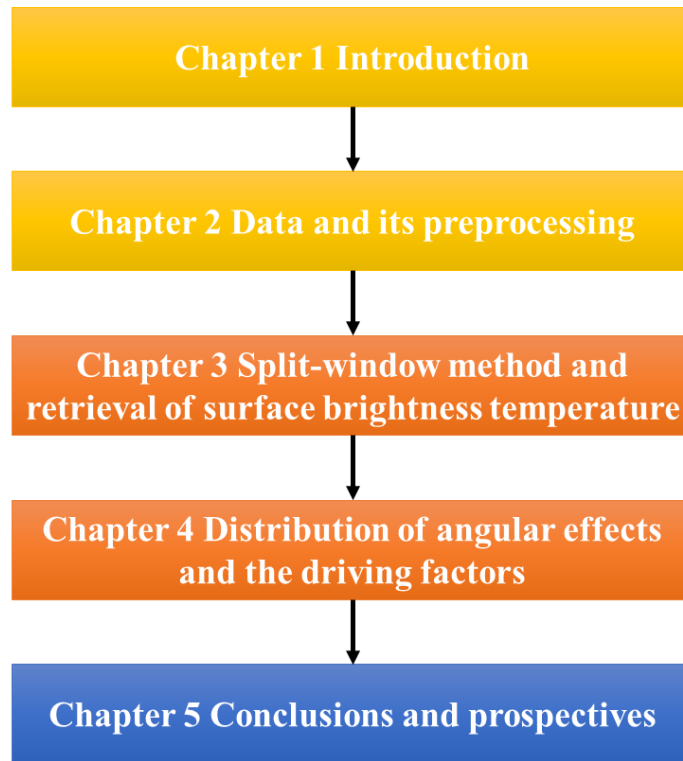


Fig 1.1 Structure chart of the dissertation.

## 2. Description of data used

The second chapter is concerned with the data utilized in this study. Sentinel-3A data were used to determine surface brightness temperature of nadir and oblique view. MCD12Q1 data and SRTM data were employed to define the study area. The emissivity spectra and TIGR database were utilized to generate a simulation database. The Köppen-Geiger climate classification map was applied to analyze the angular effect of surface brightness temperature. The CCI SM product was used to analyze the driving factors of the angular effect of surface brightness temperature.

### 2.1 Sentinel-3A data

Sentinel-3A was launched on February 16, 2016 as an important mission of the Global Monitoring for Environmental Security (GMES) program. Sentinel-3 satellite is equipped with several remote sensing instruments, including the Ocean and Land Colour Instrument (OLCI), SLSTR, SAR Radar ALtimeter (SRAL), Microwave Radiometer (MWR), Precise Orbit Determination (POD), as illustrated in Fig 2.1. The satellite is designed to observe sea and land surface temperature, sea surface topography, and ocean and land surface color with high precision and reliability, thereby enhancing climate monitoring, environmental monitoring, and ocean forecasting systems.

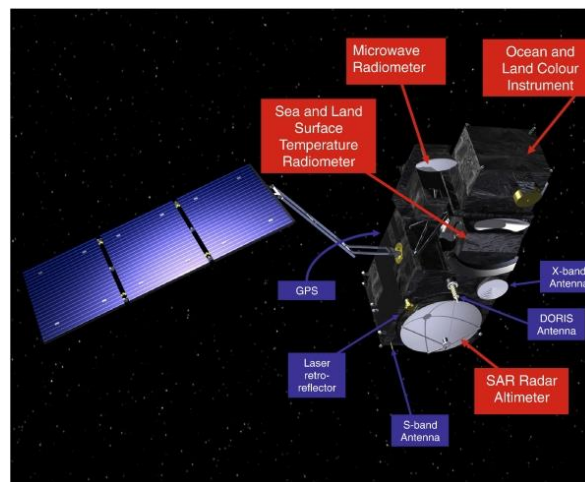


Fig 2.1 Structure of Sentinel-3 Satellite (Credits: European Satellite Agency).

Sentinel-3A operates in a high inclination orbit of  $98.65^\circ$ , providing exceptional coverage of ice and snow characteristics in high latitudes. Sentinel-3A follows a near-polar, sun-synchronous orbit at an altitude of 814.5 km, with a revisit period of 27 days and a local equatorial crossing time of 10:00 AM/PM.

The SLSTR sensor onboard Sentinel-3A is a conical scanning imaging radiometer, which is inherited from the (A)ATSR instrument series. The SLSTR instrument is designed with two independent observation angles: nadir and a backward-viewing zenith angle of  $55^\circ$ . The track of the Sentinel-3 SLSTR instrument, including nadir and oblique view, is shown in Fig 2.3. The swath of nadir view is approximately 1400 km, while the swath of oblique view is approximately 740 km. The main objective of SLSTR is to collect land and sea surface temperature dataset to support climate monitoring.



Fig 2.2 Track and scanning parameters of the Sentinel-3 SLSTR instrument with the nadir and oblique view (Credits: European Satellite Agency).

The SLSTR instrument includes the same seven spectral channels used in ASTR-2 and AATSR for each scan view, with the addition of two new channels at  $1.375 \mu\text{m}$  and  $2.25 \mu\text{m}$  for improved cloud detection. Table 2.1 presents nine channels of SLSTR, which range from visible to thermal infrared wavelengths, including three visible and near-infrared (VNIR) channels, three shortwave infrared (SWIR) channels, and three MIR/TIR channels (centered at  $0.555$ ,  $0.659$ ,  $0.865$ ,  $1.375$ ,  $1.610$ ,  $2.25$ ,  $3.74$ ,  $10.85$ , and  $12.0 \mu\text{m}$ ) (Zhang et al., 2019). In this thesis, two TIR channels were used to obtain

surface brightness temperature, and the spectral response functions for SLSTR S8 and S9 were depicted in Fig 2.3.

Table 2.1 Specifications of SLSTR sensor.

Band	Central Wavelength ( $\mu\text{m}$ )	Spatial resolution (km)	Radiometric resolution	Function
S1	0.555	0.5	SNR > 20 (a=0.5%)	Cloud screening, aerosol, vegetation monitoring
S2	0.659	0.5	SNR > 20 (a=0.5%)	NDVI, aerosol, vegetation monitoring
S3	0.865	0.5	SNR > 20 (a=0.5%)	NDVI, cloud flagging
S4	1.375	0.5	SNR > 20 (a=0.5%)	Cirrus detection
S5	1.61	0.5	SNR > 20 (a=0.5%)	Cloud clearing, ice, snow, vegetation monitoring
S6	2.25	0.5	SNR > 20 (a=0.5%)	Cloud clearing and vegetation state
S7	3.74	0.5	NE $\Delta$ T < 80 mK (T=270K)	Sea/Land surface temperature
S8	10.85	1	NE $\Delta$ T < 50 mK (T=270K)	Sea/Land surface temperature
S9	12	1	NE $\Delta$ T < 50 mK (T=270K)	Sea/Land surface temperature
F1	3.74	1	NE $\Delta$ T < 1 K (T<500 K)	Fire detection
F2	10.85	1	NE $\Delta$ T < 0.5 K (T<400 K)	Fire detection

a is top of atmosphere albedo, T is top of atmosphere brightness temperature, SNR is signal-to-noise ratio, and NE $\Delta$ T is noise equivalent difference temperature.

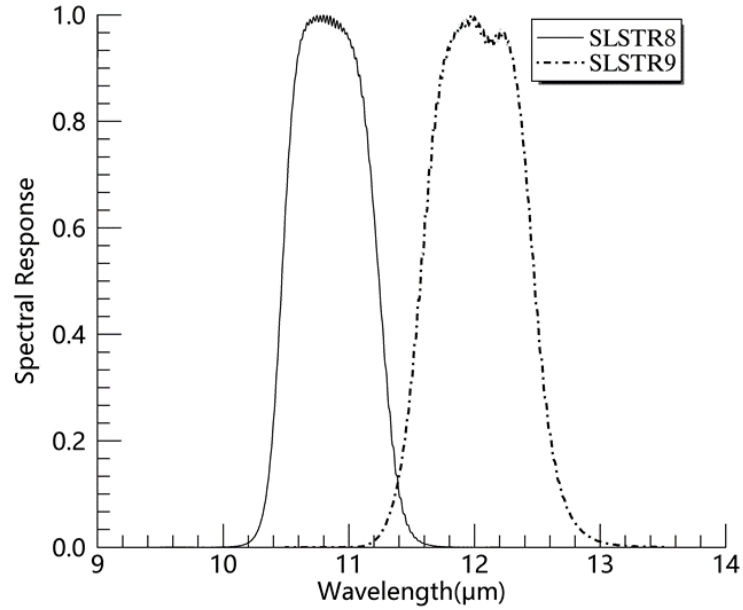


Fig 2.3 The spectral response functions at SLSTR S8 and S9.

The level 1 product provides at-sensor radiances for all visible and shortwave infrared channels at a spatial resolution of 0.5 km, brightness temperatures at the top of the atmosphere (TOA) for TIR channels at a spatial resolution of 1 km, as well as relevant annotation data for each view. This data is available for downloading from the ESA website (<https://scihub.copernicus.eu/dhus/#/home>).

The SLSTR level 1 product from October, 2019 to September, 2020 was selected to retrieve and analyze the angular effect on surface brightness temperature. Cloud flags extracted from SLSTR level1 data were used to select cloud-free data within a 3×3 km range. Only high-quality data (value = 0) was used. There were 27352 scenes at daytime and 27384 scenes at night time downloaded. Then SLSTR level1 data need to combine with the abnormal event table SLSTR\_Anomaly\_Events to filter available data. Since the SLSTR level 1 product has not been geometrically corrected, images from each band must undergo geometric correction based on the geographic lookup table (GLT) before retrieving surface brightness temperature. A GLT file contains the ground location for each pixel in an image. Using a GLT file, the nearest neighbor algorithm can be applied to perform geometric correction on the image.

For VNIR channels, SWIR channels, and MIR channel, the product provides radiance data, which needs to be converted using Eq (2.1):

$$Rad = DN * scale\_factor\_r \quad (2.1)$$

where  $Rad$  is the radiance at TOA, in  $W/(m^2 \cdot sr \cdot \mu m)$ ,  $DN$  is the value recorded in the image, and  $scale\_factor\_r$  is the conversion factor, which is 0.01. For the thermal infrared band, the product provides the TOA brightness temperature data, which needs to be converted using Eq (2.2):

$$BT = DN * scale\_factor\_b + offset\_b \quad (2.2)$$

where  $BT$  is the TOA brightness temperature on the satellite, in units of K,  $scale\_factor\_b$  is 0.01, and  $offset\_b$  is 283.73.

## 2.2 MCD12Q1 data

MODIS is a key instrument onboard the Earth Observing System (EOS) Terra and Aqua satellites. Terra was launched on December 18, 1999, followed by the successful launch of Aqua on May 4, 2002. The MODIS follows a near-polar orbit at an altitude of 705 km, with a local equatorial crossing time of 10:30 AM for Terra and 1:30 PM for Aqua. There are 36 channels for MODIS, ranging from visible to thermal infrared wavelengths (0.4-14.4  $\mu m$ ), including 2 channels at a nominal resolution of 250 m, 5 channels at 500 m, and 29 channels at 1 km. MODIS sensors are designed to support of ocean, land and atmosphere sciences.

The MCD12Q1 dataset, a MODIS Level 3 land cover type product generated from Terra and Aqua satellite observations at a spatial resolution of 500 m, was used in this thesis to identify the study area in Chapter 4. This dataset, available since 2001, provides annual global land cover data. It was created using MODIS reflectance data and supervised classification methods (Friedl et al., 2010). The MCD12Q1 data includes five different land cover classification methods (IGBP, UMD, LAI, BGC, and PFT), three datasets based on the Land Cover Classification System (LCCS), and additional quality control datasets. The IGBP classification scheme, employed in this thesis, utilizes a decision tree classification to classify global feature types into 17 categories, including evergreen needleleaf forests, evergreen broadleaf forests, deciduous needleleaf forests, deciduous broadleaf forests, mixed forests, closed shrublands, open shrublands, woody savannas, savannas, grasslands, permanent wetlands, croplands, urban and built-up lands, cropland/natural vegetation mosaic, permanent snow and ice, barren or sparsely vegetated, and water bodies. Details of the IGBP classification are shown in Table 2.2. The MCD12Q1 data can be downloaded

from the USGS website ([https://lpdaac.usgs.gov/dataset\\_discovery/modis/modis\\_products\\_table/mcd12q1](https://lpdaac.usgs.gov/dataset_discovery/modis/modis_products_table/mcd12q1)).

Table 2.2 Land cover types and their description by IGBP classification strategy in MCD12Q1 product.

IGBP_Name	Value	Description
Evergreen needleleaf forests	1	Dominated by evergreen conifer trees (canopy >2m). Tree cover >60%.
Evergreen broadleaf forests	2	Dominated by evergreen broadleaf and palmate trees (canopy >2m). Tree cover >60%.
Deciduous needleleaf forests	3	Dominated by deciduous needleleaf (larch) trees (canopy >2m). Tree cover >60%.
Deciduous broadleaf forests	4	Dominated by deciduous broadleaf trees (canopy >2m). Tree cover >60%.
Mixed forests	5	Dominated by neither deciduous nor evergreen (40-60% of each) tree type (canopy >2m). Tree cover >60%.
Closed Shrublands	6	Dominated by woody perennials (1-2m height) >60% cover.
Open shrublands	7	Dominated by woody perennials (1-2m height) 10-60% cover.
Woody savannas	8	Tree cover 30-60% (canopy >2m).
Savannas	9	Tree cover 10-30% (canopy >2m).
Grasslands	10	Dominated by herbaceous annuals (<2m).
Permanent wetlands	11	Permanently inundated lands with 30-60% water cover and >10% vegetation cover.
Croplands	12	At least 60% of the area is cultivated cropland.
Urban and built-up lands	13	At least 30% impervious surface area including building materials, asphalt, and vehicles.
Cropland/natural vegetation mosaics	14	Mosaics of small-scale cultivation 40-60% with natural tree, shrub, or herbaceous vegetation.
Permanent snow and ice	15	At least 60% of the area is covered by snow and ice for at least 10 months of the year.
Barren/sparsely vegetated	16	At least 60% of area is non-vegetated barren (sand, rock, soil) areas with less than 10% vegetation.
Water Bodies	17	At least 60% of the area is covered by permanent water bodies.
Unclassified	255	Has not received a map label because of missing inputs.

## 2.3 SRTM data

Shuttle Radar Topographic Mission (SRTM) data was utilized in this study to obtain global elevation data and to filter for elevation uniformity. The SRTM data were measured by NASA in collaboration with the United States Department of Defense's National Mapping Agency (NGA) and the German and Italian space agencies. The mission was commenced on February 11, 2000, and lasted 11 days, with the SRTM system aboard the Space Shuttle Endeavour. Radar imagery was collected between 60° N and 56° S, covering more than 80% of the Earth's land area. In April and October 1994, the space shuttle deployed the C-band Spaceborne Imaging Radar and the X-Band Synthetic Aperture Radar (X-SAR) technology to acquire data on the Earth's surface. For the SRTM mission, the technology was upgraded to gather interferometric radar data, which compares two radar pictures or signals taken from slightly different angles. This mission employed single-pass interferometry, collecting two signals simultaneously using two distinct radar antennas: one data board the space shuttle and the other at the end of a 60-meter mast extending from the shuttle. Surface elevation was calculated by analyzing the differences between the two signals.

The processed SRTM radar data can be adapted to the requirements of the military, public, and scientific users. The SRTM product was released in 2003 as a digital elevation model with 30 m and 90 m spatial resolutions after two years of data processing. The elevation file with a spatial resolution of 30 m comprises 3601 x 3601 elevations, whereas the elevation file with a spatial resolution of 90 m has 1201 x 1201 elevations. The SRTM data can be downloaded at the USGS website (<https://earthexplorer.usgs.gov/>)

## 2.4 Emissivity spectra database

In this study, the ECOSTRESS spectral library version 1.0 was used to determine the emissivity in the simulation database. On February 2, 2018, the ECOSTRESS spectral library version 1.0 was released (<http://speclib.jpl.nasa.gov>). The ECOSTRESS spectral library was developed and expanded from ASTER spectral library version 2.0 (Baldrige et al., 2009; Meerdink et al., 2019). Data from the U.S. Geological Survey (USGS), Johns Hopkins University (JHU), and Jet Propulsion Laboratory (JPL) were compiled in the ECOSTRESS spectral library. The edition

includes more than 3400 reflectivity spectra of both natural and artificial materials, covering the wavelength range of 0.35–15.4  $\mu\text{m}$ .

The spectral library is broadly categorized based on surface types: vegetation, rocks, minerals, meteorites, soils, non-photosynthetic vegetation (NPV), snow and ice, water bodies, and man-made materials. Each spectrum file includes header data along with wavelength and associated reflectance information. A total of 53 spectra were selected (41 soil samples, 4 vegetation samples, and 8 samples of water bodies, snow and ice) as shown in Fig 2.4 to obtain land surface emissivity (LSE) by Eq (2.3):

$$X_i = \frac{\int f_i(\lambda) X(\lambda) d\lambda}{\int f_i(\lambda) d\lambda} \quad (2.3)$$

where  $f_i(\lambda)$  is the value of the spectral response function at wavelength  $\lambda$  for channel  $i$  as shown in Fig 2.3.  $X(\lambda)$  is the emissivity at wavelength  $\lambda$ , which is obtained by 1- reflectivity using the Kirchhoff's law.

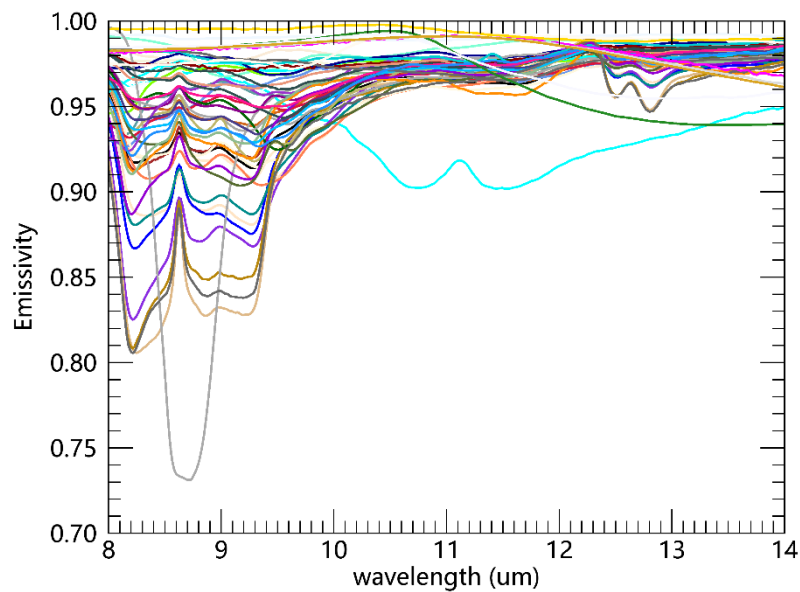


Fig 2.4 53 Selected emissivity spectra from ECOSTRESS spectral library.

## 2.5 Thermodynamic Initial Guess Retrieval (TIGR) database

The Thermodynamic Initial Guess Retrieval (TIGR) database was used as input parameters to establish a simulation database. Developed by the Dynamic Meteorology Laboratory since 1985 (Chedin and Scott, 1985), TIGR version 2000 provides 2311 representative atmospheric profiles, including pressures, temperatures, water vapor and ozone profiles across 40 levels. These meteorological circumstances were categorized into five types in ascending order: Tropical (profiles 1 to 872), temperate -Midlat1- (profiles 873 to 1260), cold temperate and summer polar -Midlat2- (profiles 1261 to 1614), Northern Hemisphere very cold polar -polar1- (profiles 1615 to 1718), and winter Polar -Polar2- (profiles 1719 to 2311) (Chedin et al., 1994). The TIGR database is available online (<https://www.aeris-data.fr/tigr-databank-access/>).

As only clear-sky conditions were considered for LST retrieval, cloudy atmospheric profiles in the TIGR database were excluded. Cloudy atmospheric profiles were identified based on two criteria: relative humidity was greater than 90% at any level, and relative humidity was greater than 85% across two consecutive levels of the profile. After filtering, 1416 cloud-free atmospheric profiles remained in the TIGR database. From these, sixty cloud-free atmospheric profiles with well-representative of global atmospheric and surface situations were selected. The WVC ranged from 0 to 6.5 g/cm<sup>2</sup>, while atmospheric temperature ( $T_0$ ) in the first boundary layer of each atmospheric profile ranged from 230 K to 310 K. Fig 2.5 shows a scatterplot of the WVC and  $T_0$  in the first boundary layer of 60 selected atmospheric profiles. This figure demonstrates a nonlinear relationship between WVC and  $T_0$ .

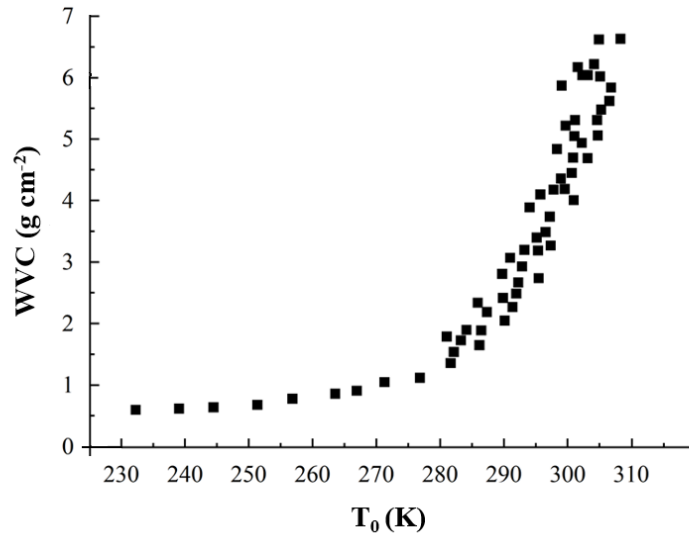


Fig 2.5 Scatterplot of WVC and  $T_0$  in the first boundary layer of 60 selected atmospheric profiles.

## 2.6 Köppen-Geiger climate classification map

In this thesis, the angular effect of surface brightness temperature was analyzed in conjunction with climate classification. The Köppen-Geiger climate classification system categorizes climate zones worldwide based on local vegetation. Wladimir Köppen first established this approach in the late nineteenth century, recognizing the close relationship between vegetation and climate. Temperature and precipitation are the two primary climatic variables influencing vegetation growth. Forests typically thrive in regions with higher precipitation and temperatures, while deserts are prevalent in areas with lower precipitation.

The system divided the globe into five main climate types: tropical (A), arid (B), temperate (C), cold (D), and polar (E) climates. Each type is further subdivided into 30 sub-types based on temperature or aridity. Köppen's classification map has undergone multiple revisions and improvements since its initial publication. A new version of this map, published in 2018, offers 1-km resolution data for both historical and future climate conditions (1901–2099) (Beck et al., 2018). Fig 2.6 illustrates the global distribution of climates across the five Köppen-Geiger types. Table 2.3 lists the criteria to which the functions used to classify the temperature and precipitation data is according. The Köppen-Geiger climate classification map is available online (<https://www.gloh2o.org/koppen/>)

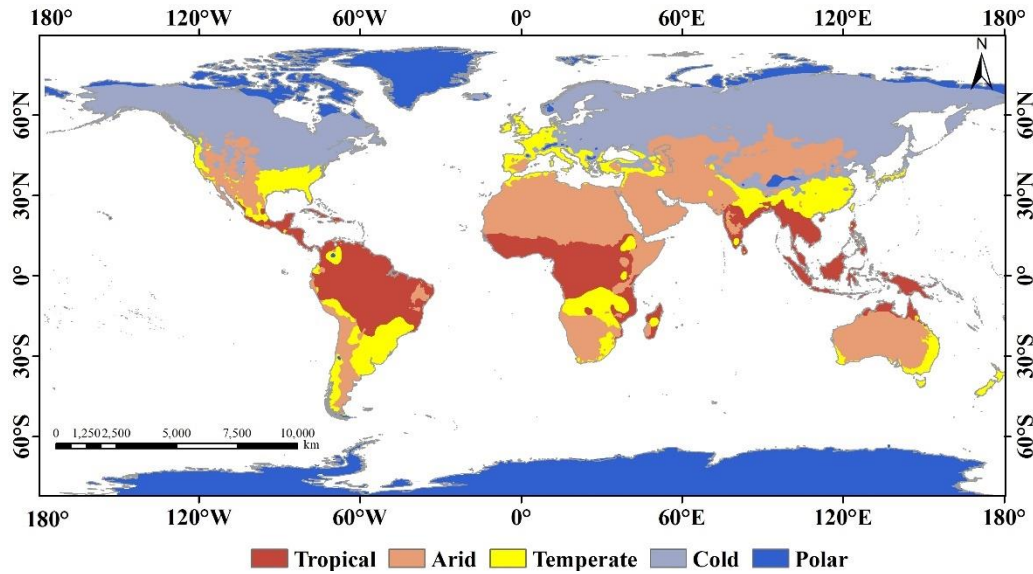


Fig 2.6 The Köppen-Geiger climate classification map in five main climate types (tropical, arid, temperate, cold, and polar climates).

Table 2.3 Climate classes and their defining criteria.

Code	Description	Criterion
A	Tropical	Not (B) & $T_{cold} \geq 18$
B	Arid	$MAP < 10 \times P_{threshold}$
C	Temperate	Not (B) & $T_{hot} > 10$ & $0 < T_{cold} < 18$
D	Cold	Not (B) & $T_{hot} > 10$ & $T_{cold} \leq 0$
E	Polar	Not (B) & $T_{hot} \leq 10$

$MAT$ =mean annual air temperature ( $^{\circ}\text{C}$ );  $MAP$ = mean annual precipitation ( $\text{mm y}^{-1}$ );  $T_{cold}$ = the air temperature of the coldest month ( $^{\circ}\text{C}$ );  $T_{hot}$ = the air temperature of the warmest month ( $^{\circ}\text{C}$ );  $P_{threshold} = 2 \times MAT$  if  $>70\%$  of precipitation falls in winter,  $P_{threshold} = 2 \times MAT + 28$  if  $>70\%$  of precipitation falls in summer, otherwise  $P_{threshold} = 2 \times MAT + 14$ . Summer (winter) is the six-month period that is warmer (colder) between April-September and October-March.

## 2.7 ESA climate change initiative plus soil moisture

The ESA CCI Soil Moisture (SM) Level 3 product was used to analyze the driving factors of angular effects in this thesis. The CCI SM V07.1 products consists of three datasets: the active product created by fusing scatterometer products including Active Microwave Instrument Wind Scatterometer (AMI-WS) and the Advanced Scatterometer (ASCAT), the passive product created by fusing radiometer products

including the Scanning Multi-channel Microwave Radiometer (SMMR), the Special Sensor Microwave Imager (SSM/I), the Advanced Microwave Scanning Radiometer for EOS (AMSR-E), AMSR2, and the Soil Moisture Active Passive (SMAP) etc., and combined product blended the former two datasets. In this study, the combined product was used considering its relatively better accuracy and spatial coverage. CCI SM product can be accessed from ESA website (<https://climate.esa.int/en/projects/soil-moisture/data/>).

The products are provided as NetCDF-4 classic format and comprise merged surface soil moisture measurements at a spatial resolution of  $0.25^\circ$  with a global coverage. The grid is a  $0.25^\circ \times 0.25^\circ$  longitude-latitude global array of points based on the World Geodetic System 1984 (WGS 84) reference system, with a dimension of 1440 columns and 720 rows. The temporal resolution of CCI SM product is 1 day with a reference time at 0:00 UTC with a global coverage. The temporal coverage of the dataset spans from 1978 to 2021, covering more than 40 years. The soil moisture data are provided in volumetric units [ $\text{m}^3 / \text{m}^3$ ]. The theoretical and algorithmic basis of the CCI SM product can be found in the report of Dorigo et al. (2023).

## 3. Surface brightness temperature retrieval algorithm on Sentinel-3A satellite

The third chapter presents the SW algorithm applied on TOA brightness temperatures from Sentinel-3A satellite to obtain the surface brightness temperature. Surface brightness temperatures can be retrieved using the split-window method by combining two adjacent infrared channels to reduce atmospheric effects. It is focusing on four key themes. The first section of this chapter covers the process of deriving the radiative transfer equation for the SW algorithm of the surface brightness temperature. In the second section the simulation of surface brightness temperature is conducted. The coefficients are determined, and the performance of algorithm is analyzed in the third and fourth sections.

### 3.1 Development of SW algorithm

The SW algorithm was derived from radiative transfer theory, incorporating specific assumptions (Coll and Caselles, 1997). The measured radiance received by thermal infrared sensors comes primarily from the Earth's surface and the atmosphere. Under cloud-free conditions, assuming local thermal equilibrium, the general radiative transfer equation can be expressed as Eq (3.1), without considering solar scattering radiance.

$$B_i(T_i) = \tau_i B_i(T_{gi}) + R_{ati}^{\uparrow} \quad (3.1)$$

where  $T_i$  is the TOA brightness temperature and  $T_{gi}$  is the surface brightness temperature in channel  $i$ , also called ground brightness temperature;  $B$  represents the Planck function;  $\tau_i$  is the atmospheric transmittance of the channel  $i$ ;  $R_{ati}^{\uparrow}$  is the atmospheric upwelling radiance of the channel  $i$ . The reflected solar radiance is negligible in 8-14  $\mu\text{m}$  at both daytime and nighttime and in 3-5  $\mu\text{m}$  during the night.  $B_i(T_{gi})$  is the surface-leaving radiance observed in channel  $i$ , which can be written as:

$$B_i(T_{gi}) = \varepsilon_i B_i(T_s) + (1 - \varepsilon_i) R_{at}^\downarrow \quad (3.2)$$

where  $\varepsilon_i$  is the land surface emissivity (LSE) in channel  $i$ ;  $T_s$  is LST;  $R_{at}^\downarrow$  is the atmospheric downwelling radiance of the channel  $i$ . And  $R_{at}^\uparrow$  can be defined with the mean value theorem (McMillin, 1975)

$$B_i(T_{ai}) = \frac{R_{at}^\uparrow}{1 - \tau_i} \quad (3.3)$$

where  $T_{ai}$  is the equivalent atmospheric temperature in channel  $i$ . Then inserting Eq (3.3) into Eq (3.4) produces

$$B_i(T_i) = \tau_i B_i(T_{gi}) + (1 - \tau_i) B_i(T_{ai}) \quad (3.4)$$

Similarly, another channel  $j$  can be written as Eq (3.4)

$$B_j(T_j) = \tau_j B_j(T_{gj}) + (1 - \tau_j) B_j(T_{aj}) \quad (3.5)$$

To obtain the SW equation, it is also required to simplify by linearizing Planck's function around a temperature reference. To accomplish this, assuming  $T_{ai}$ ,  $T_i$ , and  $T_{gi}$  are near to each other so does channel  $j$ . Then, Eq (3.4) and Eq (3.5) compute the first derivative at  $T_i$ , as follows:

$$T_i = \tau_i (T_{gi} - T_{ai}) + T_{ai} \quad (3.6)$$

$$T_j = \tau_j (T_{gj} - T_{aj}) + T_{aj} \quad (3.7)$$

$T_{ai}$  and  $T_{aj}$  can be expressed using a linear relationship (Coll et al., 1994a; Coll et al., 1994b; Zheng et al., 2019),

$$T_{ai} = \alpha T_{aj} + \beta \quad (3.8)$$

where  $\alpha$  and  $\beta$  are constants. By combining Eq (3.6) and Eq (3.7) with the relation Eq (3.8), the  $T_{ai}$  and  $T_{aj}$  can be eliminated between both equations, allowing for the formulation of SW function in terms of  $T_{gi}$ ,  $T_i$ , and  $T_j$ .

$$T_{gi} = A_0 + A_1 T_i + A_2 (T_i - T_j) + A_3 \quad (3.9)$$

with

$$A_0 = \frac{\beta(\tau_i - 1)(\tau_j - 1)}{\tau_i(\tau_j - 1) - \alpha\tau_j(\tau_i - 1)} \quad (3.10)$$

$$A_1 = \frac{(\tau_j - 1) - \alpha(\tau_i - 1)}{\tau_i(\tau_j - 1) - \alpha\tau_j(\tau_i - 1)} \quad (3.11)$$

$$A_2 = \frac{\alpha(\tau_i - 1)}{\tau_i(\tau_j - 1) - \alpha\tau_j(\tau_i - 1)} \quad (3.12)$$

and

$$A_3 = \frac{\alpha\tau_j(1 - \tau_i)}{\tau_i(\tau_j - 1) - \alpha\tau_j(\tau_i - 1)} (T_{gi} - T_{gj}) \quad (3.13)$$

$A_0$ ,  $A_1$ , and  $A_2$  can be considered as constants.  $A_3$  is small and can be regarded as either a linear or quadratic function of  $(T_i - T_j)$ . The optimal balance between retrieval accuracy and method simplicity appears to be a quadratic expression in Eq (3.14)

$$T_g = a_0 + a_1 T_i + a_2 (T_i - T_j) + a_3 (T_i - T_j)^2 \quad (3.14)$$

where  $a_0$ ,  $a_1$ ,  $a_2$ , and  $a_3$  are constants depend on atmospheric conditions. The introduction of the quadratic item  $a_3(T_i - T_j)^2$  further improves the retrieval accuracy of  $T_g$ .

## 3.2 Establishment of simulation database

Thermal infrared radiation received by sensors is often influenced by atmospheric absorption and emission. Atmospheric radiative transfer modeling software provides an effective means to simulate atmospheric radiation transfer processes and perform atmospheric correction on remote sensing images. In this study, the atmospheric radiative transfer software MODerate resolution atmospheric TRANsmission (MODTRAN) was used to simulate the atmosphere and derive atmospheric parameters.

In the late 1980s, the US Air Force Research Laboratory (AFRL) and Spectrum Sciences Inc. (SSI) collaborated to develop MODTRAN (Berk et al., 2011).

MODTRAN is based on the LOWTRAN model. It incorporates multiple scattering computations, an expandable molecular database, and improves spectral resolution from  $20 \text{ cm}^{-1}$  to  $0.1 \text{ cm}^{-1}$ . MODTRAN also provides additional parameters for aerosol patterns, transport pathways, and transmittance. It includes six common atmospheric models for various climate types and latitudinal band distributions. MODTRAN includes six common atmospheric models for various climate types and latitudinal zone distributions: tropical, Mid-Latitude Summer (MLS), Mid-Latitude Winter (MLW), Sub-Arctic Summer (SAS), and Sub-Arctic Winter (SAW), as well as the 1976 Standard Atmospheric Model from the United States. Fig 3.1 presents the temperature profiles of six common atmospheric models built into MODTRAN. In addition to these preset models, the user can customize the atmospheric models to meet specific needs by inputting atmospheric profile data for simulation and batch computations.

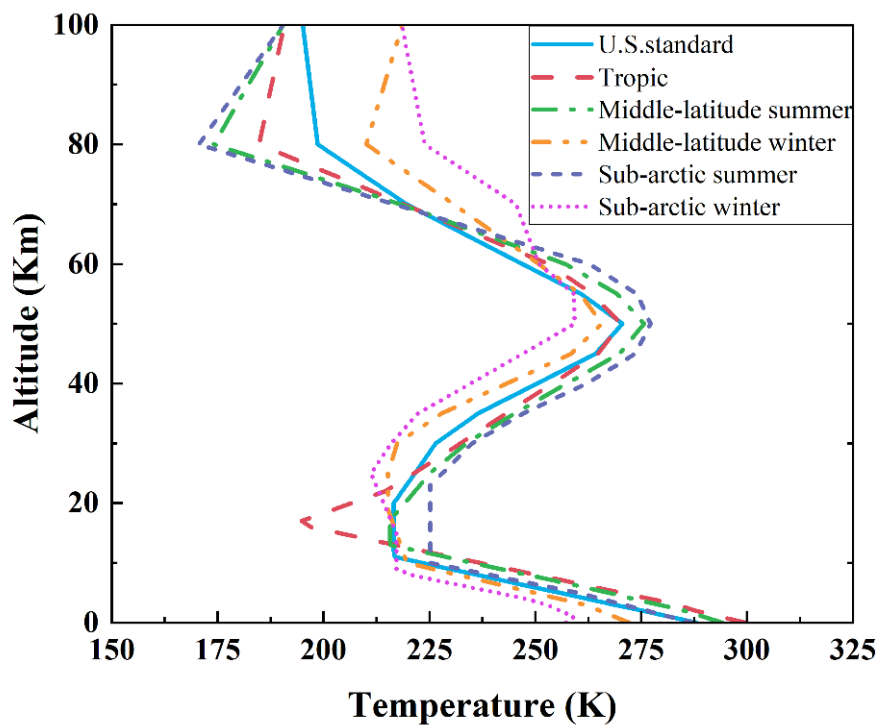


Fig 3.1 Temperature profiles of the MODTRAN model atmospheres

Users can install MODTRAN software or simulate atmospheric transmission through the MODTRAN website ([http://modtran.spectral.com/modtran\\_index](http://modtran.spectral.com/modtran_index)). The website allows for quick selection of atmospheric modes and aerosol models, defining necessary atmospheric, sensor, and ground parameters, and estimating atmospheric

transmittance, upwelling radiance, downwelling radiance, and more.

Since the surface temperature retrieval from thermal infrared data is only applicable under clear-sky conditions, the atmospheric profiles under clear-sky conditions from the TIGR2000 database are selected. When the relative humidity value of a layer in an atmospheric profile is higher than 90%, this atmospheric profile is considered as cloudy condition. Based on the above rules, 1416 cloud-free atmospheric profiles were finally selected, and 60 atmospheric profiles with atmospheric water vapor content between  $0.06 \text{ g/cm}^2$  and  $6.5 \text{ g/cm}^2$  were selected from the cloud-free atmospheric profiles, which cover almost all atmospheric conditions on a global scale. These 60 profiles are used as inputs to MODTRAN to simulate the atmospheric parameters.

The air temperature ( $T_0$ ) in the bottom layer of each atmospheric profile ranged from 230 to 320 K. To better simulate the correlation between  $T_0$  and  $T_s$ , the input  $T_s$  was varied with  $T_0$  for each profile. when  $T_0$  exceeded 280 K,  $T_s$  ranged from  $T_0 - 5 \text{ K}$  to  $T_0 + 10 \text{ K}$ , with an interval of 5 K. when  $T_0$  was less than or equal to 280 K,  $T_s$  ranged from  $T_0 - 5 \text{ K}$  to  $T_0 + 5 \text{ K}$ , with the same interval. In the simulations, the average emissivity was set to vary from 0.94 to 1.0, with an interval of 0.02. The soil emissivity for the two thermal infrared channels of SLSTR ranges from 0.959 to 0.981, as shown in Fig 3.2. Meanwhile, the emissivity difference ranged from -0.02 to 0.02, with a step of 0.005. Consequently, the simulation dataset comprised 8,316 different cases. The flowchart for generating the simulated dataset is shown as Fig 3.3.

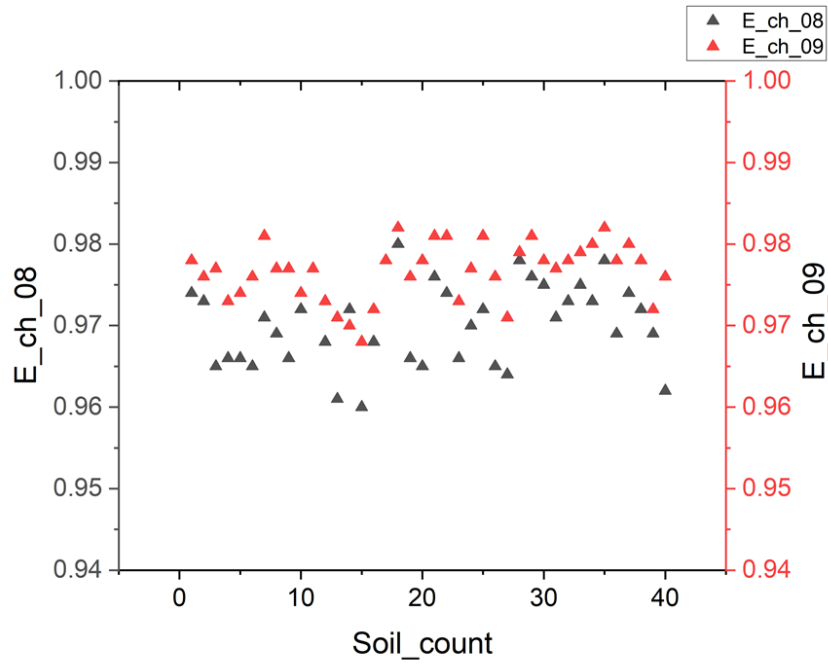


Fig 3.2 the soil emissivity in the two thermal infrared channels of the SLSTR. The black and red dots represent the soil emissivity at  $10.85\mu\text{m}$  and  $12\mu\text{m}$ , respectively.

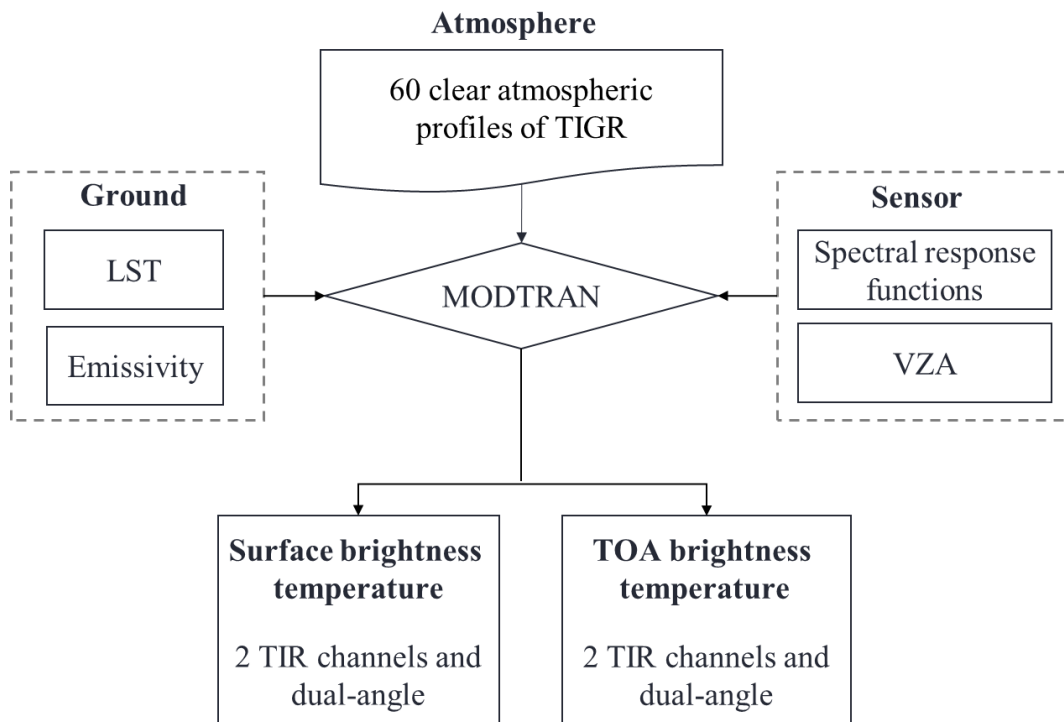


Fig 3.3 Flowchart of generating a simulated dataset

Following data preparation, the flowchart shows the steps involved in generating a simulated database. The specific steps are outlined below:

Firstly, create a tape5 input file in which five types of parameters are configured

based on the input data and the study's requirements. The first type sets MODTRAN's driving parameters, the second type sets aerosol and cloud parameters, the third type specifies the geometrical parameters of the sensors, the fourth type defines the spectral range and spectral resolution, and the fifth type sets the options for repeated runs of the atmospheric profiles.

Second, the path to the tape5 file is entered into the 'mod5root.in' file. Use the 'Console2.exe' application to simulate and generate the output files tape6 and tape7, which contain the calculation process file and the result file for the atmospheric parameters, respectively.

Third, the tape7 file contains each spectrum's atmospheric transmittance, emissivity, atmospheric upwelling radiance, atmospheric water vapor content, atmospheric downwelling radiance, atmospheric scattering, ground reflection, and total radiance. The atmospheric parameters for the channel can be determined by convolving them with the sensor's spectral response function.

### Chapter 3. Surface brightness temperature retrieval algorithm on Sentinel-3A satellite

```

TMF+7F  2   1  -1   0   0   0   0   0   0   0   1   0 294.050  0.020
FTT  8  0.    380.    0    00F  F  F    0.000
  1   0   0   3   0   0  0.00000  0.00000  0.00000  0.00000  0.00200
40   0   0   TIGR clear cloud
  0.0021.013E+0032.940E+0026.967E+0010.000E+0000.000E+000AAH2C222222222
  0.5029.551E+0022.919E+0026.559E+0010.000E+0000.000E+000AAH2C222222222
  0.9979.003E+0022.884E+0027.143E+0010.000E+0000.000E+000AAH2C222222222
  1.4848.489E+0022.848E+0027.817E+0010.000E+0000.000E+000AAH2C222222222
  1.9858.000E+0022.859E+0025.042E+0010.000E+0000.000E+000AAH2C222222222
  2.8097.248E+0022.847E+0023.380E+0010.000E+0000.000E+000AAH2C222222222
  3.6806.510E+0022.802E+0024.889E+0010.000E+0000.000E+000AAH2C222222222
  4.5305.848E+0022.750E+0025.340E+0010.000E+0000.000E+000AAH2C222222222
  5.3705.250E+0022.698E+0025.509E+0010.000E+0000.000E+000AAH2C222222222
  6.1814.719E+0022.644E+0025.949E+0010.000E+0000.000E+000AAH2C222222222
  6.9764.239E+0022.587E+0026.168E+0010.000E+0000.000E+000AAH2C222222222
  7.7513.807E+0022.529E+0026.279E+0010.000E+0000.000E+000AAH2C222222222
  8.5053.420E+0022.469E+0026.322E+0010.000E+0000.000E+000AAH2C222222222
  9.2403.072E+0022.409E+0024.769E+0010.000E+0000.000E+000AAH2C222222222
  9.9402.760E+0022.340E+0026.152E+0010.000E+0000.000E+000AAH2C222222222
10.6172.479E+0022.271E+0027.944E+0010.000E+0000.000E+000AAH2C222222222
11.3012.226E+0022.214E+0027.598E+0010.000E+0000.000E+000AAH2C222222222
11.9682.000E+0022.158E+0027.275E+0010.000E+0000.000E+000AAH2C222222222
13.2841.620E+0022.069E+0026.821E+0010.000E+0000.000E+000AAH2C222222222
14.5451.312E+0021.980E+0026.443E+0010.000E+0000.000E+000AAH2C222222222
15.8151.063E+0021.911E+0026.207E+0010.000E+0000.000E+000AAH2C222222222
17.3238.607E+0011.919E+0026.231E+0010.000E+0001.000E-003AAH2C222222222
19.2236.971E+0012.026E+0021.145E+0010.000E+0001.000E-003AAH2C222222222
20.9395.646E+0012.073E+0022.536E+0000.000E+0002.000E-003AAH2C222222222
22.4684.573E+0012.074E+0021.090E+0000.000E+0004.000E-003AAH2C222222222
24.1773.704E+0012.111E+0027.310E-0010.000E+0007.000E-003AAH2C222222222
27.4682.479E+0012.177E+0022.200E-0010.000E+0001.100E-002AAH2C222222222
30.7611.660E+0012.231E+0027.700E-0020.000E+0001.400E-002AAH2C222222222
34.1001.111E+0012.281E+0023.000E-0020.000E+0001.500E-002AAH2C222222222
37.4217.740E+0002.364E+0029.000E-0030.000E+0001.500E-002AAH2C222222222
41.5564.980E+0002.460E+0022.000E-0030.000E+0001.300E-002AAH2C222222222
45.6893.330E+0002.578E+0021.000E-0030.000E+0001.100E-002AAH2C222222222
49.2762.230E+0002.621E+0020.000E+0000.000E+0008.000E-003AAH2C222222222
52.3281.500E+0002.606E+0020.000E+0000.000E+0006.000E-003AAH2C222222222
55.2521.000E+0002.573E+0020.000E+0000.000E+0004.000E-003AAH2C222222222
59.9065.500E-0012.563E+0020.000E+0000.000E+0003.000E-003AAH2C222222222
63.8823.000E-0012.491E+0020.000E+0000.000E+0002.000E-003AAH2C222222222
67.2581.700E-0012.405E+0020.000E+0000.000E+0001.000E-003AAH2C222222222
70.8709.000E-0022.309E+0020.000E+0000.000E+0000.000E+000AAH2C222222222
74.0515.000E-0022.221E+0020.000E+0000.000E+0000.000E+000AAH2C222222222
100.000    0.002  180.000    0.000    0.000    0.000    0    0.000
    680    1333    1.0000    10
1

```

Fig 3.4 Example of tp5 file

```

TMF 7 2 1 -1 0 0 0 0 0 0 0 1 0 294.050 0.020
1 1 1 3 0 0 23.00000 0.00000 0.00000 0.00000 0.00000 0.00200
-99.000 -99.000 -99.000
-99.00000 -99.00000 -99.00000 3.411557 0.000712 H2O & O3 COLUMNS [GM/CM2]
40 TIGR clear cloud
74.05100 0.00200 180.00000 74.04900 0.00000 0.00000 0 0.00000
-99 -99 -99 -99
-99.000000 -99.000000 -99.000000 -99.000000 -99.000000 -99.000000 -99.000000 -99.000000
680.0 1333.0 1.0 10.0NW
1 0 0.000 0 0.000 0 1.000
FREQ TOT_TRANS PTH_THRML THRML_SCT SURF_EMIS SOL_SCAT SING_SCAT GRND_RFLT DRCT_RFLT TOTAL_RAD REF_SOL SOL@OBS DEPTH DIR_EM TOA_SUN BBODY_T[K]
680.00 0.00000000 4.5046E-06 1.0158E-11 2.8583E-27 5.8189E-29 4.5046E-06 49.912 0.9800 220.734
681.00 0.00000000 4.4672E-06 1.1304E-11 2.8495E-26 5.8006E-28 4.4672E-06 47.612 0.9800 220.432
682.00 0.00000000 4.4224E-06 1.2591E-11 9.0790E-26 1.8479E-27 4.4224E-06 46.453 0.9800 220.047
683.00 0.00000000 4.3706E-06 1.3666E-11 3.6440E-24 7.4116E-26 4.3706E-06 42.759 0.9800 219.581
684.00 0.00000000 4.3257E-06 1.4846E-11 4.5052E-23 9.1654E-25 4.3257E-06 40.244 0.9800 219.191
685.00 0.00000000 4.2745E-06 1.6472E-11 3.6970E-22 7.5229E-24 4.2745E-06 38.138 0.9800 218.726
686.00 0.00000000 4.2281E-06 1.8068E-11 4.2403E-20 8.6249E-22 4.2281E-06 33.395 0.9800 218.313
687.00 0.00000000 4.1870E-06 1.9510E-11 3.2849E-19 6.6814E-21 4.1870E-06 31.348 0.9800 217.958
688.00 0.00000000 4.1466E-06 2.1253E-11 2.5913E-17 5.2705E-19 4.1466E-06 26.978 0.9800 217.607
689.00 0.00000000 4.1234E-06 2.3556E-11 2.0304E-16 4.1297E-18 4.1234E-06 24.919 0.9800 217.451
690.00 0.00000000 4.1025E-06 2.5948E-11 4.9640E-16 1.0094E-17 4.1025E-06 24.025 0.9800 217.323
691.00 0.00000000 4.0820E-06 2.8488E-11 8.7236E-15 1.7710E-16 4.0820E-06 21.157 0.9800 217.197
692.00 0.00000001 4.0820E-06 3.1372E-11 7.4963E-14 1.5217E-15 4.0820E-06 19.006 0.9800 217.308
693.00 0.00000002 4.0907E-06 3.4610E-11 2.5898E-13 5.2579E-15 4.0907E-06 17.766 0.9800 217.519
694.00 0.00000005 4.1083E-06 3.8161E-11 6.6332E-13 1.3466E-14 4.1083E-06 16.825 0.9800 217.831
695.00 0.00000010 4.1433E-06 4.1907E-11 1.3064E-12 2.6523E-14 4.1433E-06 16.146 0.9800 218.340
696.00 0.00000018 4.1947E-06 4.5602E-11 2.4093E-12 4.8908E-14 4.1947E-06 15.534 0.9800 219.034
697.00 0.00000047 4.2645E-06 5.0230E-11 6.3098E-12 1.2805E-13 4.2645E-06 14.570 0.9800 219.930
698.00 0.00000122 4.3484E-06 5.5727E-11 1.6333E-11 3.3137E-13 4.3485E-06 13.618 0.9800 220.974
699.00 0.00000403 4.4402E-06 6.2378E-11 5.4002E-11 1.0943E-12 4.4403E-06 12.421 0.9800 222.093
700.00 0.00001339 4.5506E-06 7.2443E-11 1.7920E-10 3.6259E-12 4.5508E-06 11.221 0.9800 223.401

```

Fig 3.5 Example of tp7 file

Additionally, users can install MODTRAN software or simulate atmospheric transmission through the MODTRAN website ([http://modtran.spectral.com/modtran\\_index](http://modtran.spectral.com/modtran_index)). The website allows for quick selection of atmospheric modes and aerosol models, defining necessary atmospheric, sensor, and ground parameters, and estimating atmospheric transmittance, upwelling radiance, downwelling radiance, and more.

### 3.3 Determination of SW coefficients for Sentinel-3A SLSTR

The atmospheric parameters for two thermal infrared channels output from MODTRAN are used to derive surface radiance and surface brightness temperature. The split-window algorithm coefficients for SLSTR data were determined by least-squares regression analysis in combination with the simulated data. In the least squares method,  $T_i$ ,  $(T_i - T_j)$ ,  $(T_i - T_j)^2$  were set as independent variables,  $T_{gi}$  is set as dependent variable.

The coefficients of SW algorithm were regressed from nadir and oblique TIR channels, respectively.  $a_0$ ,  $a_1$ ,  $a_2$ , and  $a_3$  in Eq (3.14) has been constructed from Table 3.1.

Table 3.2 The coefficients of SW algorithm at nadir and oblique view

Observation view	$a_0$	$a_1$	$a_2$	$a_3$
Nadir view	-5.58	1.02	0.37	0.41
Oblique view	-5.49	1.02	0.11	0.57

The scatterplot scatter plots of actual and estimated surface brightness temperature at nadir view and oblique view are shown in Fig 3.6. Surface brightness temperature at nadir view fits the data better than oblique view. The root-mean-square error (RMSE) of the surface brightness temperature is 0.74 K at nadir view and 1.23 K at oblique view. With the increase of surface brightness temperature and WVC shown in Fig 3.7, the fitting get worse.

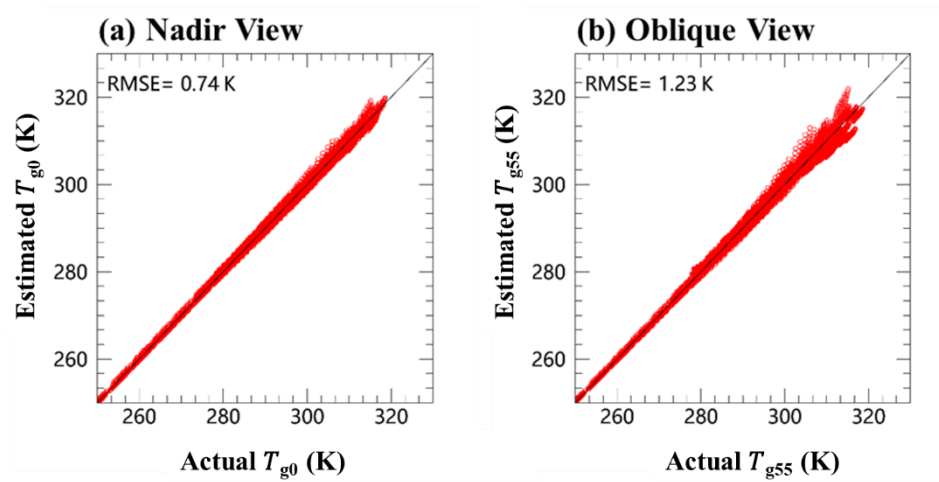


Fig 3.6 Scatter plots of actual and estimated surface brightness temperature at nadir view (a) and oblique view (b)

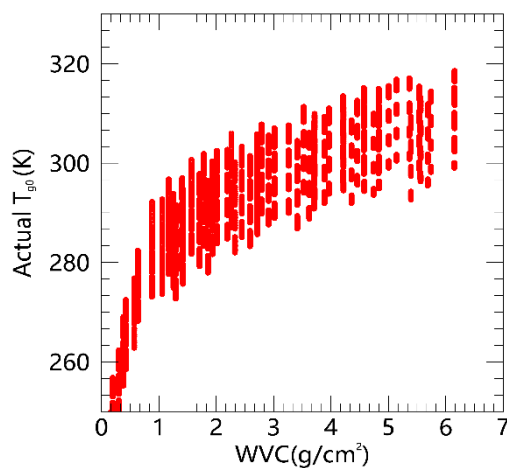


Fig 3.7 Scatter plots of WVC and actual surface brightness temperature.

Eq (3.15) can be used to express the angular effect of surface brightness temperature, neglecting retrieval model accuracy differences.

$$\Delta T_g = T_{g0} - T_{g55} \quad (3.15)$$

where  $T_{g0}$  is the surface brightness temperatures of SLSTR at nadir view, and  $T_{g55}$  is the surface brightness temperatures of SLSTR at oblique view.

### 3.4 Uncertainty evaluation in surface brightness temperature

According to the equation of the SW algorithm in Eq (3.16), the total uncertainty in surface brightness temperature is composed of contributions from the surface brightness temperature retrieval model and the TOA brightness temperature. The sources of uncertainty are assumed to be independent (Hulley et al., 2012a; Jiménez - Muñoz and Sobrino, 2006). The uncertainty can be expressed as shown in in Eq (3.16):

$$\delta(T_g) = \sqrt{\delta(sim)^2 + \delta(bt)^2} \quad (3.16)$$

where  $\delta(T_g)$  is the total uncertainty in surface brightness temperature;  $\delta(sim)$  is the uncertainty due to the retrieval algorithm;  $\delta(bt)$  is the uncertainty associated with TOA brightness temperature. These errors are calculated in the following two subsections.

#### 3.4.1 Uncertainty evaluation resulting from the retrieval model

$\delta(sim)$  is the algorithm fitting error based on the simulation database generated in Section 3.2. To calculate the surface brightness temperature uncertainty associated with the model uncertainty, it is assumed that there are no uncertainties in the input parameters, including atmospheric profile, TOA radiance. Only the uncertainty of the algorithm itself is considered. The retrieval model uncertainty is characterized by the RMSE between the surface brightness temperature retrieved by the SW algorithm and the surface brightness temperature used in the MODTRAN radiative transfer simulations. It can be written as Eq (3.17).

$$\delta(sim) = E \left[ (T_{ret} - T_{act})^2 \right]^{1/2} \quad (3.17)$$

where  $T_{ret}$  is the estimated surface brightness temperature;  $T_{act}$  is the actual surface brightness temperature;  $E[ ]$  is the arithmetic mean.  $\delta(sim)$  is 0.74 K at nadir view and 1.23 K at oblique view as shown in Fig 3.6.

### 3.4.2 Uncertainty evaluation resulting from noise in TOA brightness temperature

The uncertainty caused by TOA brightness temperature (including sensor noise and radiometric calibration) can be expressed as:

$$\delta(bt) = \sqrt{\left(\frac{\partial T_g}{\partial T_i} \delta(T_i)\right)^2 + \left(\frac{\partial T_g}{\partial T_j} \delta(T_j)\right)^2} \quad (3.18)$$

where  $\frac{\partial T_g}{\partial T_i}$  is the first-order partial derivative of the surface brightness temperature

with respect to TOA brightness temperature in channel  $i$ ;  $\delta(T_i)$  is NE $\Delta$ T in channel  $i$ ;

$\frac{\partial T_g}{\partial T_j}$  is the first-order partial derivative of the surface brightness temperature with

respect to TOA brightness temperature in channel  $j$ ;  $\delta(T_j)$  is NE $\Delta$ T in channel  $j$ . The

NE $\Delta$ T value for SLSTR at 10.85  $\mu$ m is 0.05 K, with a TOA brightness temperature of 270 K. The NE $\Delta$ T value for SLSTR at 12  $\mu$ m is also 0.05 K, same as the value at 10.85  $\mu$ m.

The first-order Taylor series expansion of the TOA brightness temperature can be applied to Eq. (3.14), as follows:

$$\frac{\partial T_g}{\partial T_i} = a_1 + a_2 + 2a_3T_i - 2a_3T_j \quad (3.19)$$

$$\frac{\partial T_g}{\partial T_j} = -a_2 - 2a_3T_i + 2a_3T_j \quad (3.20)$$

where  $a_1$ - $a_3$  are coefficients of split-window algorithm in Table 3.1.  $\frac{\partial T_g}{\partial T_i}$  of nadir and

oblique observations are 1.39 K and 1.13 K.  $\frac{\partial T_g}{\partial T_j}$  of nadir and oblique observations

are -0.37 K and -0.11 K.  $\delta(bt)$  is 1.44 K at nadir observations and 1.14 K at oblique

observations. The total uncertainty  $\delta(T_g)$  of nadir and oblique observations are 1.62 K and 1.68 K, respectively.

## 4. Angular effects of surface brightness temperatures observed from SLSTR data

Although the surface brightness temperature retrieval algorithm assumes isotropic thermal radiation from the surface, heterogeneous mixed pixels are widely present. Therefore, selecting pixels with uniform land cover types within the study area could reduce errors. This section first defines the study area by combining MOD12Q1 and SRTM data, considering the uniformity of land cover and elevation. Based on the selected study areas, the magnitude and characteristics of  $\Delta T_g$  across different land cover types were observed. The analysis explores the influence of season, latitude, solar zenith angle, and climate on the angular effects. Additionally, three modules of the GeoDetector method were applied to conduct a detailed analysis of the driving factors influencing the angular effects.

### 4.1 Study area

#### 4.1.1 Sites selection

To compare the nadir surface brightness temperature with the oblique surface brightness temperature obtained from SLSTR, it is necessary to select pixels with homogeneous land cover types and flat terrain at a 1 km scale. This study uses the MCD12Q1 land cover classification data to analyze the spatial homogeneity of land cover types in 2018. The MCD12Q1 dataset includes a total of 315 global images with a pixel resolution of 500 m. First, the global images are mosaicked into a single map based on the IGBP classification. Then, the pixels are aggregated into  $2 \times 2$  blocks. For each SLSTR pixel, it is considered homogeneous only if all MCD12Q1 pixels within the SLSTR pixel belong to the same class. Additionally, to minimize the influence of terrain factors, the SRTM data with a 90 m spatial resolution is used. The SRTM data is spatially aggregated to a resolution of 1 km to match the spatial resolution of the

SLSTR data. The standard deviation of surface elevation is calculated for each SLSTR pixel. The standard deviation of surface elevation should be less than 100 m.

In the aggregated image, a moving window size 3×3 is used to identify pixels with uniform classification. A pixel is considered to meet the criteria if all nine pixels within the window have the same land cover type.

To cover the diversity of global ecological and climate types, a total of 42 sites were distributed worldwide, ranging from the cold regions of the Northern Hemisphere to Antarctica.

### 4.1.2 The location of the study area

According to the criteria, forty-two sites over fourteen land covers were selected using the IGBP classification system (evergreen needleleaf forests (ENF), evergreen broadleaf forests (EBF), deciduous broadleaf forests (DBF), mixed forests (MF), open shrublands (OSH), woody savannas (WSA), savannas (SVA), grasslands (GRA), permanent wetlands (WET), croplands (CRO), urban and built-up lands (URB), cropland/natural vegetation mosaic (CVM), snow and ice (SNO), barren or sparsely vegetated (BSV)) shown in Fig 4.1. Detailed information of each study area was shown in Table 4.1.

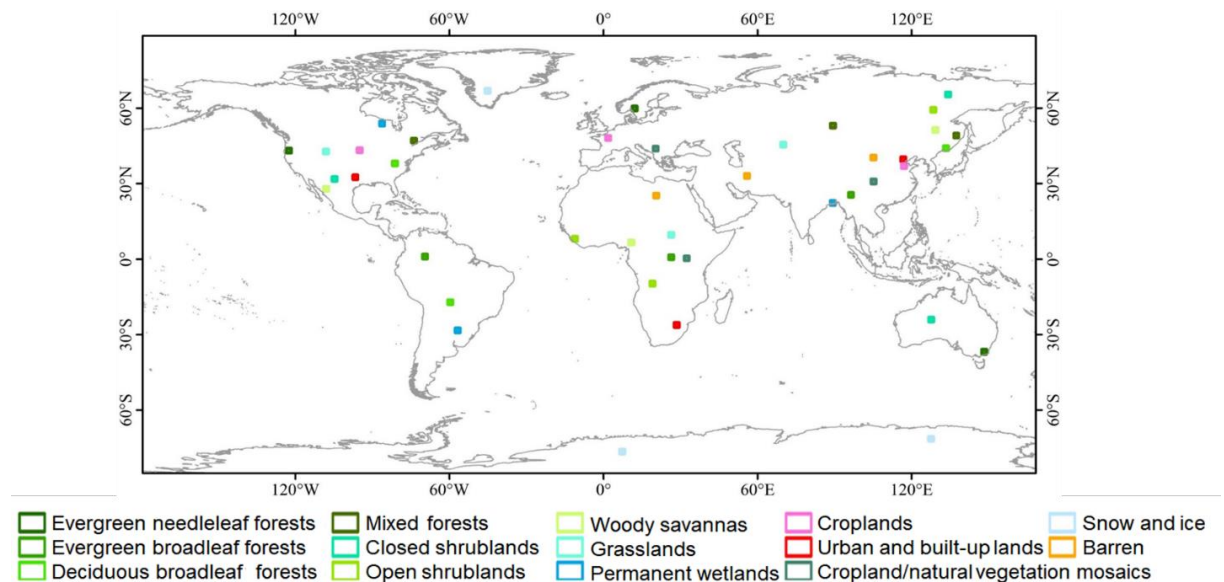


Fig 4.1 Geolocation of the selected 42 study sites.

Table 4.1 Detailed information of the selected 42 study sites.

IGBP_ID	Climate	Lat	Lon	IGBP_Class
1_1	Temperate	44.0	-123.4	Evergreen needleleaf forests
1_2	Cold	60.7	11.3	Evergreen needleleaf forests
1_3	Temperate	-36.0	147.4	Evergreen needleleaf forests
2_1	Temperate	26.40	95.53	Evergreen broadleaf forests
2_2	Tropical	1.6	25.4	Evergreen broadleaf forests
2_3	Tropical	1.86	-70.40	Evergreen broadleaf forests
4_1	Temperate	38.8	-82.0	Deciduous broadleaf forests
4_2	Tropical	-16.3	-60.5	Deciduous broadleaf forests
4_3	Cold	44.9	132.5	Deciduous broadleaf forests
5_1	Cold	48.75	136.42	Mixed forests
5_2	Cold	53.8	88.5	Mixed forests
5_3	Cold	48.0	-74.6	Mixed forests
7_1	Arid	32.7	-105.6	Open shrublands
7_2	Arid	-23.23	126.87	Open shrublands
7_3	Cold	66.2	133.3	Open shrublands
8_1	Cold	60.1	127.6	Woody savannas
8_2	Tropical	-8.8	18.1	Woody savannas
8_3	Tropical	8.9	-12.0	Woody savannas
9_1	Arid	28.8	-108.9	Savannas
9_2	Tropical	7.4	9.9	Savannas
9_3	Cold	52.2	128.4	Savannas
10_1	Arid	43.6	-108.9	Grasslands
10_2	Arid	10.5	25.5	Grasslands
10_3	Arid	46.36	69.16	Grasslands
11_1	Tropical	23.2	88.4	Permanent wetlands
11_2	Temperate	-27.47	-57.56	Permanent wetlands
11_3	Cold	54.8	-87.1	Permanent wetlands
12_1	Cold	44.1	-95.9	Croplands
12_2	Temperate	49	1	Croplands
12_3	Cold	37.8	116.2	Croplands
13_1	Temperate	-25.34	27.66	Urban and built-up lands
13_2	Cold	40.5	115.9	Urban and built-up lands
13_3	Temperate	33.42	-97.5	Urban and built-up lands

14_1	Tropical	1.2	31.5	Cropland/natural vegetation mosaics
14_2	Temperate	31.7	104.3	Cropland/natural vegetation mosaics
14_3	Temperate	44.7	19.4	Cropland/natural vegetation mosaics
15_1	Polar	67.7	-45.9	Snow and ice
15_2	Polar	-75.7	6.4	Snow and ice
15_3	Polar	-70.5	126.7	Snow and ice
16_1	Arid	26.1	19.7	Barren
16_2	Arid	33.9	55.1	Barren
16_3	Arid	41.2	104.32	Barren

After obtaining the differences in surface brightness temperature across various study areas using the split-window algorithm in Chapter 3, it is necessary to further remove outliers by applying the mean plus or minus three times the standard deviation. If the number of processed pixels in a selected study area is less than 1%, the entire scene will be excluded from further analysis. The remaining data consists of 1,910 and 2,996 scenes at daytime and nighttime, respectively. The monthly distribution of these scenes is shown in Fig 4.2. Detailed information on the available data for each station is provided in Table 4.2, including the number of scenes and pixels during day and night.

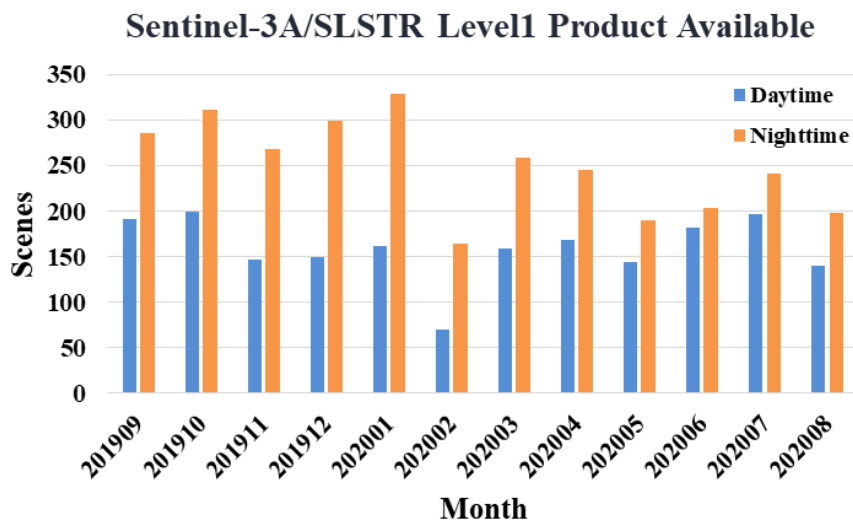


Fig 4.2 Total available scenes of SLSTR Level1 data for each month.

Table 4.2 Information of available SLSTR Level1 data of the selected 42 study sites.

IGBP_ID	Number	Number	Number	Number	IGBP_ID	Number	Number	Number	Number
	of	of	of	of		of	of	of	of
	scenes	points	scenes	points		scenes	points	scenes	points
	Daytime		Nighttime			Daytime		Nighttime	
1_1	53	39782	61	49629	10_1	57	35287	76	50223
1_2	60	45264	112	73190	10_2	37	35318	26	23680
1_3	66	61363	81	63834	10_3	65	77140	114	94949
2_1	56	49170	74	45186	11_1	41	19568	50	28123
2_2	17	14733	27	26171	11_2	56	76258	55	42154
2_3	17	4974	19	11574	11_3	37	28807	109	70831
4_1	54	41147	82	64088	12_1	55	51423	99	86241
4_2	39	39634	54	45117	12_2	74	46026	99	72458
4_3	55	35385	90	56170	12_3	66	68892	96	75197
5_1	84	50250	108	74962	13_1	81	71389	81	69997
5_2	60	28162	93	44667	13_2	38	21968	97	74998
5_3	31	13017	65	37277	13_3	43	36930	90	61567
7_1	73	64698	70	51422	14_1	14	4173	21	9124
7_2	25	31654	60	47734	14_2	24	15482	36	20468
7_3	79	44283	148	83834	14_3	85	75225	102	74985
8_1	37	25732	129	73008	15_1	24	16115	83	72159
8_2	8	6561	18	10751	15_2	1	103	73	26491
8_3	3	2755	8	6464	15_3	1	391	41	34995
9_1	23	16105	30	23743	16_1	93	133278	82	70386
9_2	21	12900	25	18695	16_2	82	63732	93	82293
9_3	17	14324	34	20517	16_3	58	60401	85	61028

## 4.2 Results of angular effects of surface brightness temperature

This section presents the magnitude of surface brightness temperature differences  $\Delta T_g$  across fourteen land cover types to verify the presence of angular effects. Additionally, the variations in surface brightness temperature differences are analyzed, across four different seasons, solar zenith angles, six latitude zones, and five climate types.

### 4.2.1 Land cover types

Fig 4.3 to Fig 4.16 shows the  $\Delta T_g$  of fourteen land cover types during the daytime. Each figure (a) represents the geographical location of the three sites corresponding to the land cover type. Figures (b-c) use the violin plot to show the  $\Delta T_g$  of each site from September 2019 to August 2020 monthly. The violins present the distribution of the  $\Delta T_g$  with density curves. The upper and lower sides of the black rectangle present the third quartile and first quartile, respectively. The black horizontal line in rectangle indicates the median. The red dotted line represents the mean. The upper and lower boundaries are the maximum and minimum values, respectively. For daytime,  $\Delta T_g$  is primarily concentrated between -2 K and 8 K both in the northern and southern hemisphere, with a small amount of data up to 9 K or falling below -2 K. Therefore, in the following analysis we mainly focus on the distribution of the mean  $\Delta T_g$ .

#### Daytime

For ENF, sites 1-1 and 1-2 are both located in the northern hemisphere. According to the probability distribution observed in Fig 4.3 (b-c), sites 1-1 and 1-2 exhibit similar distribution characteristics, but  $\Delta T_g$  at site 1-1 is slightly higher than at site 1-2 in most months, except for July and August. This difference may be attributed to the higher latitude of site 1-2, which receives less solar radiation. In July and August, site 1-1 has only 1 and 3 days of available data, respectively, compared to 8 days for site 1-2 in both months. As a result, the data volume at site 1-1 is smaller, and its  $\Delta T_g$  range is narrower than that of site 1-2. The mean  $\Delta T_g$  throughout the year ranges from -1 K to 4 K. Site 1-3 is located in the southern hemisphere (Fig 4.3 (d)), where the mean  $\Delta T_g$  at site 1-3 ranges from 1 K to 4 K throughout the year, which is higher than that of the two Northern Hemisphere sites, indicating a trend of decreasing with increasing latitude.

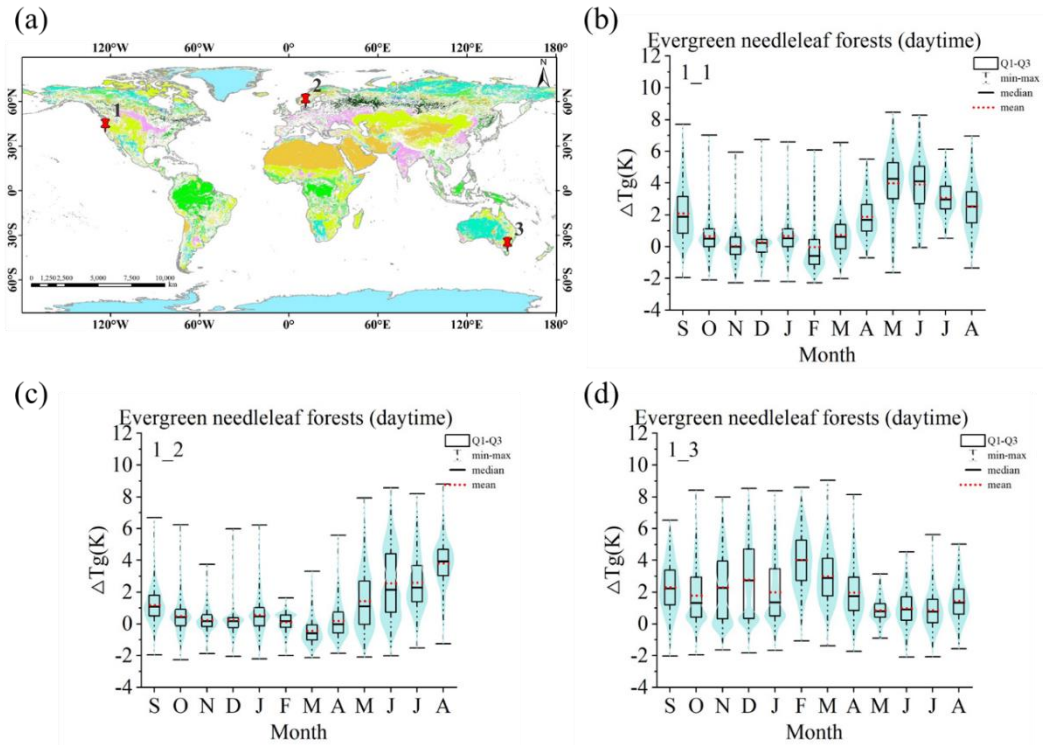


Fig 4.3 (a) Geographic distribution of the study sites. (b-d) Violin plots of the  $\Delta T_g$  in evergreen needleleaf forests (ENF) during the day from September 2019 to August 2020. The violins present the distribution of the  $\Delta T_g$  with density curves. The upper and lower sides of the black rectangle present the third quartile and first quartile, respectively. The black horizontal line in rectangle indicates the median. The red dotted line represents the mean. The upper and lower boundaries are the maximum and minimum values, respectively.

For EBF, sites 2-1, 2-2, and 2-3 are all located in the northern hemisphere. The mean  $\Delta T_g$  at site 2-1 ranges from 0 to 6 K and increases with rising temperatures in Fig 4.4 (b). The mean  $\Delta T_g$  in November is larger than in October and December. It is primarily due to the TOA brightness temperature in November is larger on average. Additionally, sites 2-2 and 2-3 are situated in tropical rainforest regions near the equator, where abundant rainfall and prolonged cloud cover make it difficult to obtain a large amount of data. Due to significant variations in TOA brightness temperature on different days within the same month, ranging from 5 to 7 K, the mean  $\Delta T_g$  at site 2-2 in December and February is distributed across multiple temperature intervals.

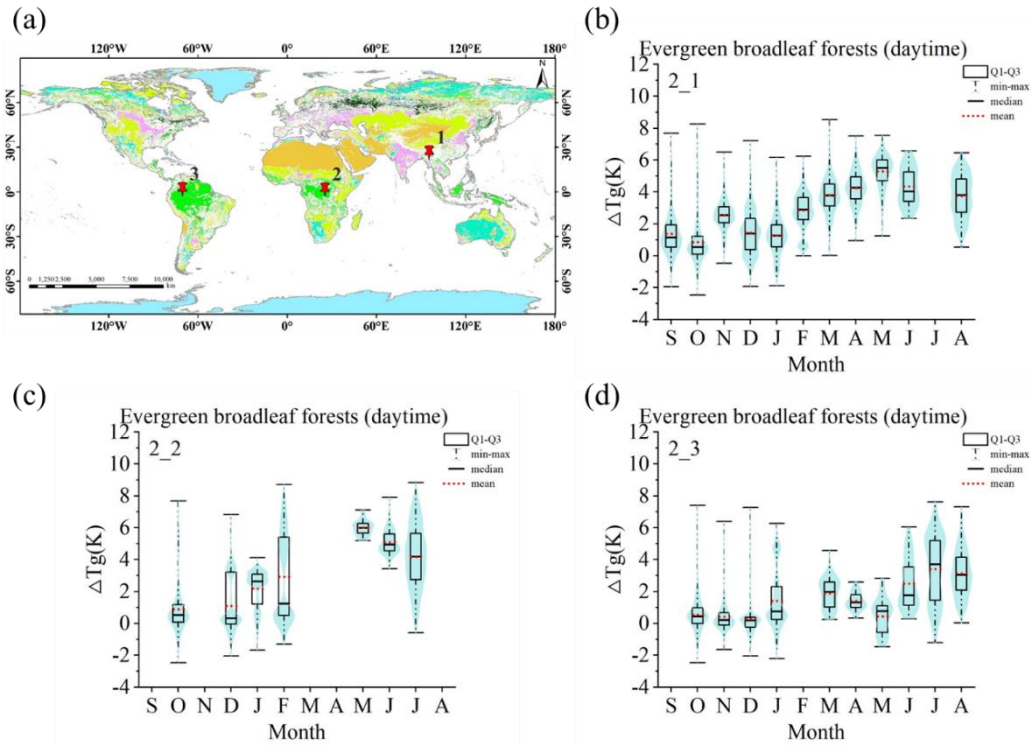


Fig 4.4 (a) Geographic distribution of the study sites. (b-d) Violin plots of the  $\Delta T_g$  in evergreen broadleaf forests (EBF) during the day from September 2019 to August 2020.

The mean  $\Delta T_g$  for DBF ranges from -1 to 6 K in Fig 4.5 (b-c). Site 4-2 is located in a tropical region of the southern hemisphere, where the dry season typically occurs from April to September, and the rainy season occurs during the remaining months. During periods of heavy rainfall, air humidity is higher, leading to a larger increase in surface brightness temperature observed at an oblique angle compared to that observed vertically. As a result, the mean  $\Delta T_g$  is lower during the rainy season and higher during the dry season.

The mean  $\Delta T_g$  for MF shows a similar pattern over time and temperature changes as that of ENF, EBF, and DBF forest types in Fig 4.6 (b-c). In months with lower temperatures, the mean  $\Delta T_g$  is also lower, and as temperatures rise, the mean  $\Delta T_g$  increases accordingly. For MF, as shown in Fig 4.6(a), the three MF sites are located at similar latitudes but are spread across different longitudes. The mean  $\Delta T_g$  for MF ranges from -1 to 5 K, with no significant differences in distribution across the various longitudes.

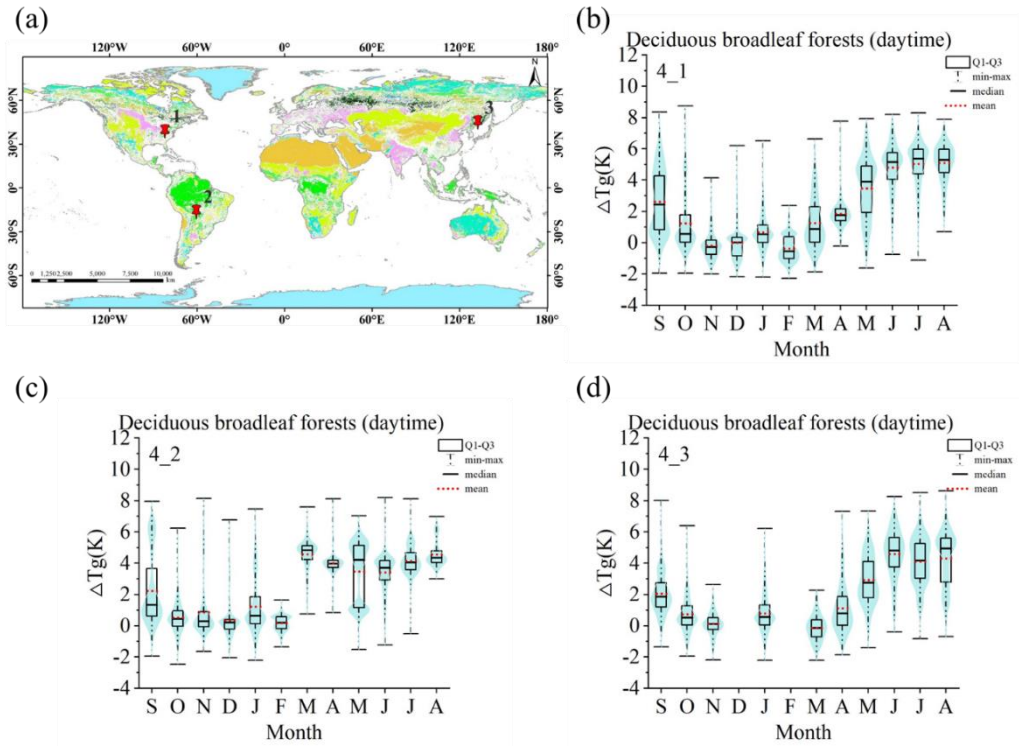


Fig 4.5 (a) Geographic distribution of the study sites. (b-d) Violin plots of the  $\Delta T_g$  in deciduous broadleaf forests (DBF) during the day from September 2019 to August 2020.

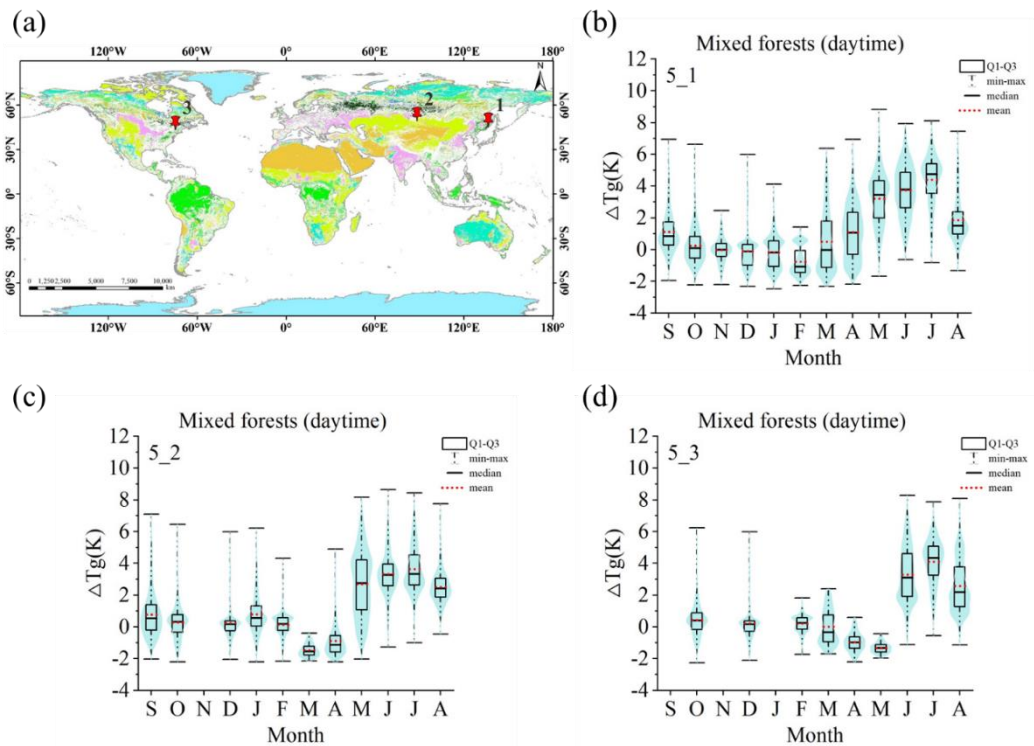


Fig 4.6 (a) Geographic distribution of the study sites. (b-d) Violin plots of the  $\Delta T_g$  in mixed forests (MF) during the day from September 2019 to August 2020.

For OSH, Sites 7-1 and 7-3 (Fig 4.7 (b) and (d)), located in the northern hemisphere, share a common pattern in mean  $\Delta T_g$ , with values ranging from 0 to 1 K between October and March, and increasing from April to September. However, the mean  $\Delta T_g$  at Site 7-1 is concentrated between 4 and 6 K from April to September, while at site 7-3, it is around 2 K, indicating a smaller angular effect at higher latitudes. Site 7-2, located in the southern hemisphere, shows an opposite trend compared to the northern hemisphere sites in Fig 4.7 (c). Its mean  $\Delta T_g$  ranges from 1 to 3 K during cooler months, while no data is available for the warmest period from December to February, during which the mean  $\Delta T_g$  reach 5 to 7 K.

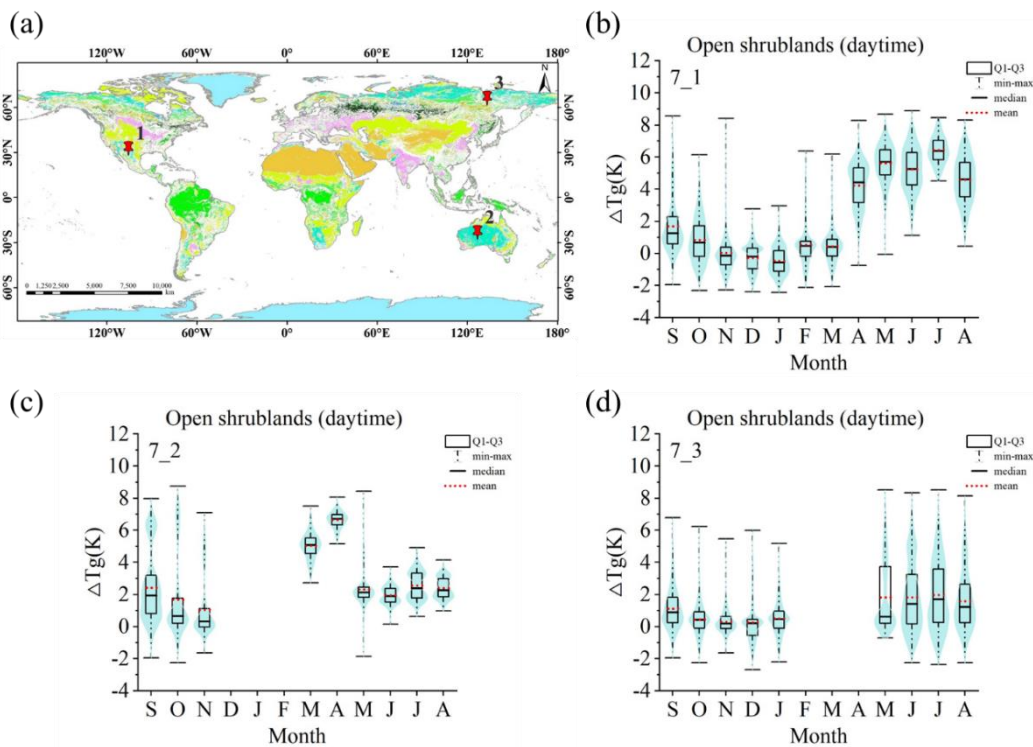


Fig 4.7 (a) Geographic distribution of the study sites. (b-d) Violin plots of the  $\Delta T_g$  in open shrublands (OSH) during the day from September 2019 to August 2020.

Site 8-1 (Fig 4.8 (b)) of WSA is located in a high-latitude region of the northern hemisphere, where snow cover results in a lack of valid data from December to April. The mean  $\Delta T_g$  at this site ranges from 0 to 3 K. At site 8-2 in Fig 4.8 (c), the rainy season occurs from October to April each year, during which almost no data is available. During the dry season, the mean  $\Delta T_g$  ranges from 3 to 5 K. Site 8-3 (Fig 4.8 (c)) is situated in the southern hemisphere at a latitude similar to that of site 8-2, and experiences similar data gaps for the same reasons. During the dry season, the mean

$\Delta T_g$  at site 8-3 ranges from 4 to 7 K, which is higher than that observed in the northern hemisphere.

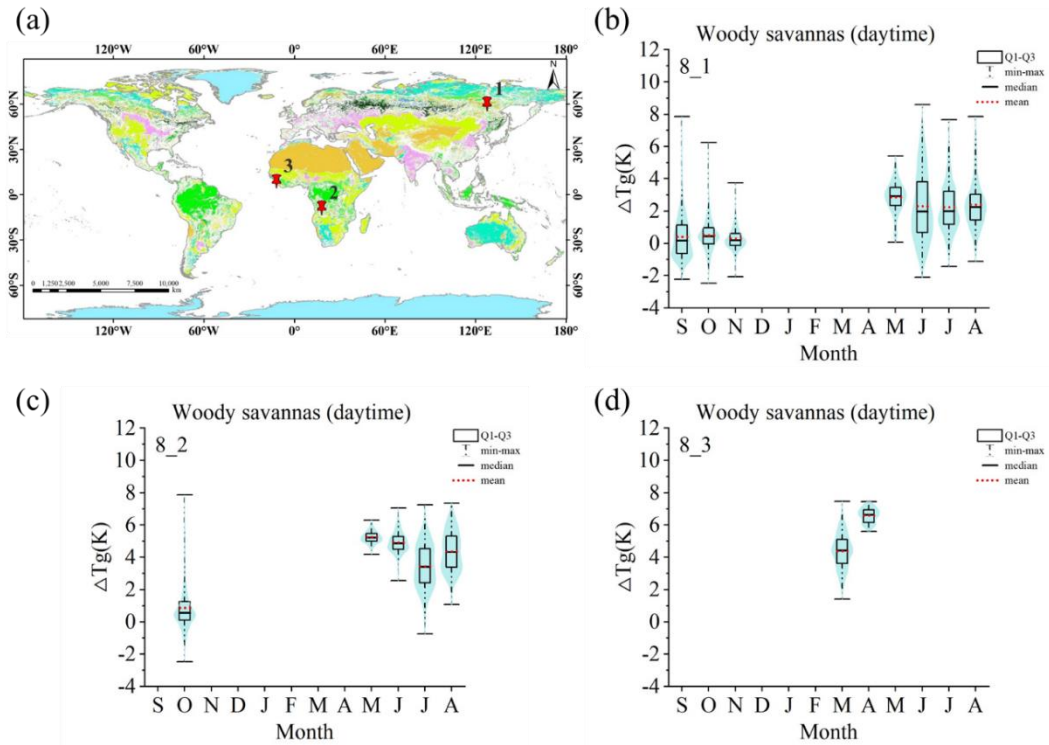


Fig 4.8 (a) Geographic distribution of the study sites. (b-d) Violin plots of the  $\Delta T_g$  in woody savannas (WSA) during the day from September 2019 to August 2020.

SVA includes three sites in the northern hemisphere in Fig 4.9 (b-d). Sites 9-1 and 9-3 exhibit similar distribution characteristics; however, the mean  $\Delta T_g$  at site 9-1 ranges from 0 to 7 K, which is 2 K higher than that at site 9-3, located at a higher latitude. Site 9-2 has data gaps due to the influence of dry and wet seasons. The mean  $\Delta T_g$  values for SVA are similar to those of WSA.

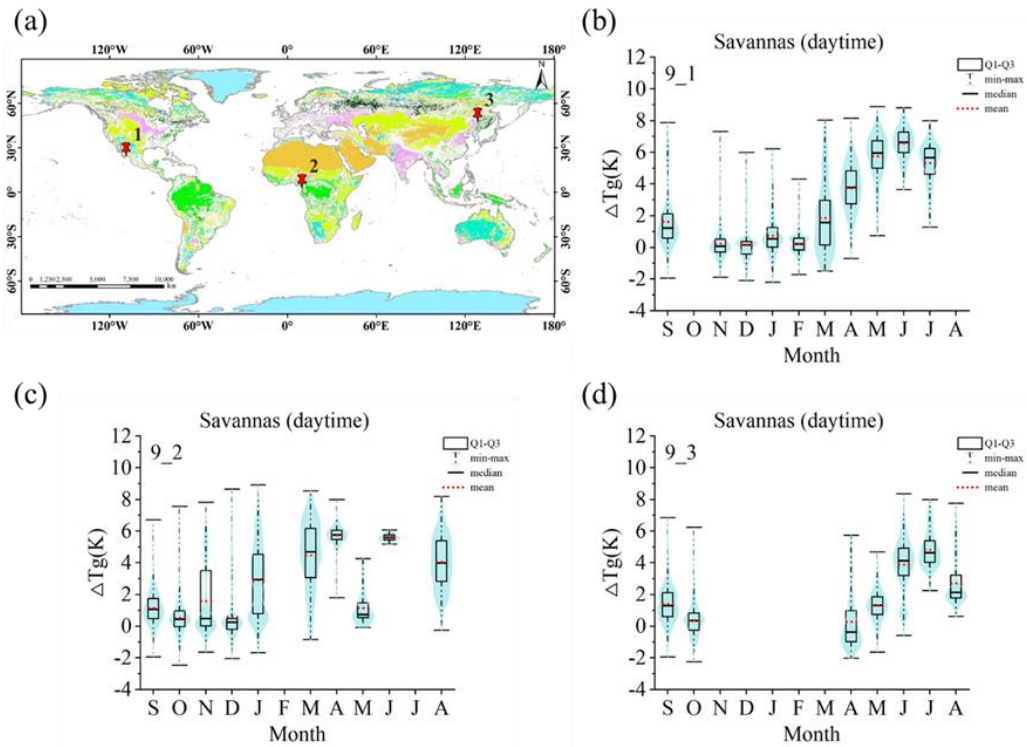


Fig 4.9 (a) Geographic distribution of the study sites. (b-d) Violin plots of the  $\Delta T_g$  in savannas (SVA) during the day from September 2019 to August 2020.

The sites of GRA are all located in the northern hemisphere. Sites 10-1 (Fig 4.10 (b)) and 10-3 (Fig 4.10 (d)) are situated at similar latitudes but are spread across different longitudes. The mean  $\Delta T_g$  at these sites ranges from -1 to 6 K. There is no significant difference in the overall distribution across different longitudes, which is consistent with the earlier findings for MF. At site 10-2, except for October, the mean  $\Delta T_g$  ranges from 3 to 7 K. The increase in the proportion of bare soil during the non-growing season amplifies the angular effect.

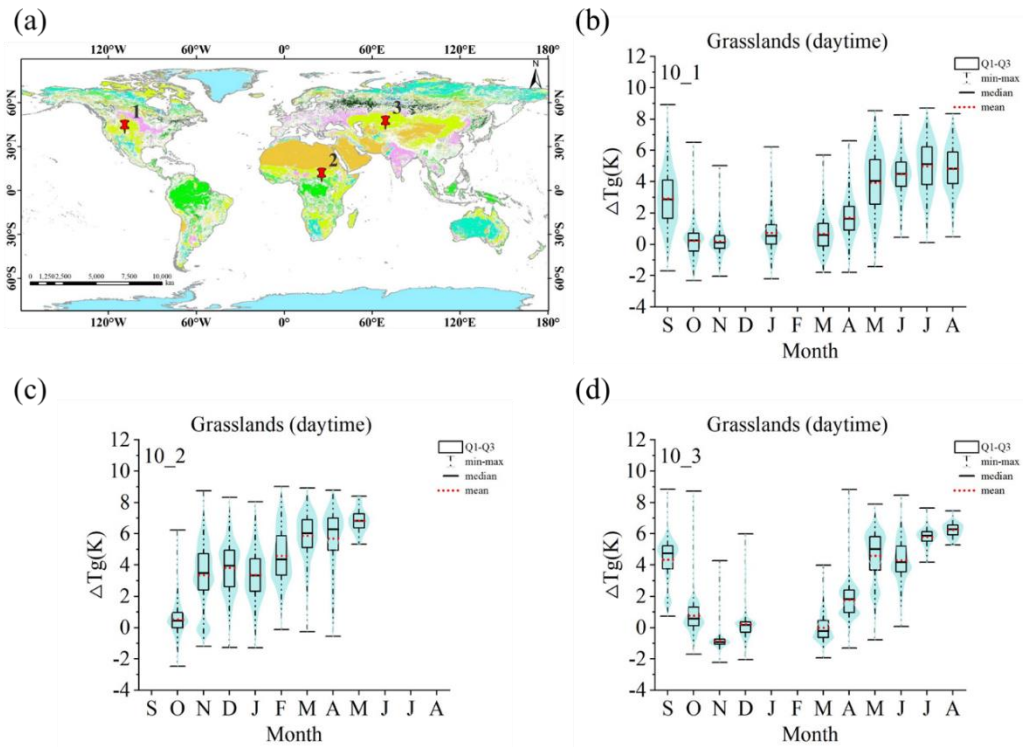


Fig 4.10 (a) Geographic distribution of the study sites. (b-d) Violin plots of the  $\Delta T_g$  in grasslands (GRA) during the day from September 2019 to August 2020.

For WET, sites 11-1 and 11-3 in the northern hemisphere exhibit similar distribution patterns in Fig 4.11(b) and (d). The mean  $\Delta T_g$  at site 11-1 ranges from 0 to 6 K, which is higher than that at site 11-3, where the mean  $\Delta T_g$  ranges from 0 to 4 K. This is consistent with the spatial characteristics observed in OSH and SVH. In the southern hemisphere, the mean  $\Delta T_g$  at site 11-2 (Fig 4.11(c)) ranges from 0 to 5 K, with higher values observed during the growing season. In January, the TOA brightness temperature shows significant variation over the five available days, reaching up to 15 K, resulting in a large difference in mean  $\Delta T_g$  compared to adjacent months.

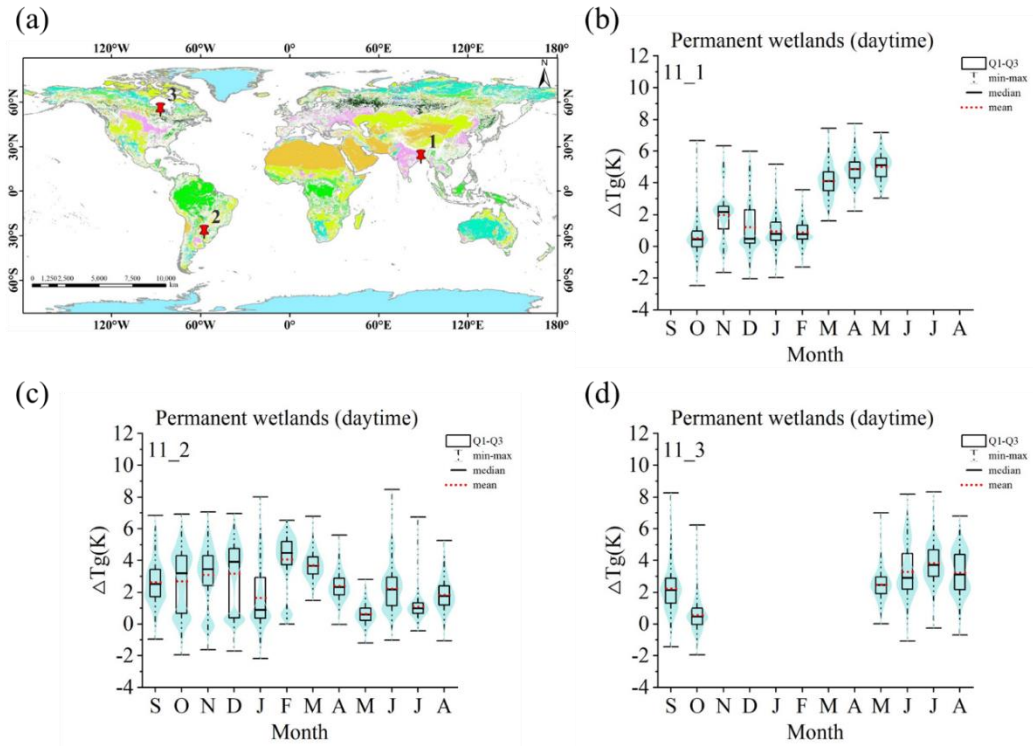


Fig 4.11 (a) Geographic distribution of the study sites. (b-d) Violin plots of the  $\Delta T_g$  in permanent wetlands (WET) during the day from September 2019 to August 2020.

The sites for CRO and CVM in Fig 4.12 and 4.14 are both located in the northern hemisphere, and their mean  $\Delta T_g$  values tend to increase with the growing season. The mean  $\Delta T_g$  ranges from -1 to 6 K. Although the angular effect is relatively pronounced, there are no significant differences in mean  $\Delta T_g$  across sites when comparing variations in longitude and latitude.

For URB, site 13-1 is located in the Southern Hemisphere, where the mean  $\Delta T_g$  ranges from 1 to 6 K throughout the year. Sites 13-2 and 13-3 are situated in the Northern Hemisphere. Between April and August, the mean  $\Delta T_g$  at these sites increases rapidly, influenced by both the growth of vegetation and the complex three-dimensional structure of urban areas, and further influences the directionality of surface thermal radiation.

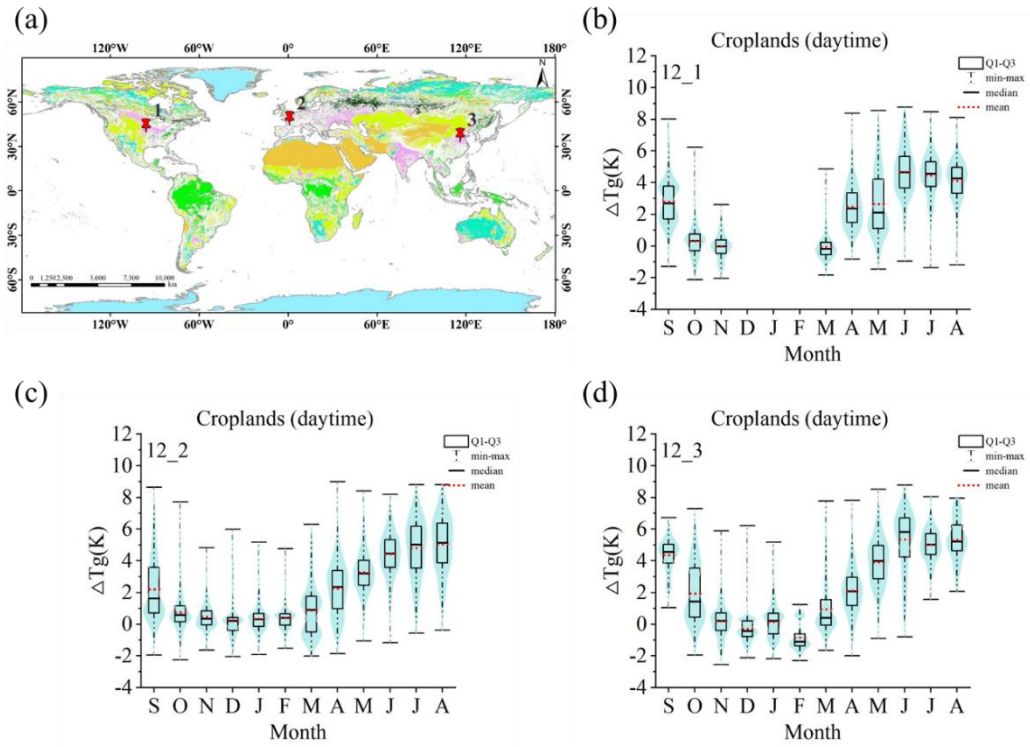


Fig 4.12 (a) Geographic distribution of the study sites. (b-d) Violin plots of the  $\Delta T_g$  in croplands (CRO) during the day from September 2019 to August 2020.

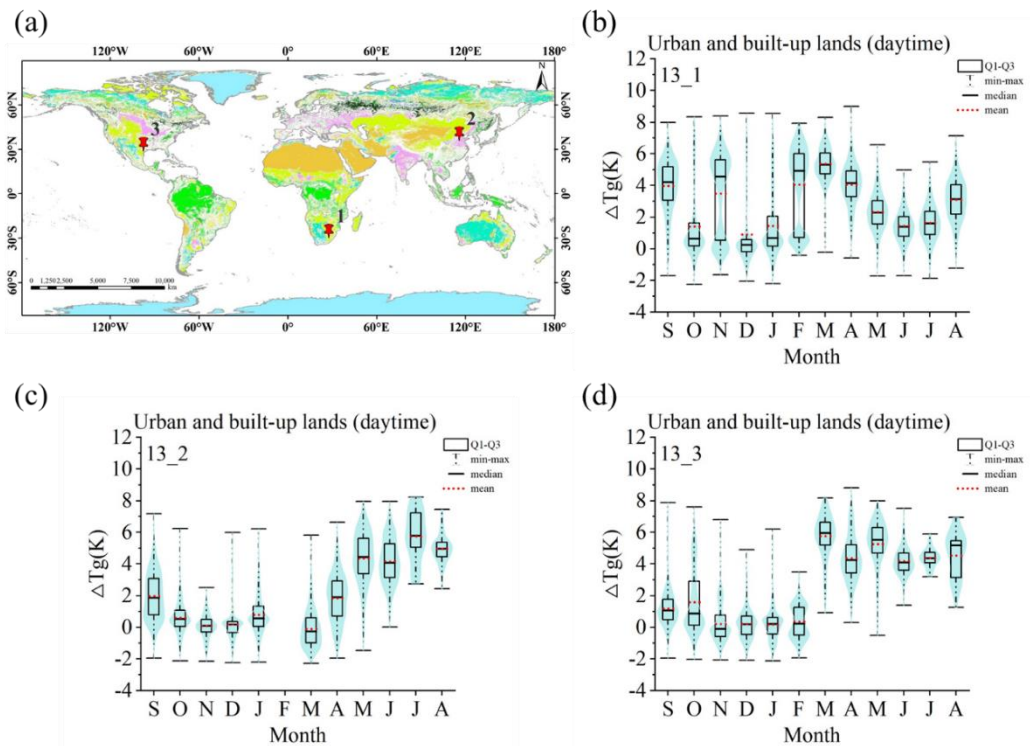


Fig 4.13 (a) Geographic distribution of the study sites. (b-d) Violin plots of the  $\Delta T_g$  in urban and built-up lands (URB) during the day from September 2019 to August 2020.

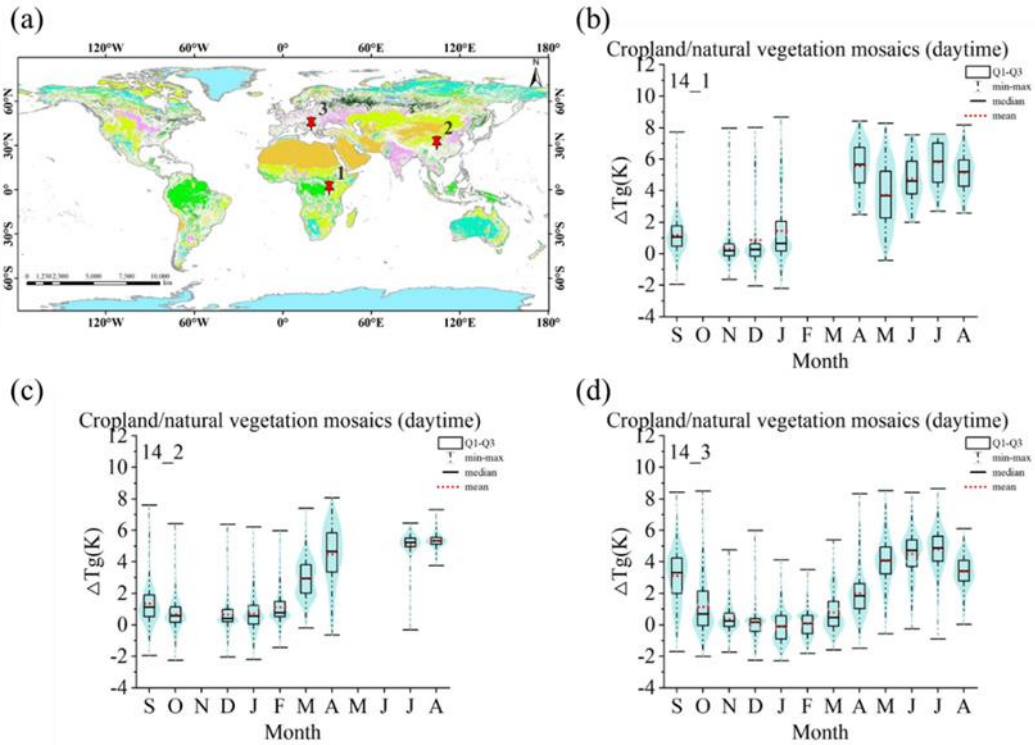


Fig 4.14 (a) Geographic distribution of the study sites. (b-d) Violin plots of the  $\Delta T_g$  in cropland/natural vegetation mosaics (CVM) during the day from September 2019 to August 2020.

All the SNO sites are located in polar regions, with two in Antarctic and one in Arctic in Fig 4.15. The completeness of data is quite poor for SNO sites. There is only one month of valid data for sites 15-2 and 15-3. For site 15-1, the number of valid data is eight months. The mean  $\Delta T_g$  of SNO sites is approximately 0 K in most months. Temporal variation of  $\Delta T_g$  is also negligible.

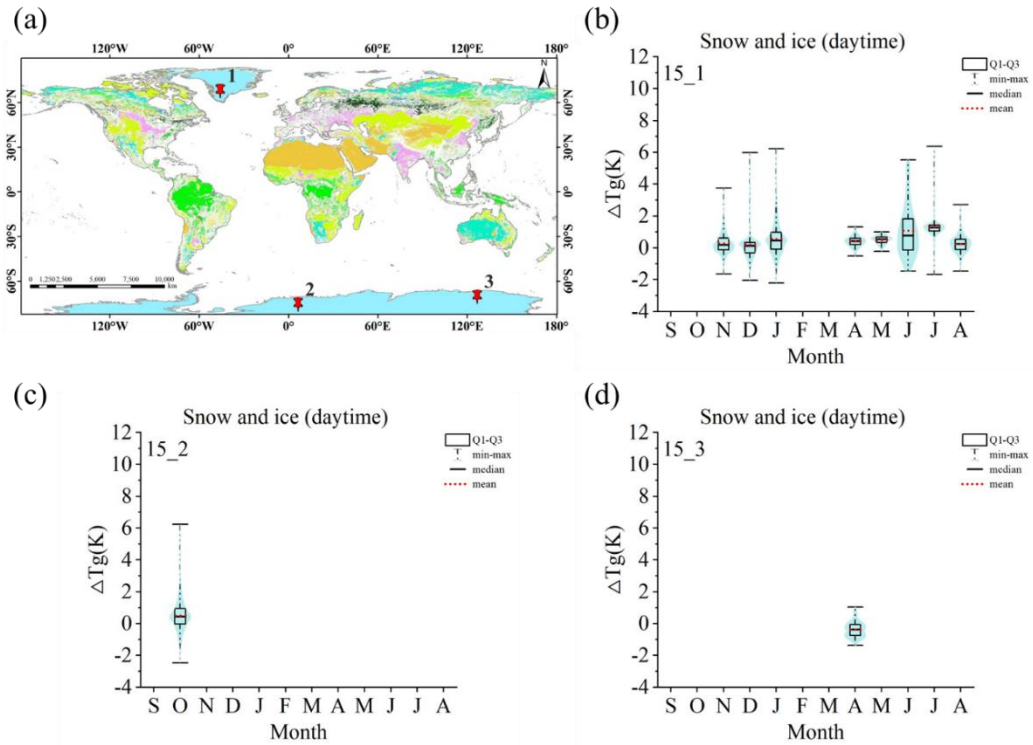


Fig 4.15 (a) Geographic distribution of the study sites. (b-d) Violin plots of the  $\Delta T_g$  in snow and ice (SNO) during the day from September 2019 to August 2020.

Three BSV sites are located in the northern hemisphere. Sites 16-1, 16-2 and 16-3 are characterized by significant annual fluctuation of  $\Delta T_g$ . The maximal value of the mean  $\Delta T_g$  can reach 6 K in August and the minimal value of  $\Delta T_g$  is lower than 0 K in December. The mean  $\Delta T_g$  increase at site 16-2 from March to July was larger than that at the other two stations, and the NDVI was also higher.

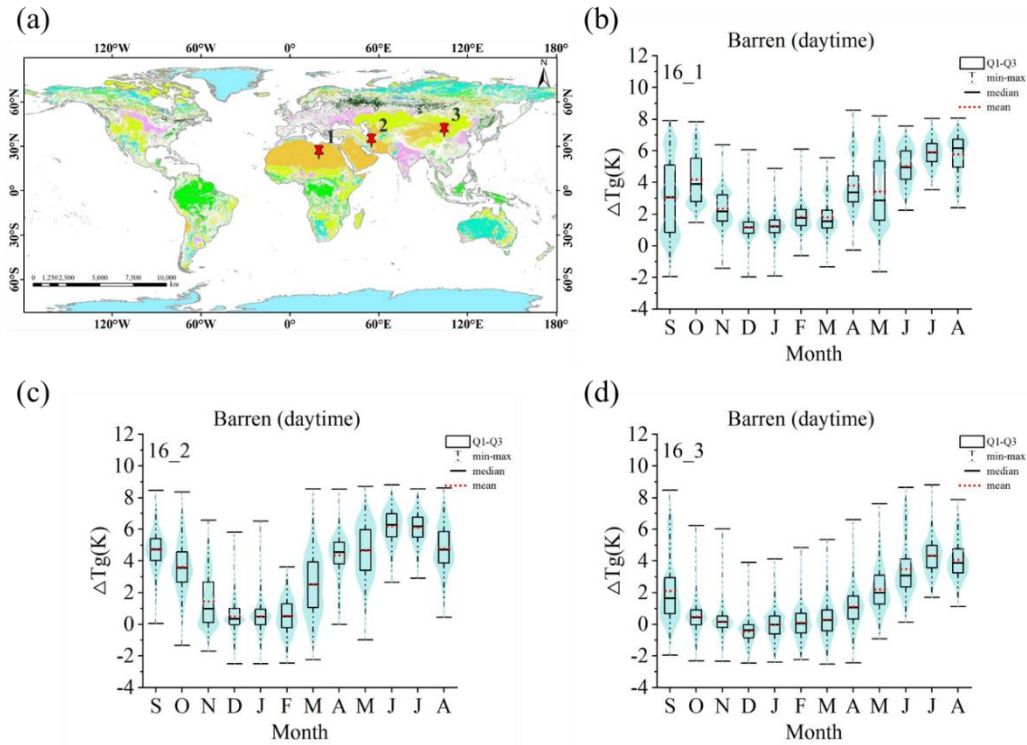


Fig 4.16 (a) Geographic distribution of the study sites. (b-d) Violin plots of the  $\Delta T_g$  in barren or sparsely vegetated (BSV) during the day from September 2019 to August 2020.

### Nighttime

Geographic distribution of study sites and violin plots of  $\Delta T_g$  of ENF, EBF, DBF, MF sites during nighttime are shown in Fig 4.17-4.20. The mean  $\Delta T_g$  of the three ENF sites are stable during the study period, with mean value ranging from approximately 0 K to 2 K. The temporal variation of the mean  $\Delta T_g$  during nighttime is minimal comparing with that during daytime. The fluctuation of the mean  $\Delta T_g$  of EBF sites during study period is distinctive and even higher than that during daytime. There is a sudden rise of the mean  $\Delta T_g$  in February or March to approximately 5 K in site 2-2 and 2-3, which are locating in equatorial regions. For DBF sites, the temporal fluctuations are moderate. Site 4-2 shows an abnormal rise of the mean  $\Delta T_g$  in October, February and May. The violin plot reveals that the dispersion of points is high and dual-spindle shaped in these months, which might be the reason of the sudden rise of the mean  $\Delta T_g$ . The dual-spindle shaped abnormality of the mean  $\Delta T_g$  can also be found in September for site 4-2 during daytime as shown in Fig 4.5. The mean  $\Delta T_g$  of MF sites are stable in the whole year except for site 5-1, which has a temperate rise in summer seasons.

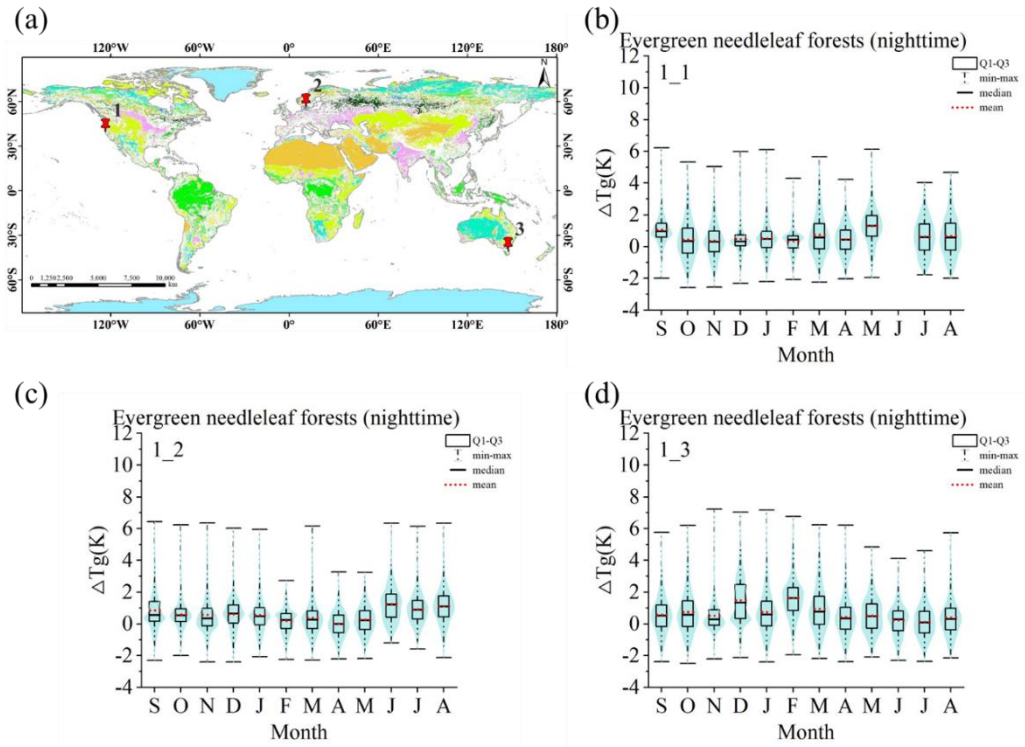


Fig 4.17 (a) Geographic distribution of the study sites. (b-d) Violin plots of the  $\Delta T_g$  in evergreen needleleaf forests (ENF) during the night from September 2019 to August 2020.

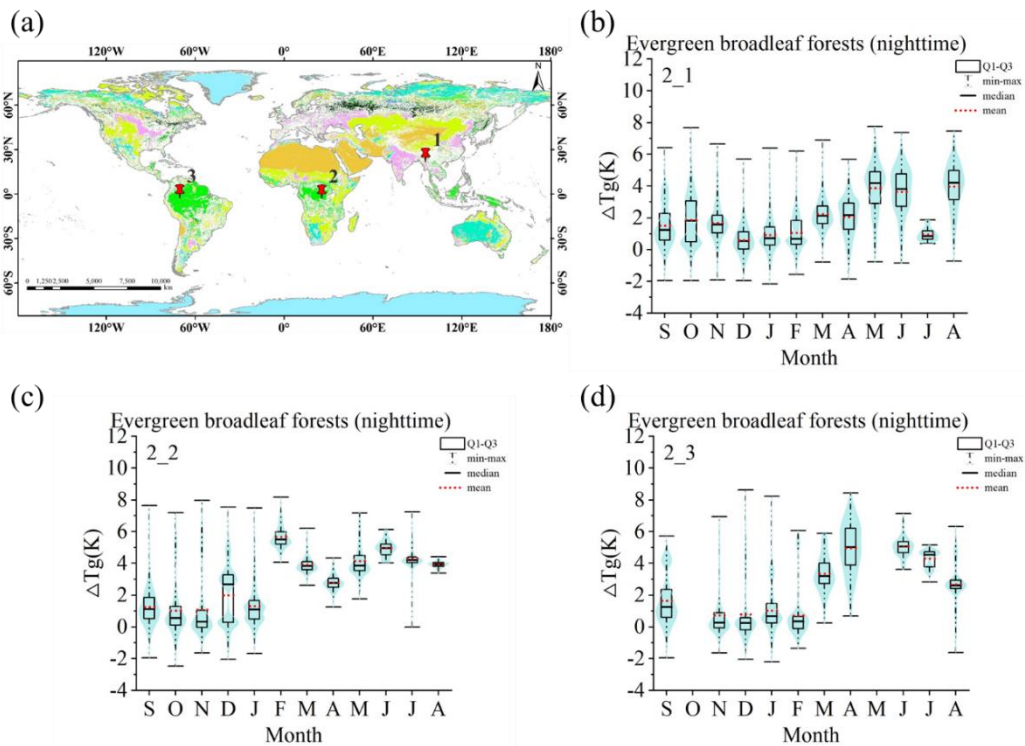


Fig 4.18 (a) Geographic distribution of the study sites. (b-d) Violin plots of the  $\Delta T_g$  in evergreen broadleaf forests (EBF) during the night from September 2019 to August 2020.

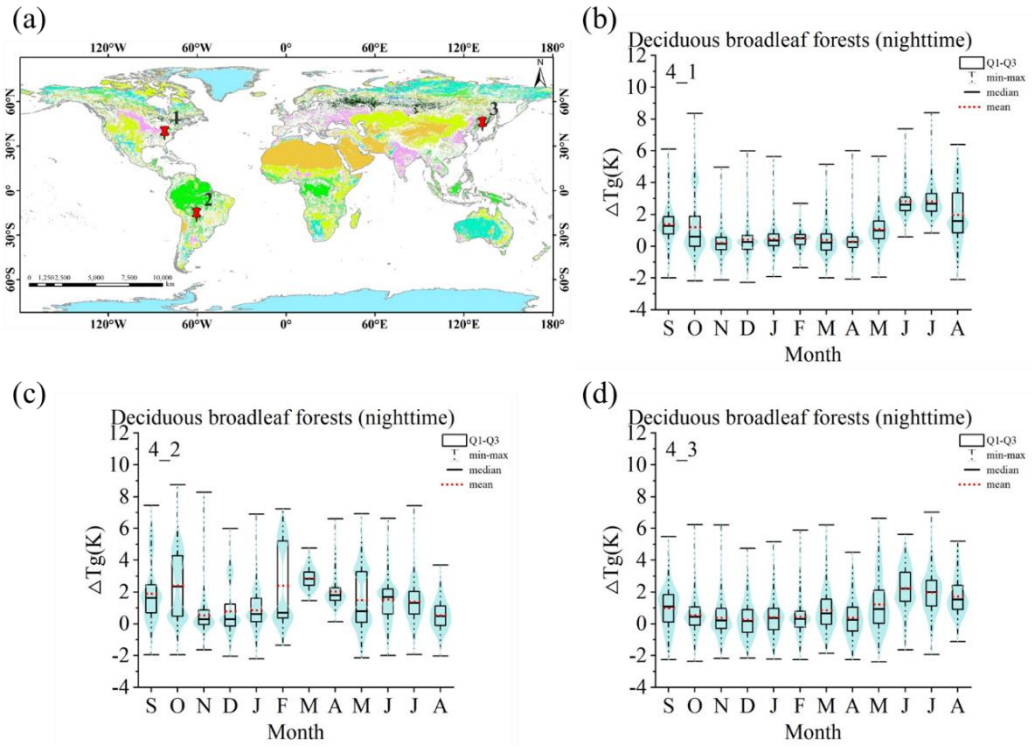


Fig 4.19 (a) Geographic distribution of the study sites. (b-d) Violin plots of the  $\Delta T_g$  in deciduous broadleaf forests (DBF) during the night from September 2019 to August 2020.

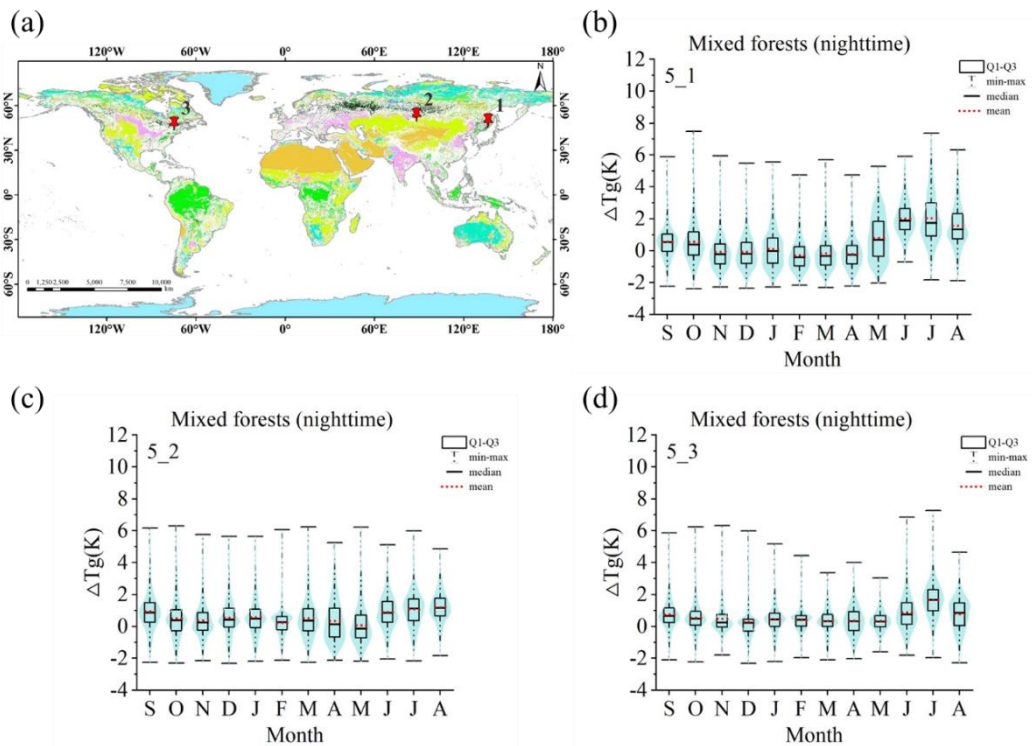


Fig 4.20 (a) Geographic distribution of the study sites. (b-d) Violin plots of the  $\Delta T_g$  in mixed forests (MF) during the night from September 2019 to August 2020.

Results for OSH, WSA, SVA and GRA during nighttime are given in Fig 4.21-4.24. The integrity of data is higher during nighttime than daytime for OSH sites. Data in June and July are missing for site 7-3, probably because these months are in the summer light-nights period. Temporal fluctuation for site 7-2 is evident in December to April, during which is the summer season for this site. For WSA sites, site 8-1 presents quite stable pattern in the whole year while site 8-2 and 8-3 are troubled by data incompleteness. Based on the residual data, the mean  $\Delta T_g$  of the two sites have significant temporal fluctuations. As for SVA sites, site 9-2, which locates in low latitude region, has stronger fluctuation than other two sites, which locates in middle- or high-latitude regions. As shown in Fig 4.24, fluctuation of the mean  $\Delta T_g$  of typical grassland sites is not significant but can still be identified by the rise of the mean  $\Delta T_g$  in summer season.

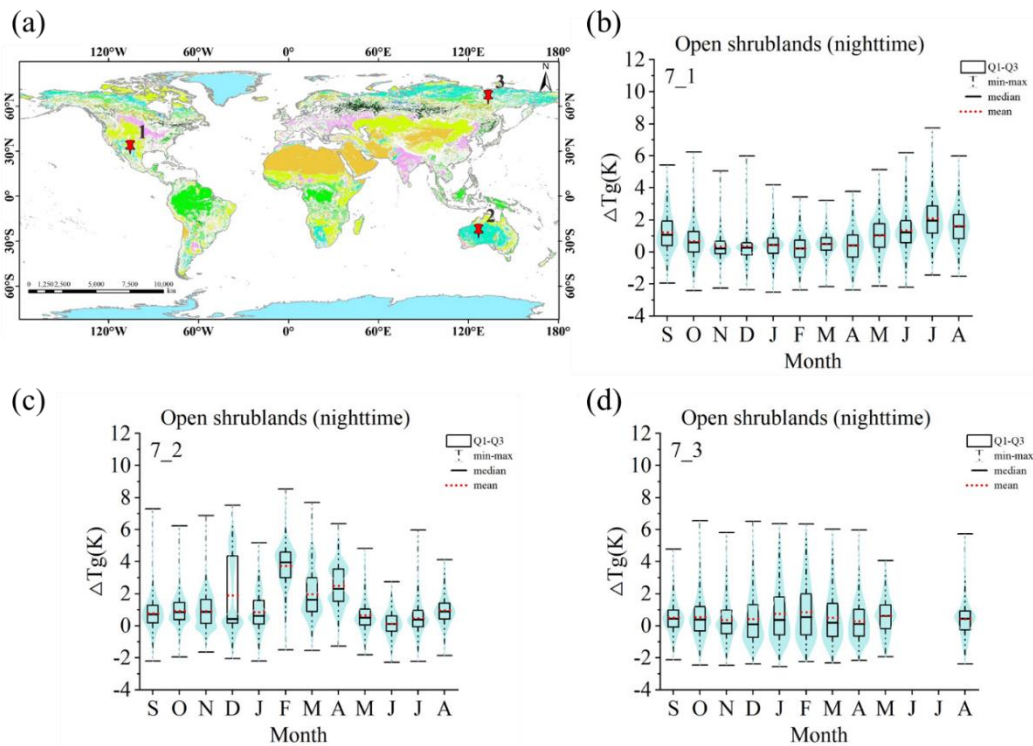


Fig 4.21 (a) Geographic distribution of the study sites. (b-d) Violin plots of the  $\Delta T_g$  in open shrublands (OSH) during the night from September 2019 to August 2020.

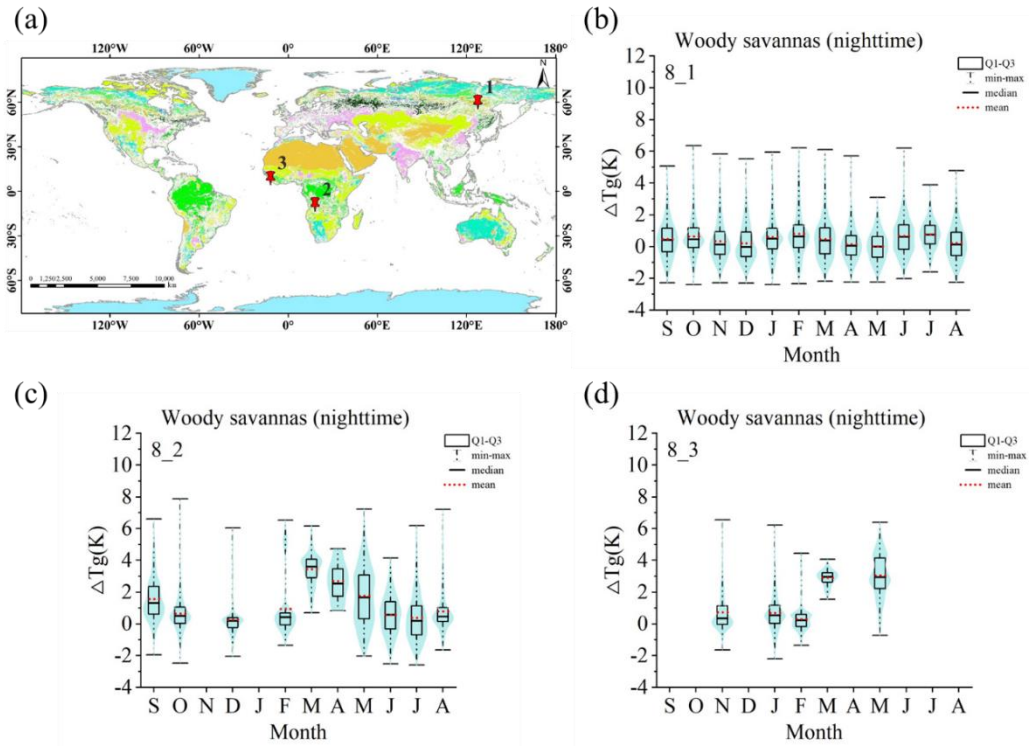


Fig 4.22 (a) Geographic distribution of the study sites. (b-d) Violin plots of the  $\Delta T_g$  in woody savannas (WSA) during the night from September 2019 to August 2020.

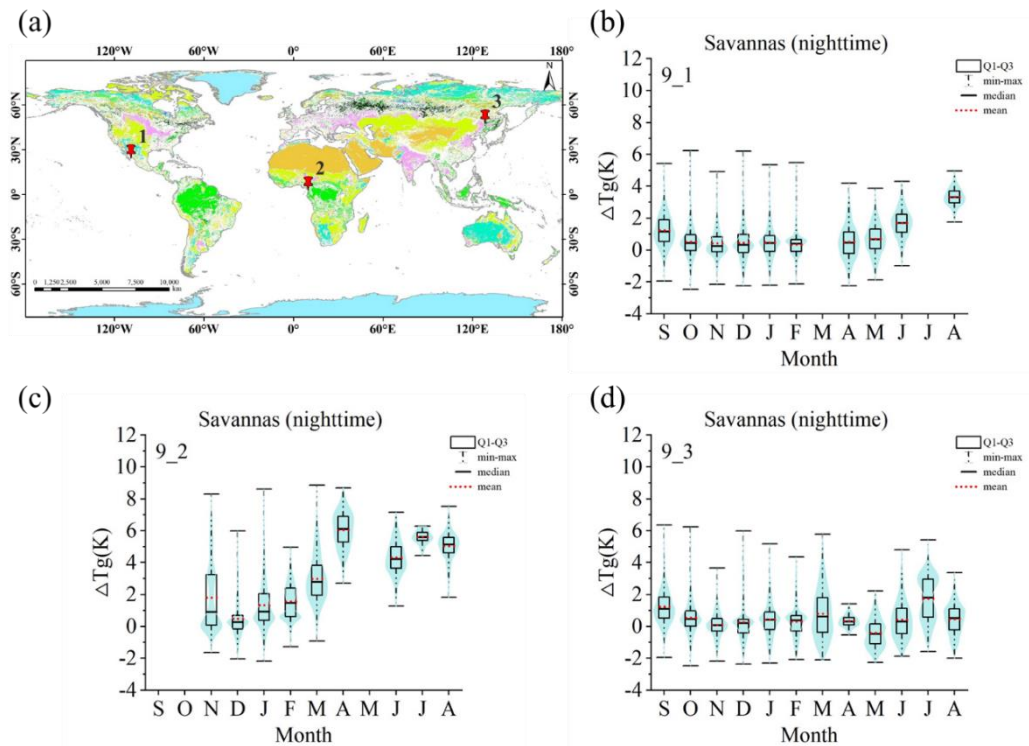


Fig 4.23 (a) Geographic distribution of the study sites. (b-d) Violin plots of the  $\Delta T_g$  in savannas (SVA) during the night from September 2019 to August 2020.

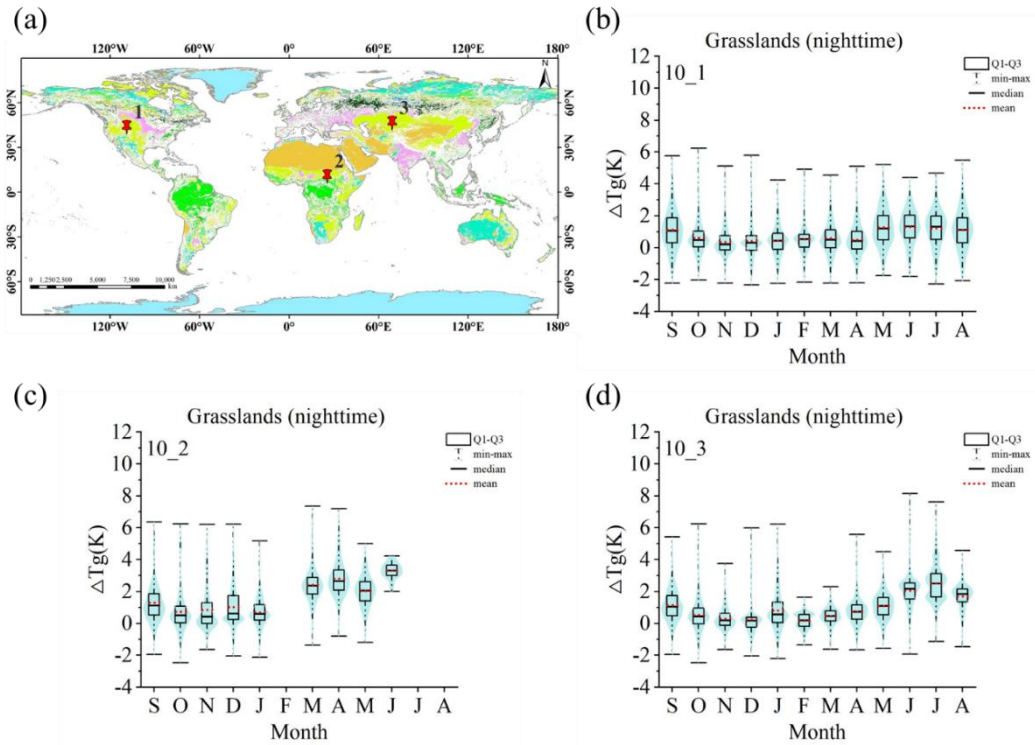


Fig 4.24 (a) Geographic distribution of the study sites. (b-d) Violin plots of the  $\Delta T_g$  in grasslands (GRA) during the night from September 2019 to August 2020.

Temporal patterns of WET sites are not uniform during nighttime. Site 11-1 locates in low latitude region, showing the strongest fluctuation in the study period, while site 11-3 locates in high latitude region with minimal monthly variation of the mean  $\Delta T_g$ . Fluctuation of site 11-2 is moderate comparing with other two sites, but the variation of the mean  $\Delta T_g$  is quite high. The variation of the mean  $\Delta T_g$  of CRO sites is significant during daytime (as shown in Fig 4.12). However, during nighttime, the variation of the mean  $\Delta T_g$ , though distinguishable, is not as high. Sowing and harvesting do not affect the mean  $\Delta T_g$  as expected. URB sites should have stable temporal variation in vegetation, resulting in stable annual  $\Delta T_g$ . While all the three URB sites show an increase of  $\Delta T_g$  in the summer season. The temporal patterns of the mean  $\Delta T_g$  of CVM sites are the fusion of cropland and natural vegetation, the temporal variation of CVM sites is higher than that of CRO sites and smaller than that of forest sites. Among all the land cover types, SNO sites are the most unique ones. Despite data missing in several months, the mean  $\Delta T_g$  of SNO sites are the smallest among all land cover types, the annual variation of  $\Delta T_g$  is also minimal. Considering the properties of SNO sites are quite stable in the whole year, it is reasonable that  $\Delta T_g$  stays stable for SNO sites during both nighttime and daytime. Comparing the plots of Fig 4.30 and Fig 4.16, BSV sites

have the hugest difference of temporal fluctuation of  $\Delta T_g$  during nighttime and daytime. The annual variation of  $\Delta T_g$  is strong during daytime but minimal during nighttime. The standard deviation of  $\Delta T_g$  is small, and relatively stable for all the three BSV sites.

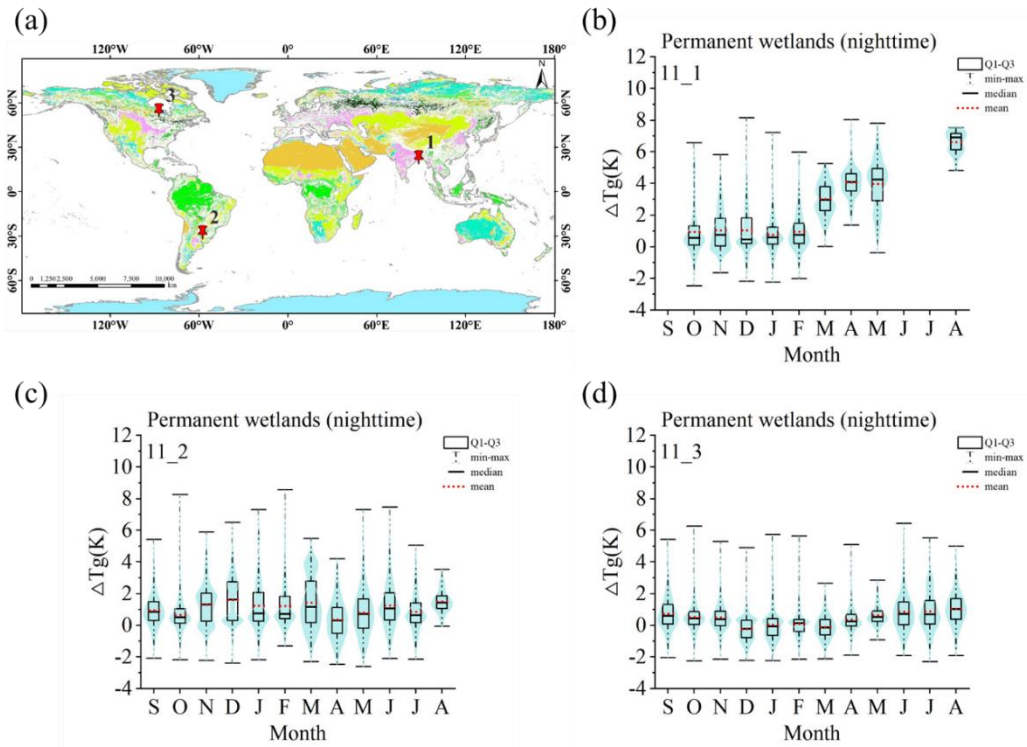


Fig 4.25 (a) Geographic distribution of the study sites. (b-d) Violin plots of the  $\Delta T_g$  in permanent wetlands (WET) during the night from September 2019 to August 2020.

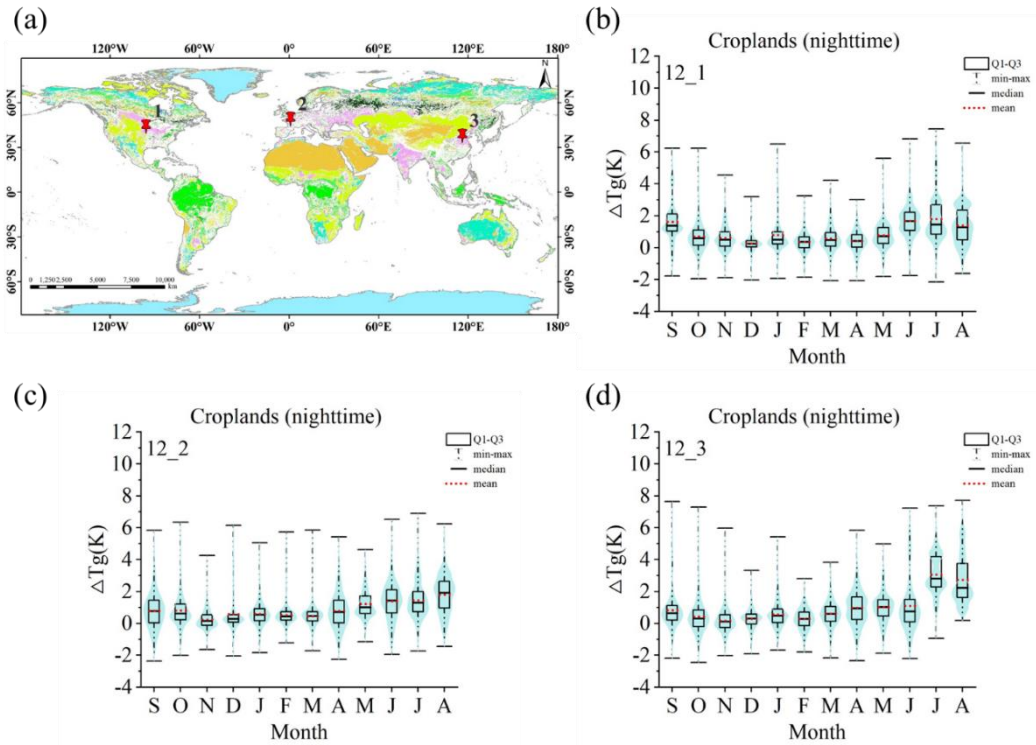


Fig 4.26 (a) Geographic distribution of the study sites. (b-d) Violin plots of the  $\Delta T_g$  in croplands (CRO) during the night from September 2019 to August 2020.

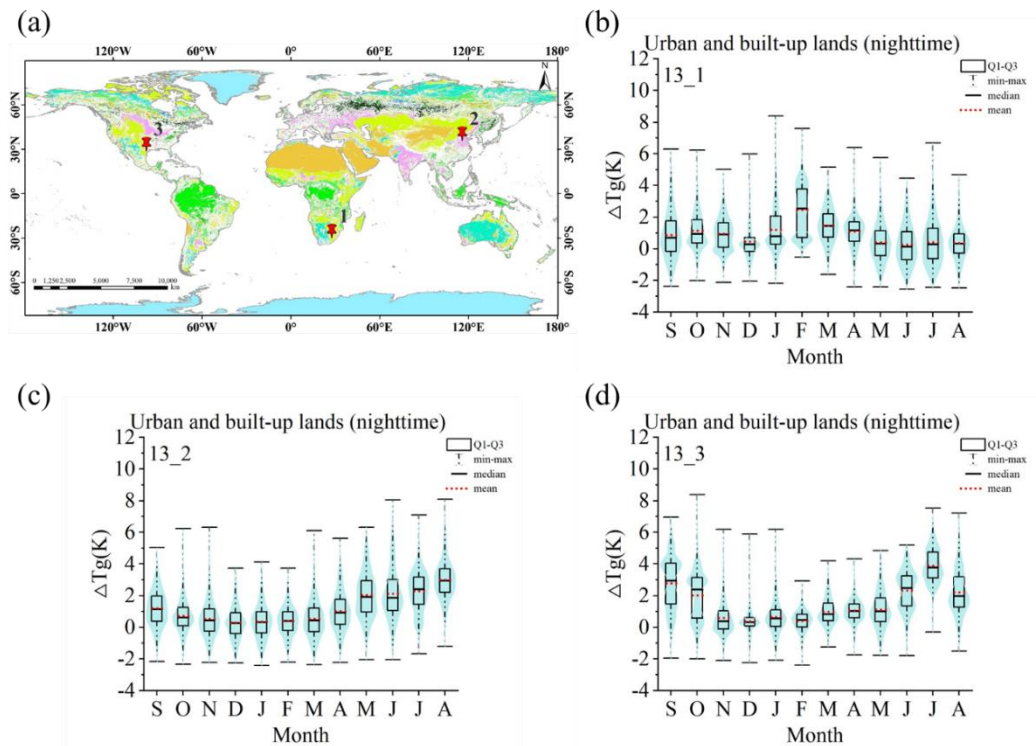


Fig 4.27 (a) Geographic distribution of the study sites. (b-d) Violin plots of the  $\Delta T_g$  in urban and built-up lands (URB) during the day from September 2019 to August 2020.

Chapter 4. Angular effects of surface brightness temperatures observed from SLSTR data

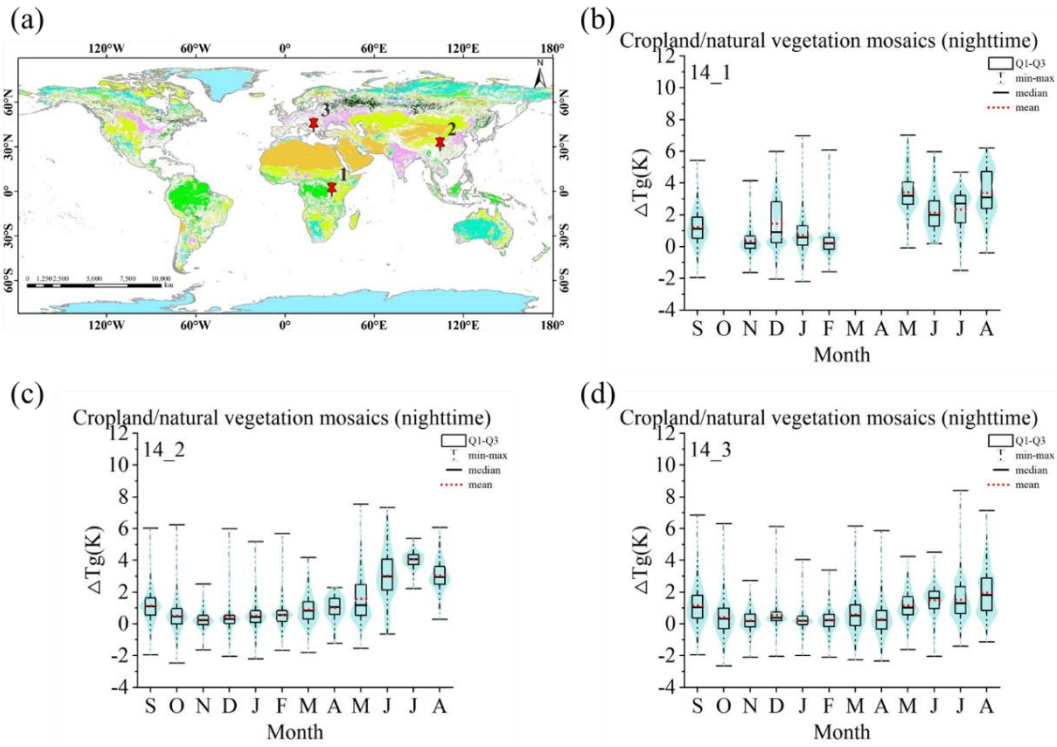


Fig 4.28 (a) Geographic distribution of the study sites. (b-d) Violin plots of the  $\Delta T_g$  in cropland/natural vegetation mosaic (CVM) during the night from September 2019 to August 2020.

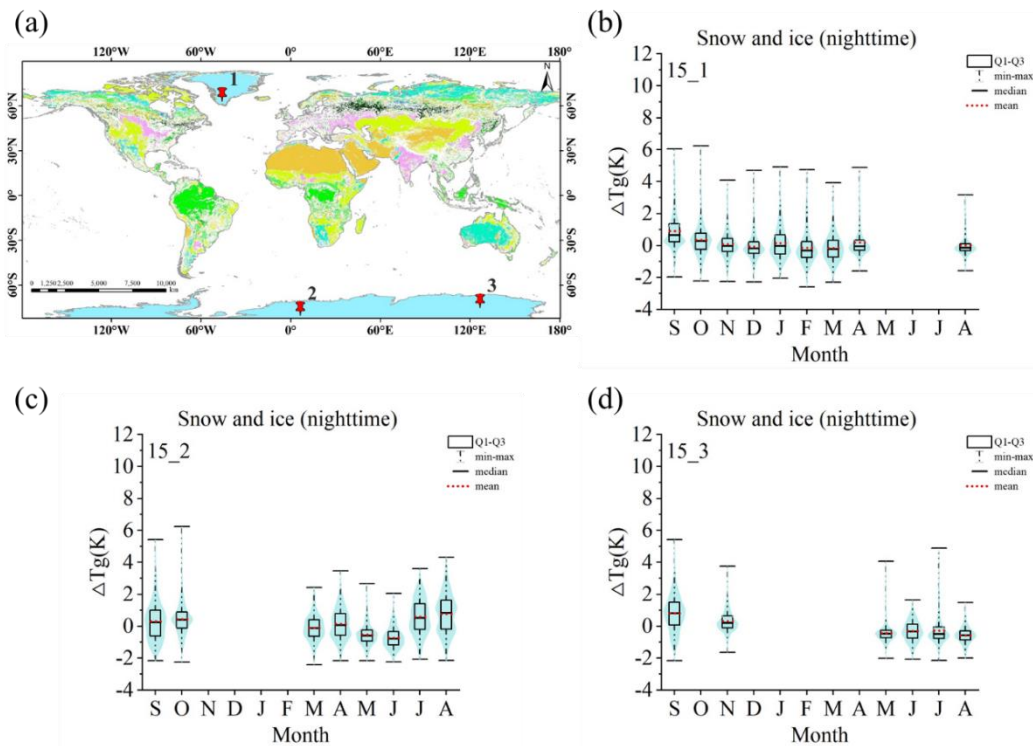


Fig 4.29 (a) Geographic distribution of the study sites. (b-d) Violin plots of the  $\Delta T_g$  in snow and ice (SNO) during the night from September 2019 to August 2020.

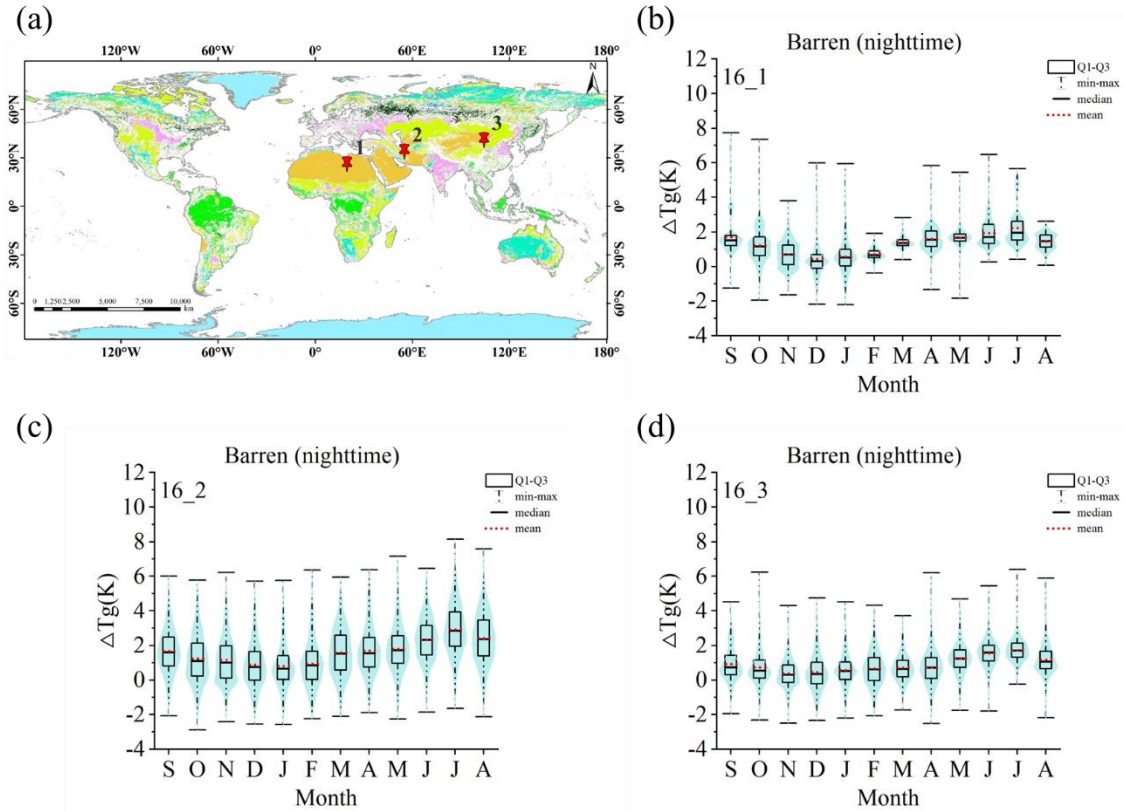


Fig 4.30 (a) Geographic distribution of the study sites. (b-d) Violin plots of the  $\Delta T_g$  in barren or sparsely vegetated (BSV) during the night from September 2019 to August 2020.

### 4.2.2 Season

The bar plots of  $\Delta T_g$  in different seasons during daytime at northern hemisphere are shown in Fig 4.31. Overall  $\Delta T_g$  during daytime in Spring and Summer is higher than that in Autumn and Winter. EBF, SVA and BSV have the highest average  $\Delta T_g$  in the whole year. The seasonal variation of  $\Delta T_g$  of those land cover types is also minimal. EBF, SVA and GRA have relatively higher  $\Delta T_g$  in Winter season, indicating their seasonal variation is not significant. SNO has the lowest  $\Delta T_g$  in Spring, Summer and Autumn. In Winter, MF has the lowest  $\Delta T_g$ . For most land cover types, the standard deviation of  $\Delta T_g$  ranges from 1 K to 3 K. Basically, high standard deviation values are often accompanied by high  $\Delta T_g$  values.

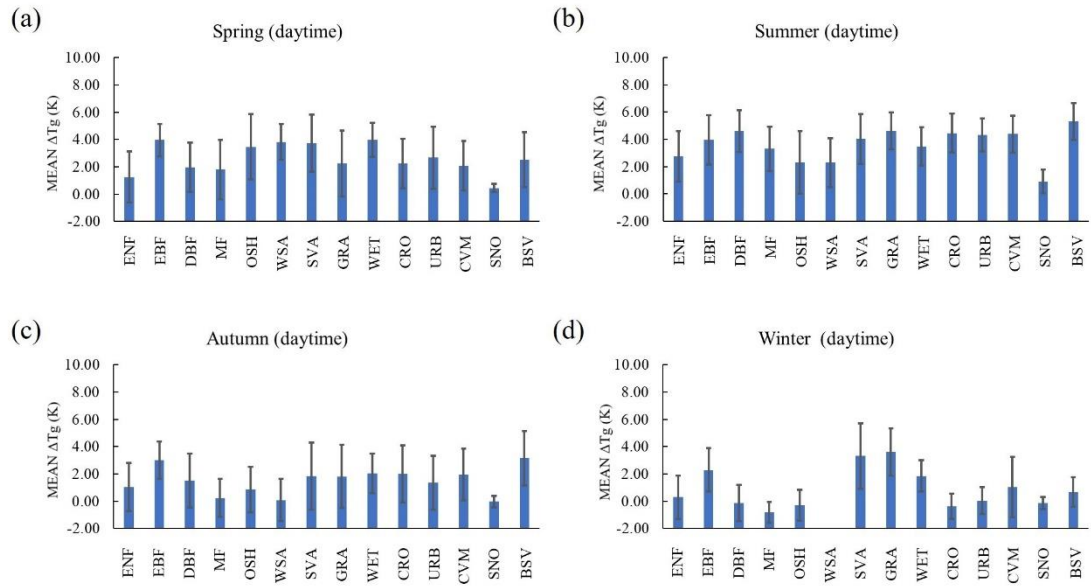


Fig 4.31 The bar chart of the  $\Delta T_g$  in different seasons during daytime at northern hemisphere: (a) spring, (b) summer, (c) autumn, and (d) winter. The length of the blue rectangle represents the mean value, and half the length of the black line represents the standard deviation.

Fig 4.32 illustrates the  $\Delta T_g$  in different seasons during nighttime in northern hemisphere. The overall  $\Delta T_g$  during nighttime is lower than that during daytime. Meanwhile, the seasonal difference of  $\Delta T_g$  during nighttime is not as significant as that during daytime. The seasonal variation patterns of all fourteen land cover types are presenting consistent trend. EBF has the highest  $\Delta T_g$  during all four seasons in the whole year. MF and SNO have the lowest annual  $\Delta T_g$  during the study period. The standard deviation of  $\Delta T_g$  during nighttime is also lower than that during daytime, ranging from approximately 1 K to 2 K.

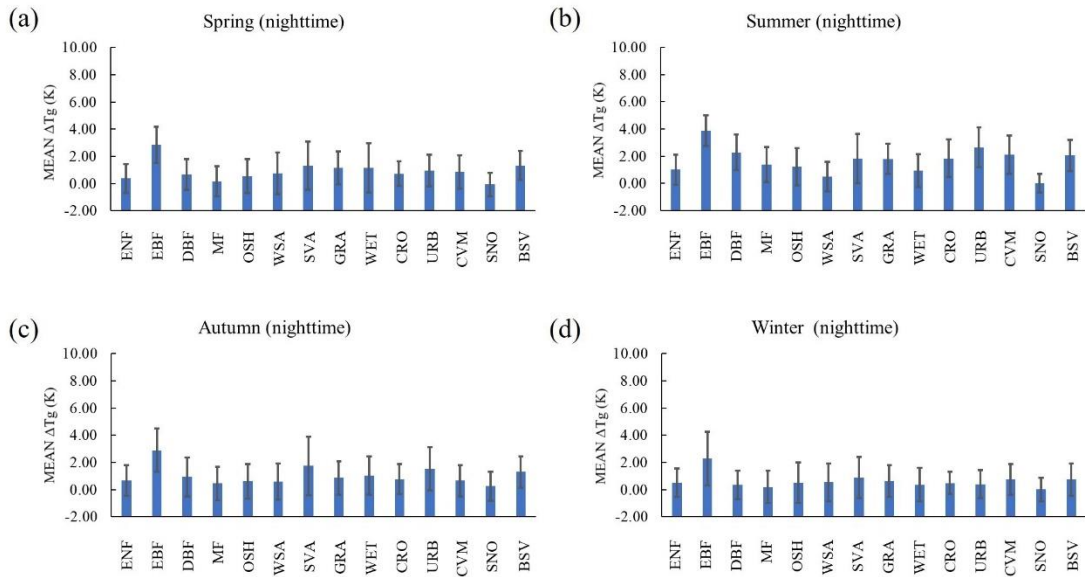


Fig 4.32 The bar chart of the  $\Delta T_g$  in different seasons during nighttime at northern hemisphere: (a) spring, (b) summer, (c) autumn, and (d) winter. The length of the blue rectangle represents the mean value, and half the length of the black line represents the standard deviation.

The bar plot of  $\Delta T_g$  in different seasons during daytime in southern hemisphere is shown in Fig 4.33. Data integrity is not as good as it in northern hemisphere. Data is available for only seven land cover types in southern hemisphere. There is no available data for analysis for OSH, WSA and SNO during Summer nor for SNO during Winter. Based on the existing data, it appears that the seasonal variation of  $\Delta T_g$  during daytime in southern hemisphere is not significant. ENF, DBF, WET and URB, the land cover types that have complete data in all four seasons, present a stable  $\Delta T_g$  in the whole year, though with slightly low  $\Delta T_g$  during Winter. OSH, WSA and SNO, though with missing data in some seasons, don't show noticeable seasonal fluctuation. The range of standard deviation of  $\Delta T_g$  during daytime in southern hemisphere is from 1 K to 2 K.

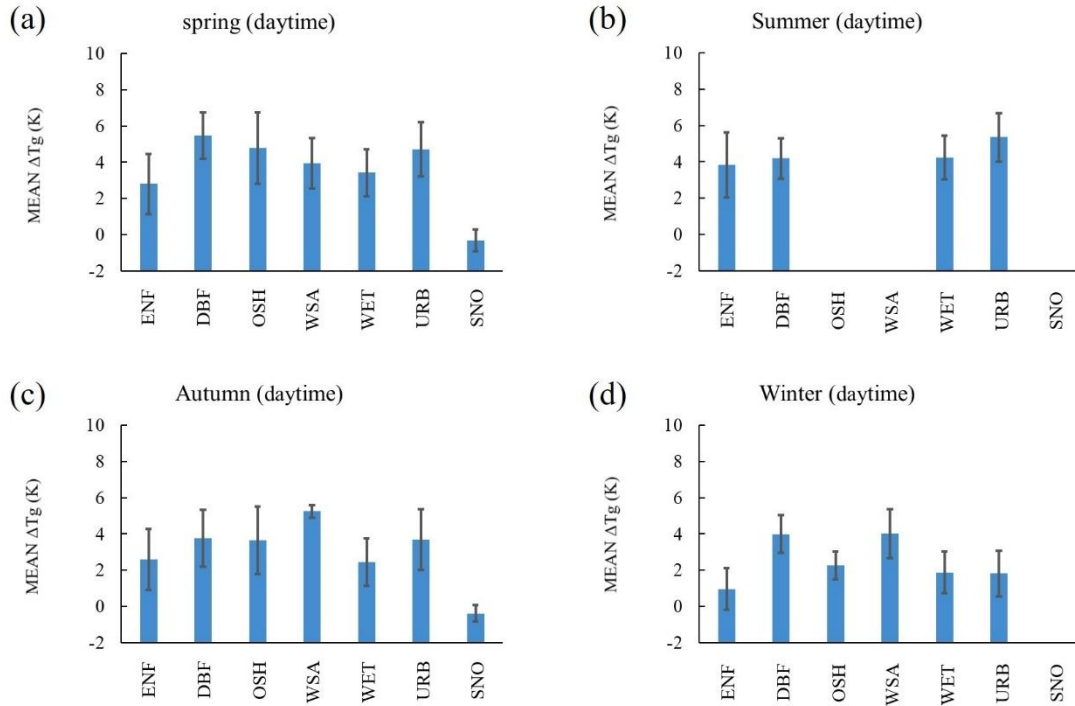


Fig 4.33 The bar chart of the  $\Delta T_g$  in different seasons during daytime at southern hemisphere: (a) spring, (b) summer, (c) autumn, and (d) winter. The length of the blue rectangle represents the mean value, and half the length of the black line represents the standard deviation.

Fig 4.34 demonstrates  $\Delta T_g$  during nighttime in southern hemisphere. Comparing with  $\Delta T_g$  during daytime, the season fluctuation of  $\Delta T_g$  during nighttime in southern hemisphere is slightly apparent. The Summer-Winter difference of  $\Delta T_g$  during nighttime can reach 3 K or 4 K for most land cover types. DBF, OSH and WSA present a significant seasonal variation. DNF, WET and URB present moderate seasonal variation, with Summe-Winter difference of  $\Delta T_g$  at approximately 1 K to 2 K. SNO provides no available data during summer, and data collected from other seasons show a stable  $\Delta T_g$  value.

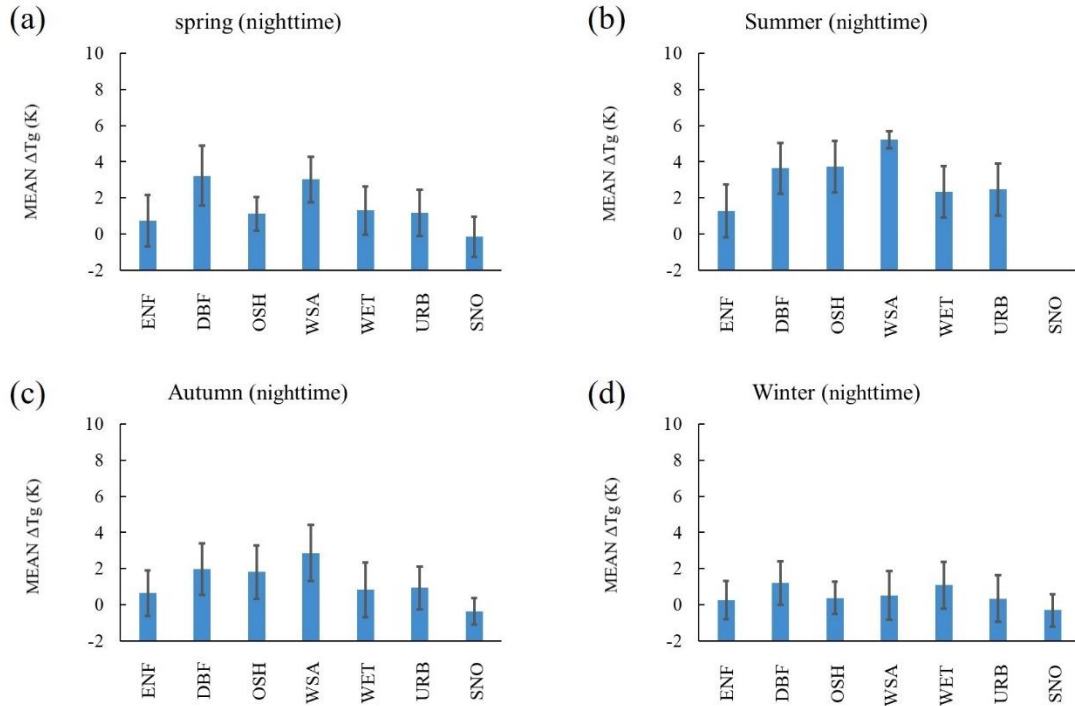


Fig 4.34 The bar chart of the  $\Delta T_g$  in different seasons during nighttime at southern hemisphere: (a) spring, (b) summer, (c) autumn, and (d) winter. The length of the blue rectangle represents the mean value, and half the length of the black line represents the standard deviation.

### 4.2.3 Latitude

To analysis the distribution of  $\Delta T_g$  along with the change of latitude, the global data is separated into six different latitude zones by the latitude line of 0, 30, and 60 degrees, which are low-, mid- and high-latitude zones in northern and southern hemisphere, respectively.

The variation of mean and standard deviation of  $\Delta T_g$  in six latitude zones is illustrated in Fig 4.35. Mean  $\Delta T_g$  locates in the range between -0.5 K to 4 K, with the minimal value appears in high-latitude zones in southern hemisphere. In low-latitude zones in northern and southern hemisphere,  $\Delta T_g$  is high, with value around 3.5 K. In mid-latitude zone in northern hemisphere,  $\Delta T_g$  is approximately 2 K, a little bit lower than that in mid-latitude zone in southern hemisphere with a value of approximately 2.8 K.  $\Delta T_g$  is about 1 K in high-latitude zone in northern hemisphere, while  $\Delta T_g$  is lower than 0 K in high-latitude zone in the southern hemisphere. In high-latitude zone in the southern hemisphere, standard deviation of  $\Delta T_g$  is obviously lower than that in other five zones.

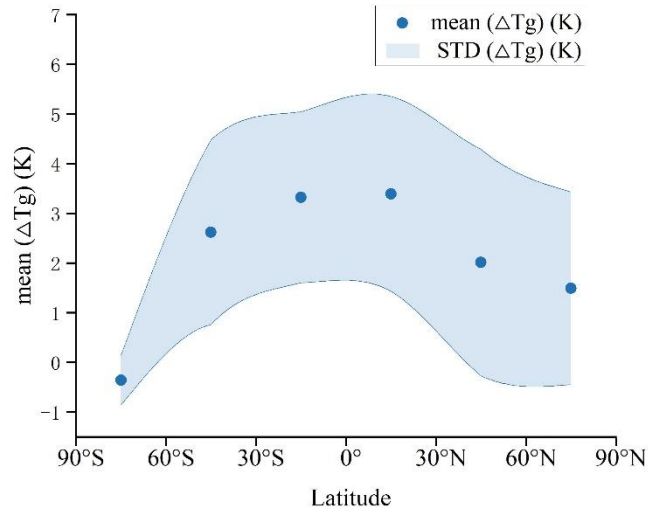


Fig 4.35 Variation of mean and standard deviation of  $\Delta T_g$  at northern and southern hemisphere, respectively. The points show the mean value of  $\Delta T_g$  in high-, mid-, low-latitude at northern and southern hemisphere, respectively. And the shaded upper and lower ends are the range of mean  $(\Delta T_g) \pm \text{STD}$ .

The temporal variation of  $\Delta T_g$  in daytime and nighttime in six latitude zones is shown as heat map in Fig 4.36. Regarding to data availability, there is available data in all twelve months during the study period except for high-latitude zone in southern hemisphere, which only has available data in two months in daytime and nine months in nighttime.

By comparing the size of circle in Fig 4.36 (a) and (b), it is shown that the overall mean  $\Delta T_g$  in daytime is higher than that in nighttime. The color of circle in daytime is warmer than that in nighttime, showing that the standard deviation in daytime is also higher than that in nighttime. In terms of temporal variation,  $\Delta T_g$  is lower in winter season (from November to March) than in summer season (from May to September) in northern hemisphere. The situation reverses in southern hemisphere, with higher  $\Delta T_g$  in winter season than in summer season. It is reasonable because solar zenith angle is lower in summer season than in winter season in northern hemisphere, and  $\Delta T_g$  is negatively related to solar zenith angle.

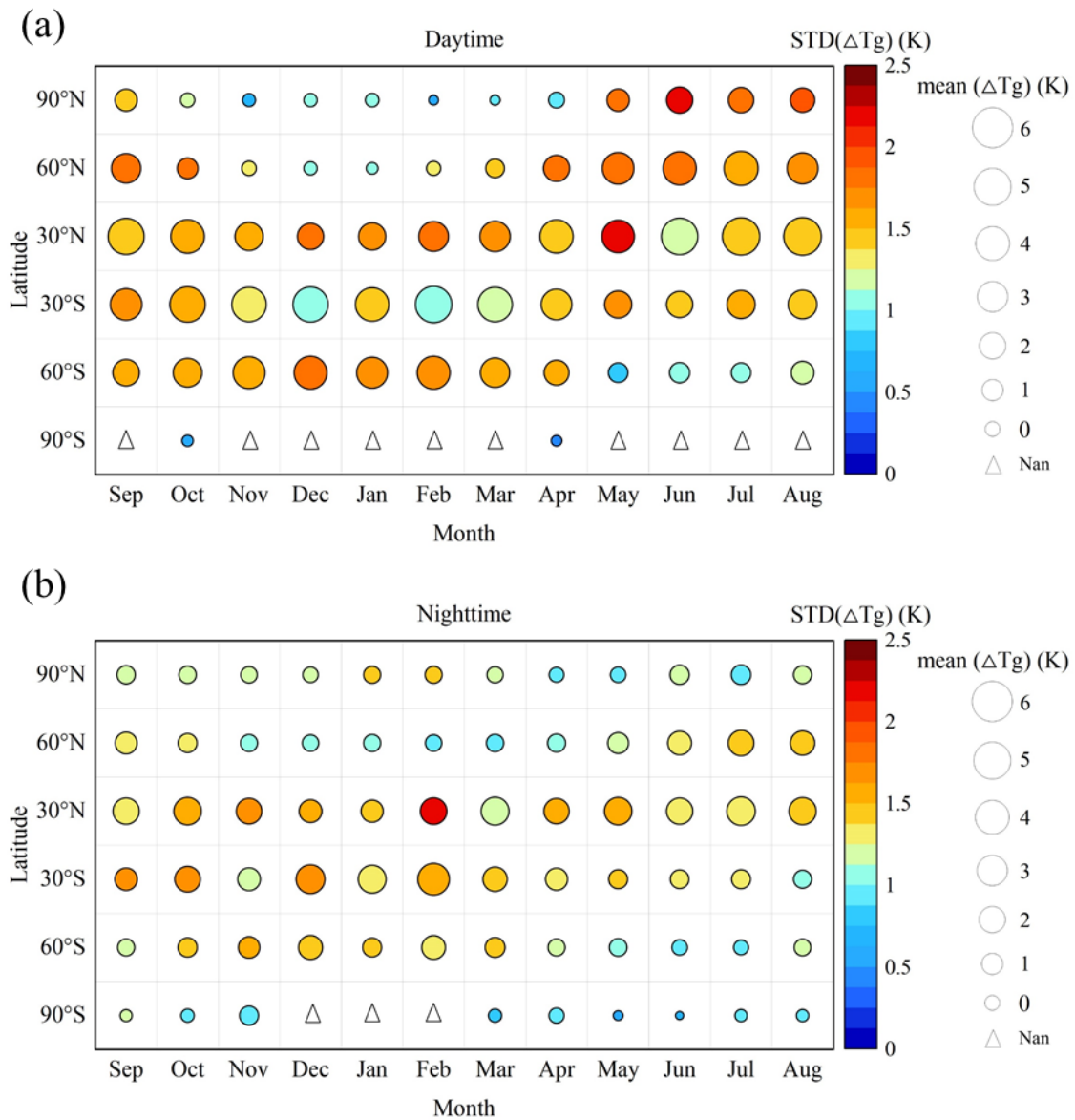


Fig 4.36 Heatmap of the mean and standard deviation of  $\Delta T_g$  during (a) daytime and (b) nighttime in high-, mid-, low-latitude at northern and southern hemisphere, respectively. Color represents standard deviation, circle indicates the mean value of  $\Delta T_g$ , and triangle means no value.

#### 4.2.4 Solar zenith angle

The relationship between solar zenith angle in each  $10^\circ$  interval and  $\Delta T_g$  is shown in Fig 4.37. The value of mean  $\Delta T_g$  stays positive in all the cases. In general, mean  $\Delta T_g$  shows a descending trend with the increase of solar zenith angle, ranging from approximately 6 K to 0 K. Especially, in cases where solar zenith angle falls within the range between  $20^\circ$  and  $70^\circ$ ,  $\Delta T_g$  presents a direct downward trend. In cases where solar

zenith angle is higher than  $70^\circ$ ,  $\Delta T_g$  remains stable, indicating that angular effect of brightness temperature is negligible when solar zenith angle is high. The standard deviation of  $\Delta T_g$  is around 1.5 K in most cases except for that where solar zenith angle is  $20^\circ$ .

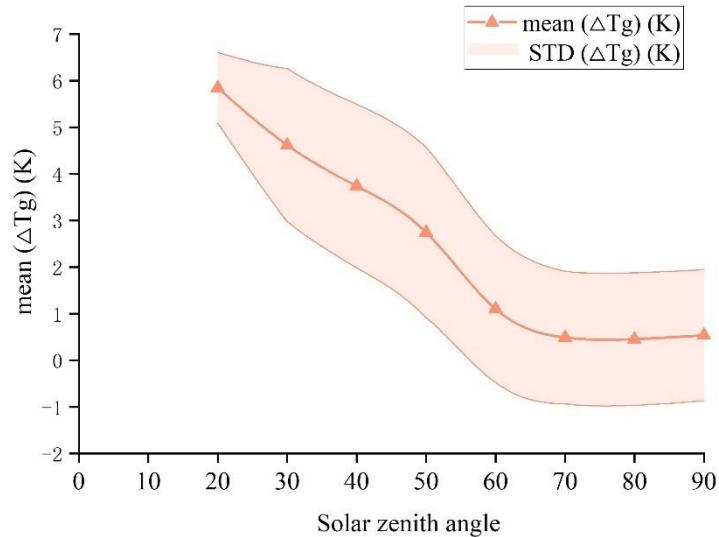


Fig 4.37 Variation of mean and standard deviation of  $\Delta T_g$  at different solar zenith angles. The triangles show the mean value of  $\Delta T_g$  in each  $10^\circ$  interval of the solar zenith angles, and the color-shaded bands upper and lower are the range of  $\text{mean}(\Delta T_g) \pm \text{STD}$ .

To analysis the distribution of  $\Delta T_g$  in the six zones, Fig 4.38 demonstrates the scatter plot of solar zenith angle and  $\Delta T_g$  with density slice in six different latitude zones, respectively. Generally speaking, mean  $\Delta T_g$  shows descending trend with the increase of solar zenith angle in all the six latitude zones except for that in high-latitude zone in southern hemisphere, in which the number of available data is insufficient to show an apparent trend. The highest density of scatter points occurs in high-latitude zones when solar zenith angle is at nearly  $90^\circ$ . The highest density of scatter points in mid- and low-latitude zones occurs when solar zenith angle is between  $50^\circ$  and  $70^\circ$ . Comparing  $\Delta T_g$  in low-, mid- and high-latitude zones, it is apparent that  $\Delta T_g$  in high-latitude zones is lower than that in mid- and low-latitude zones. The distribution of scatter points shows similar pattern in mid- and low-latitude zones in both northern and southern hemisphere, with a descending trend with solar zenith angle.

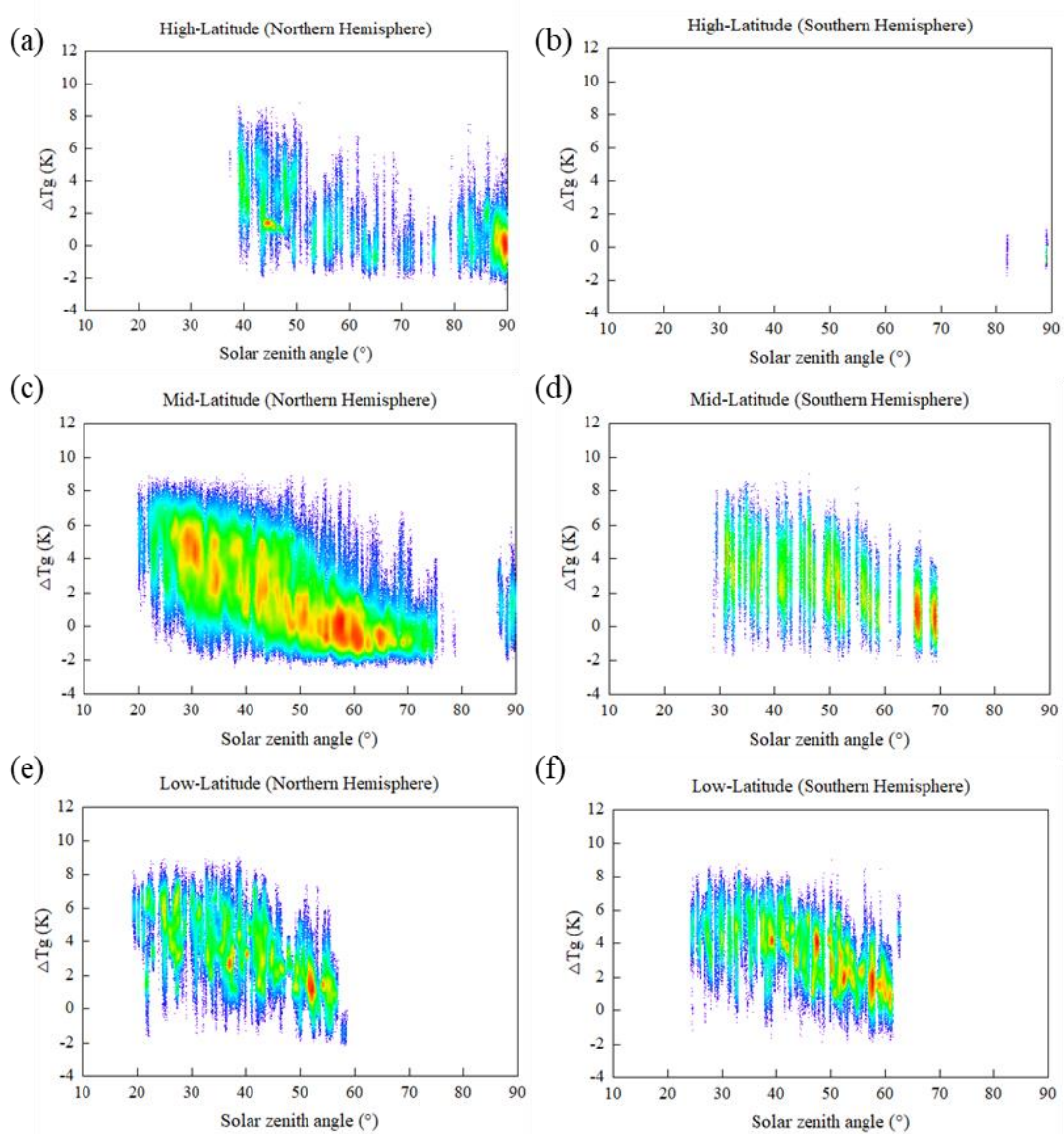


Fig 4.38 A density plot of solar zenith angle and  $\Delta T_g$  in high-, mid-, low-latitude, for (a), (c), (e) at northern and for (b), (d), (f) southern hemisphere, respectively. Red indicates a higher distribution density of  $\Delta T_g$ , while blue indicates a lower distribution density of  $\Delta T_g$ .

## 4.2.5 Climate

Fig 4.39 presents the seasonal variation of the mean  $\Delta T_g$  of different land cover types in tropical zone during daytime and nighttime. The overall mean  $\Delta T_g$  during daytime is a little bit higher than that during nighttime.

During daytime, the majority of the mean  $\Delta T_g$  is distributed between 3 K and 6 K. WET shows a relatively low mean  $\Delta T_g$  in autumn and winter. This may be related to the high soil moisture content in WET area.

During nighttime, DBF and WSA present similar seasonal variation, with high mean  $\Delta T_g$  occurring in summer and low mean  $\Delta T_g$  occurring in winter. The maximum mean  $\Delta T_g$  can reach 7 K for WET in summer and the minimum mean  $\Delta T_g$  is as low as 1 K for WET in winter. There is no noteworthy seasonal variation for other land cover types during nighttime.

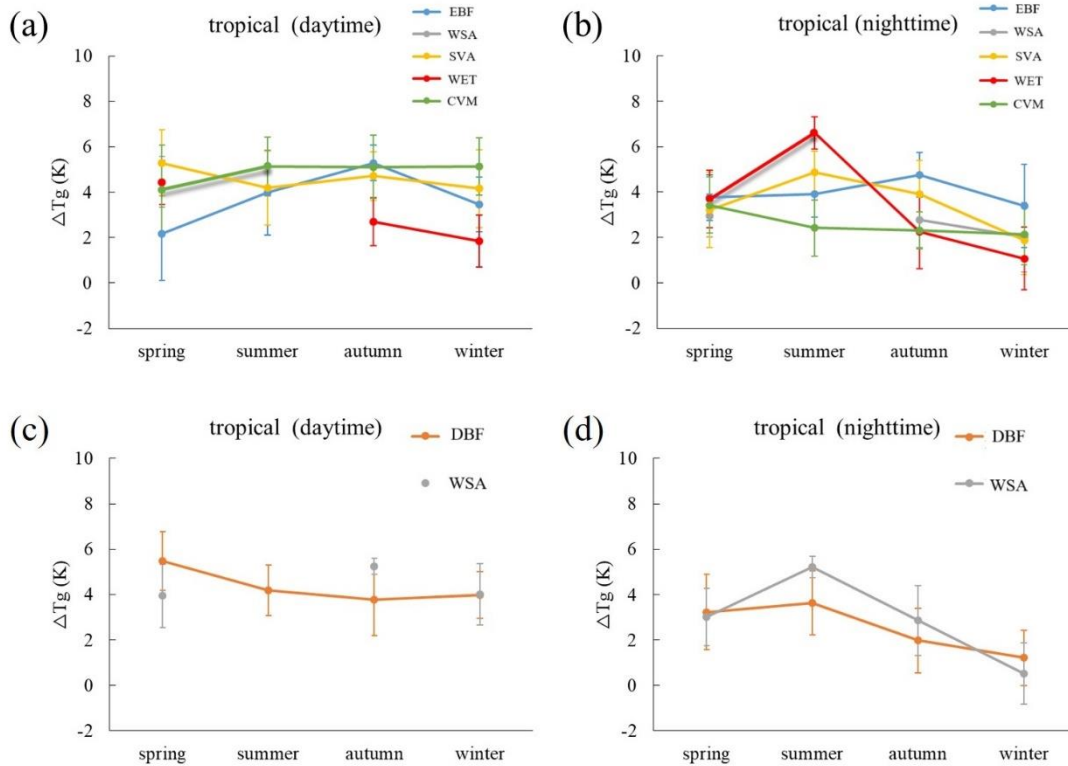


Fig 4.39 Mean  $\Delta T_g$  of tropical during daytime and nighttime, for (a) and (b) at northern hemisphere, and for (c) and (d) at southern hemisphere, respectively.

Fig 4.40 presents the seasonal variation of the mean  $\Delta T_g$  of different land cover types in arid climate zone during daytime and nighttime. The difference of the mean  $\Delta T_g$  during daytime and nighttime is also higher than that in tropical zone. Comparing with the overall mean  $\Delta T_g$  during daytime, the mean  $\Delta T_g$  during nighttime is notably lower, with all the data points distributed between 0 K and 2 K.

The seasonal variation in all the four land cover types (OSH, SVA, GRA, and BSV) during both daytime and nighttime significant, reaching peak in summer and valley in winter, except for GRA which shows a rise in winter season during daytime.

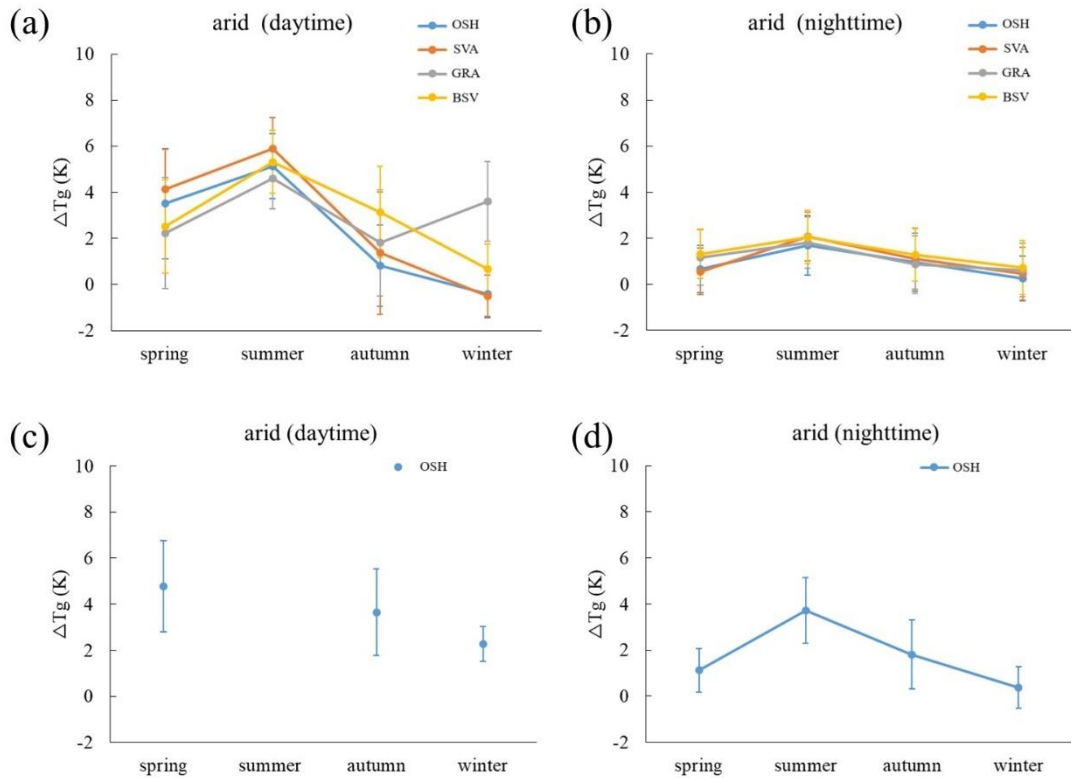


Fig 4.40 Mean  $\Delta T_g$  of arid during daytime and nighttime, for (a) and (b) at northern hemisphere, and for (c) and (d) at southern hemisphere, respectively.

The result of temperate zone is shown in Fig 4.41. There is more land cover types distributed in temperate zones, including ENF, EBF, DBF, CRO, URB, and CVM. The day-night difference of the mean  $\Delta T_g$  is also apparent in temperate zone.

During daytime, ENF, DBF, CRO and CVM presents seasonal fluctuation similar to that in arid zone. For EBF and URB, the mean  $\Delta T_g$  in spring season is a little bit higher than that in summer season. The possible reason could be that the vegetation in EBF and URB is relatively stable than other land cover types.

During nighttime, the seasonal variation is not as significant as that during daytime, though most land cover types show similar seasonal fluctuation with daytime. CRO shows the most significant seasonal fluctuation during nighttime. For other land cover types, the seasonal fluctuation is lower than 3 K.

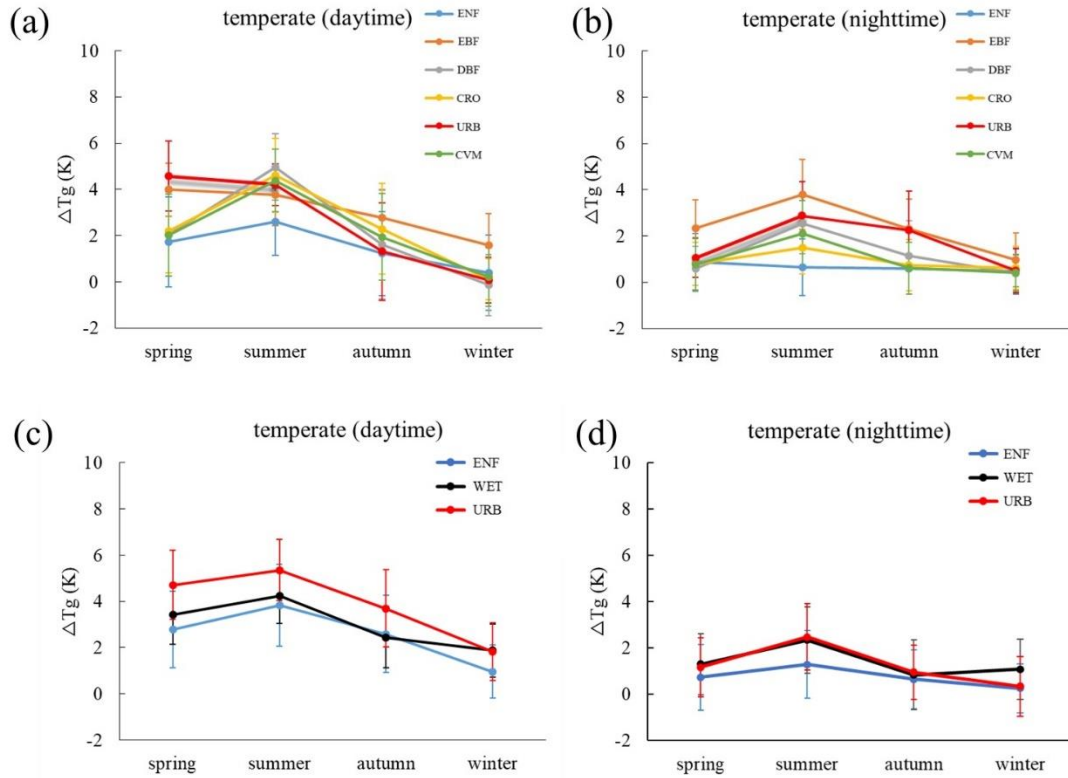


Fig 4.41 Mean  $\Delta T_g$  of temperate during daytime and nighttime, for (a) and (b) at northern hemisphere, and for (c) and (d) at southern hemisphere, respectively.

The distribution of the mean  $\Delta T_g$  in cold and polar zones are shown in Fig 4.42 and Fig 4.43. There are available data in nine land cover types in northern hemisphere and no available data in southern hemisphere.

During daytime, the seasonal variation is noticeable. Most land cover types present the peak-in-summer pattern similar to arid and temperate zones. WSA and OSH are the exception. It is reasonable since the two land cover types share similar property, that is low vegetation cover and stable temporal variation.

The mean  $\Delta T_g$  is between 0 K and 2 K in most cases during nighttime. CRO and URB present a relatively high mean  $\Delta T_g$  in summer season, but the value of the mean  $\Delta T_g$  is no higher than 2.5 K, much lower than that in other climate zones.

There is only one land cover type distributed in polar climate zone, and that is SNO.  $\Delta T_g$  is almost negligible in this climate zone. The maximum of  $\Delta T_g$  is lower than 1 K. The seasonal fluctuation is also inapparent.

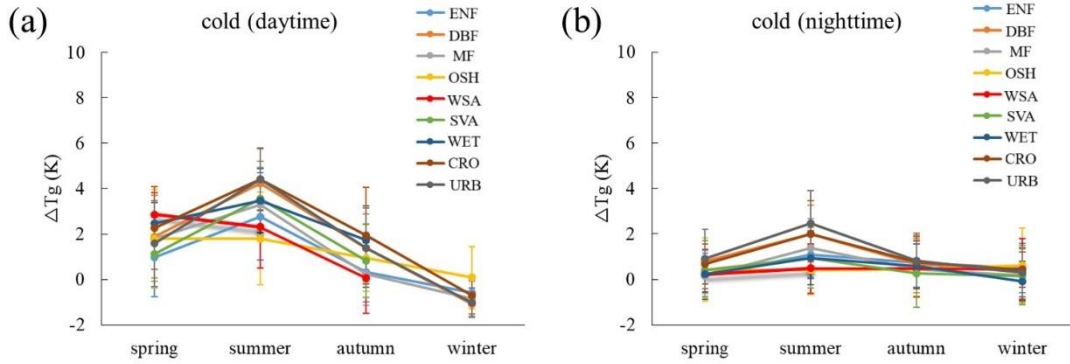


Fig 4.42 Mean  $\Delta T_g$  of cold during daytime and nighttime, for (a) and (b) at northern hemisphere.

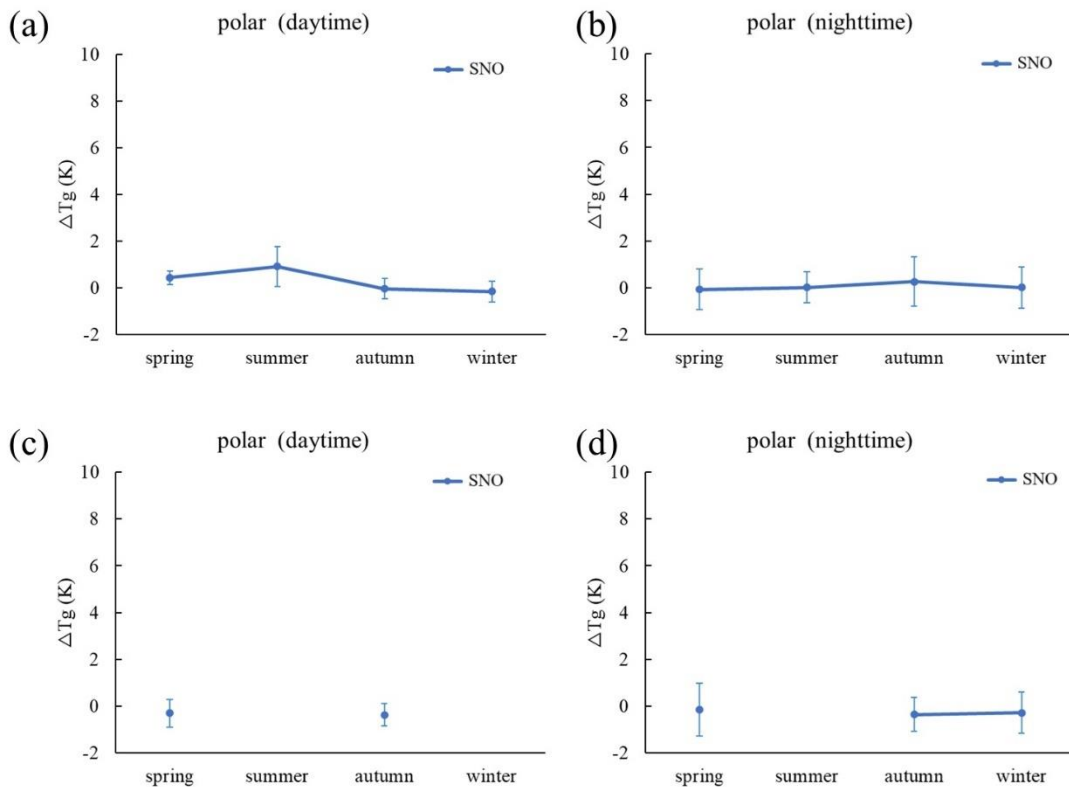


Fig 4.43 Mean  $\Delta T_g$  of polar during daytime and nighttime, for (a) and (b) at northern hemisphere, and for (c) and (d) at southern hemisphere, respectively.

### 4.3 Causality of angular effects of surface brightness temperature

The main purpose of this section is to use the GeoDetector to analyze the main driving factors of the angular effects of surface brightness temperature. Considering the complexity of the spatial distribution of surface brightness temperature, this section

selects land use/land cover (LULC), season, latitude, solar zenith angle (SZA), climate, NDVI, DEM and SM as determinants for analysis.

### 4.3.1 Methodology

In order to explore the main driving factors of spatial variability of  $\Delta T_g$  during the study period, GeoDetector was used to analyze  $\Delta T_g$  and its potential driving factors. GeoDetector is a statistical method used to detect spatial heterogeneity of variables and to reveal their driving factors (WANG et al., 2010). The advantage of this method is that it can detect the driving factors of spatial differentiation of the dependent variable, as well as the impact of the interactions between the driving factors (WANG and HU, 2012). GeoDetector consists of four modules: factor detector, interaction detector, risk detector, and ecological detector, among which factor detector, interaction detector, and risk detector are used to explore the driving factors of spatial variability of  $\Delta T_g$  in this study. The basic principles of the three detectors are described in detail below.

#### Factor detector

The factor detector detects the spatial variability of the dependent variable (Y) and the contribution of the determinants (X) on Y, which is quantified by the  $q$ -value (WANG et al., 2016). The calculation of  $q$  can be described as follows:

$$q = 1 - \frac{\sum_{h=1}^L N_h \sigma_h^2}{N \sigma^2} = 1 - \frac{SSW}{SST} \quad (4.1)$$

$$SSW = \sum_{h=1}^L N_h \sigma_h^2, SST = N \sigma^2$$

where  $h=1, 2, \dots, L$ , is the stratification of  $X$  or  $Y$ ,  $N_h$  and  $N$  are the number of units of stratum  $h$  and the entire region, respectively,  $\sigma_h^2$  and  $\sigma^2$  are the variances of  $Y$  for stratum  $h$  and total, respectively,  $SSW$  and  $SST$  are the within and total sum of squares, respectively. The value of  $q$  presents that  $q$  percent of  $Y$  can be contributed by  $X$ . The range of  $q$  is between 0 and 1. A high value of  $q$  indicates a strong contribution of  $X$  on  $Y$ . In some extreme cases, the value of  $q$  can reach 0 or 1, the former indicates that the spatial distribution of  $Y$  is completely depended on  $X$ , and the latter indicates that  $X$  is completely irrelevant with  $Y$ . Transform  $q$  to make it follow a noncentral F-distribution:

$$F = \frac{N - L}{L - 1} \frac{q}{1 - q} \quad (4.2)$$

$$M = \frac{1}{\sigma^2} \left[ \sum_{h=1}^L \mu_h^2 - \frac{1}{N} \left( \sum_{h=1}^L \sqrt{N_h} \mu_h \right)^2 \right] \quad (4.3)$$

$$F \sim F(L-1, N-L; M) \quad (4.4)$$

where  $M$  is parameter of noncentrality,  $Y_h$  is the average of stratum  $h$ . Based on Eq 4.3, the significance of  $q$  can be determined using look-up table or GeoDetector software. In this study, factor detector is used to explore the driving factor of spatial differentiation of  $\Delta T_g$  and the contribution of driving factors on  $\Delta T_g$ .

### Interaction detector

The interaction detector is defined to evaluate whether the intersection of determinants  $X1$  and  $X2$  will increase or decrease the contribution of  $Y$ , and whether these factors have independent effects on  $Y$ .

By calculating and comparing  $q(X1)$ ,  $q(X2)$ , and  $q(X1 \cap X2)$ , the relationship between the two determinants can be classified into the following five cases as shown in Table 4.3.

Table 4. 3 Determination of the interaction type between two independent variables and the dependent variable.

Cases	Interactions
$q(X1 \cap X2) < \text{Min}(q(X1), q(X2))$	Nonlinear weaken
$\text{Min}(q(X1), q(X2)) < q(X1 \cap X2) < \text{Max}(q(X1), q(X2))$	Uni-factor weaken
$q(X1 \cap X2) > \text{Max}(q(X1), q(X2))$	Bi-factor enhancement
$q(X1 \cap X2) = q(X1) + q(X2)$	Independent
$q(X1 \cap X2) > q(X1) + q(X2)$	Nonlinear enhancement

Nonlinear weaken type, refers to the fact that the combined effect of the two determinants after their interaction is weaker than any of the two determinants alone. Uni-factor weaken type, refers to the fact that the combined effect of two determinants after interaction is greater than the minimum of a single determinant for the dependent variable and less than the maximum of a single determinant. Bi-factor enhancement type refers to the interaction between two determinants having a greater influence for the dependent variable than the maximum of a single determinant. Independent type, refers to the combined effect of the interaction between two determinants being equal

to the sum of a single determinant. Nonlinear enhancement type refers to the phenomenon where the influence of the interaction between two determinants is greater than the sum of a single determinant. This study uses an interaction detector to analyze whether the interaction between determinants of spatial differentiation of surface brightness temperature will enhance or weaken their effect on  $\Delta T_g$ .

### Risk detector

Risk detector can calculate the average value of the dependent variable for each category based on different determinants, and determine whether there is a significant difference between two categories. For example, different land cover types have different surface temperatures, and risk detector can identify the land cover type corresponding to the highest surface temperature. The significance of inter-category differences is examined using t-tests:

$$t_{\bar{Y}_{h=1}-\bar{Y}_{h=2}} = \frac{\bar{Y}_{h=1} - \bar{Y}_{h=2}}{\left[ \frac{\text{Var}(\bar{Y}_{h=1})}{n_{h=1}} + \frac{\text{Var}(\bar{Y}_{h=2})}{n_{h=2}} \right]^{1/2}} \quad (4.5)$$

where  $\bar{Y}_h$  represents the average of parameters in sub-region  $h$ ,  $n_h$  is the number of samples in sub-region  $h$ ,  $\text{Var}$  is the variance.  $t$  follows student- $t$  distribution and its degrees of freedom can be calculated as:

$$df = \frac{\frac{\text{Var}(\bar{Y}_{h=1})}{n_{h=1}} + \frac{\text{Var}(\bar{Y}_{h=2})}{n_{h=2}}}{\frac{1}{n_{h=1}} \left[ \frac{\text{Var}(\bar{Y}_{h=1})}{n_{h=1}} \right]^2 + \frac{1}{n_{h=2}} \left[ \frac{\text{Var}(\bar{Y}_{h=2})}{n_{h=2}} \right]^2} \quad (4.6)$$

In this study, the risk detector is used to determine the spatial differences in surface brightness temperature based on different determinants, and to determine the sensitive zones corresponding to each type of determinant.

The process for analyzing the driving factors of spatial heterogeneity in surface temperature is illustrated in Fig 4.44. The main content is to conduct a quantitative analysis of the relationship between  $\Delta T_g$  and driving factors based on the three modules of the geographic detector.

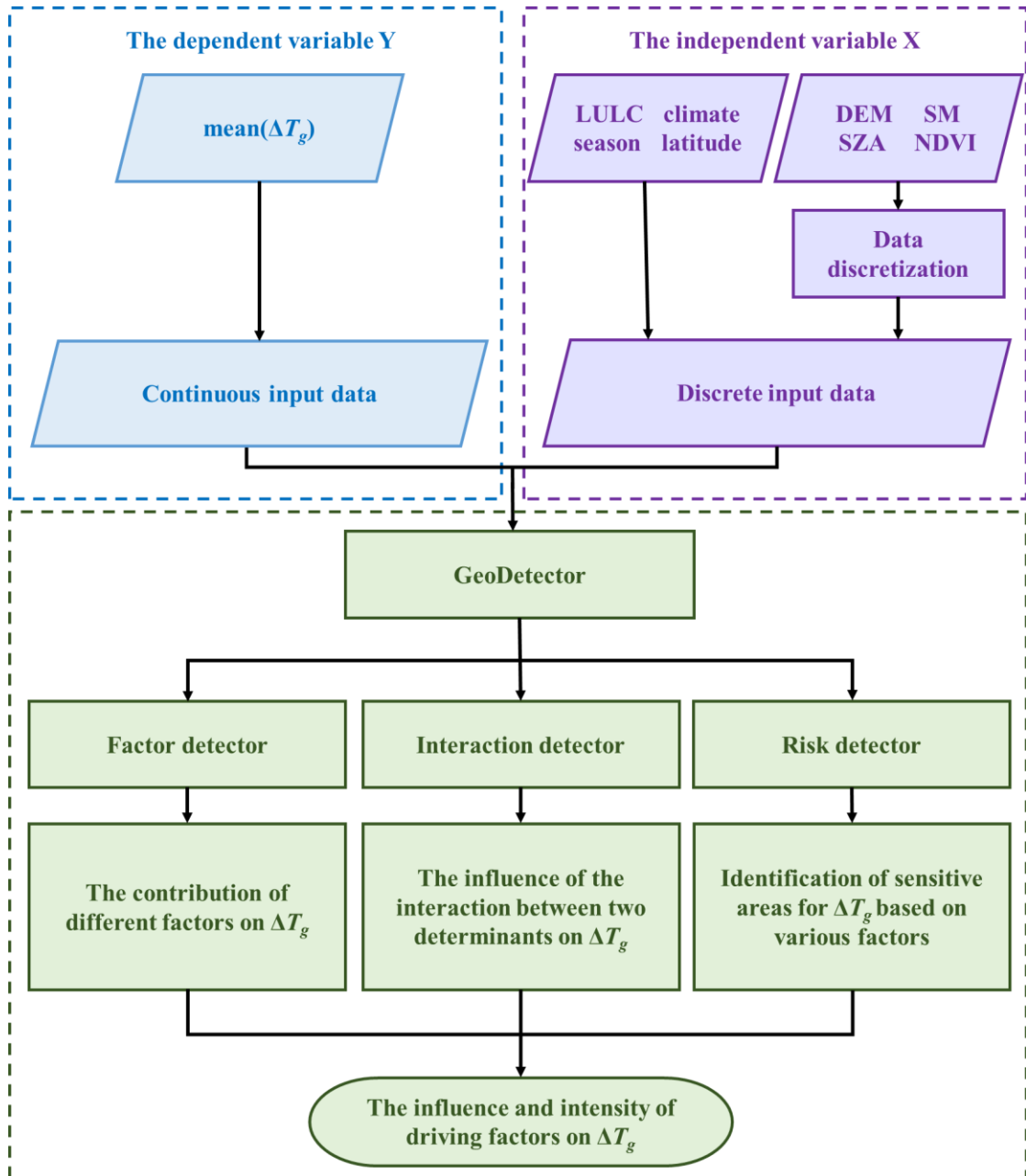


Fig 4.44 Flow chart for the analysis on the determinants of  $\Delta T_g$ .

### 4.3.2 Data processing

For the analysis using the geographic detector, the input data includes the dependent variable Y and the independent variable data X. If an independent variable is continuous, it needs to be discretized. In this study, Y represents mean  $\Delta T_g$  in month, while X includes LULC, climate, season, latitude, DEM, SM, SZA, and NDVI. Among these independent variables, LULC, climate, and season are categorical data, so no discretization is required. Therefore, latitude, DEM, SM, SZA, and NDVI need to be

discretized to determine the final number of categories. Latitude data is divided into three categories, low-, mid- and high-latitudes, based on absolute values, with intervals of 30° between 0° and 90°. DEM is classified into three categories: low elevation (0-0.5 km), medium elevation (0.5-1.5 km), and high elevation (1.5-3.5 km). SM is divided into five intervals within a range of 0-0.5 m<sup>3</sup>/m<sup>3</sup> with an interval of 0.1. SZA is categorized into nine groups ranging from 0° to 90° with a 10° interval. NDVI data is divided into ten groups, ranging from -1 to 1, with an interval of 0.2. Table 4.4 shows the result of discretizing non-type variables. Due to missing data on SM, the overall data volume is reduced by 1/4 during the daytime and 3/4 at nighttime.

Table 4.4 Discrete intervals of dependent variables

Factors	LULC	Climate	Season	Latitude	DEM (km)	SM(m <sup>3</sup> /m <sup>3</sup> )	SZA(°)	NDVI
Dispersion intervals	ENF	tropical	spring	low-latitude	0-0.5	0-0.1	0-10	-1--0.8
	EBF	arid	summer	mid-latitude	0.5-1.5	0.1-0.2	10-20	-0.8--0.6
	DBF	temperate	autumn	high-latitude	1.5-3.5	0.2-0.3	20-30	-0.6--0.4
	MF	cold	winter			0.3-0.4	30-40	-0.4--0.2
	OSH	polar				0.4-0.5	40-50	-0.2--0
	WSA						50-60	0-0.2
	SVA						60-70	0.2-0.4
	GRA						70-80	0.4-0.6
	WET						80-90	0.6-0.8
	CRO							0.8-1
	URB							
	CVM							
	SNO							
BSV								

### 4.3.3 Results

#### 4.3.3.1 The contribution of different factors on $\Delta T_g$

The contribution of the selected determinants to  $\Delta T_g$  during daytime/nighttime in northern/southern hemisphere is shown in Fig 4.45. The statistics of the contribution of the determinants are given in Table 4.5.

During daytime in the northern hemisphere, the contribution of SZA is the strongest, with  $q$  value of 0.65, followed by season with a  $q$  value of 0.32. SM, LULC

and climate are the determinants with moderate contribution, with  $q$  values of 0.18, 0.16, and 0.13, respectively. NDVI, latitude are the determinants with weak contribution, with  $q$  values lower than 0.1. And  $p$  value of DEM is larger than 0.05, the effect is not significant. During daytime in the southern hemisphere, SZA demonstrates a strong contribution to  $\Delta T_g$ , with  $q$  value of 0.75. LULC and season are in the second tier, with  $q$  value of 0.34. Latitude, SM and climate are the determinants with  $q$  value between 0.2 and 0.3. NDVI is the weakest determinant, with  $q$  value at 0.11. Therefore, it is obvious that SZA is the dominant determinant with an overwhelming contribution to  $\Delta T_g$  during daytime in both northern and southern hemisphere. Season is the second strongest determinant with  $q$  value of approximately 0.35. NDVI and DEM are the weakest determinants in terms of contribution to  $\Delta T_g$  during daytime. This may be due to the fact that a location with relatively uniform elevation was selected as the study area.

During nighttime in the northern hemisphere, climate, latitude and LULC rank at the forefront among the eight determinants, with  $q$  values of 0.29, 0.25, and 0.23, respectively. Other determinants are with weak contribution with  $q$  values less than 0.15, ranging from 0.04 to 0.13. During nighttime in the southern hemisphere,  $q$  values are higher than those in the northern hemisphere.  $q$  value of season is 0.48, making it the only determinant that with  $q$  value higher than 0.4. There are five determinants, naming LULC, NDVI, latitude, DEM, and climate with similar  $q$  value between 0.35 and 0.38. SZA and SM are the determinants with the weakest contribution. In summary, during nighttime, there is no one single determinant that overwhelms others in the contribution to  $\Delta T_g$ . The four determinants (LULC, climate, season and latitude) are with similar  $q$  value. SM is the weakest determinant during nighttime in both the northern and southern hemisphere.

Comparing the results of the northern and southern hemisphere, the contribution of determinants is higher in the southern hemisphere than in the northern hemisphere, indicating that in the southern hemisphere,  $\Delta T_g$  is more easily influenced by extrinsic factors.

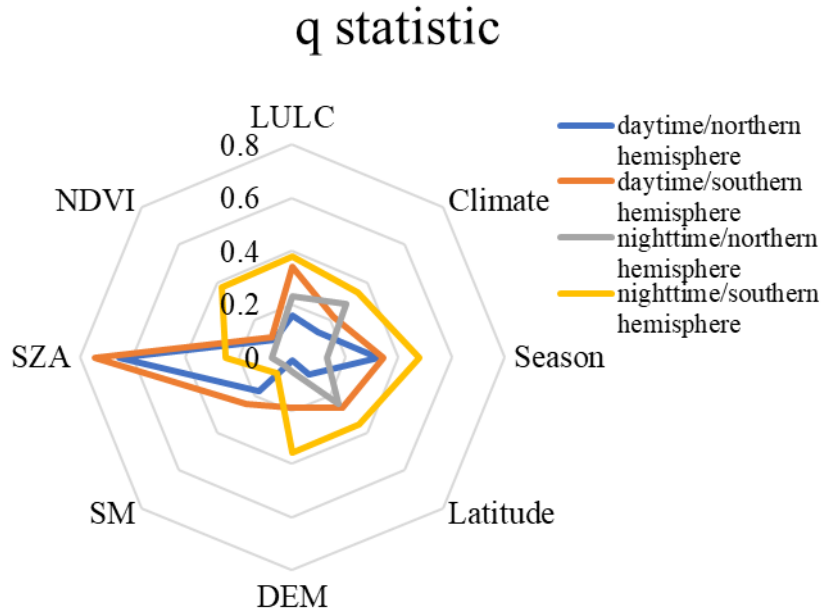


Fig 4.45 The contribution of the selected determinants to  $\Delta T_g$ .

Table 4.5 Statistics on the contribution of individual factor to  $\Delta T_g$ .

	q statistic			
	northern hemisphere		southern hemisphere	
	daytime	nighttime	daytime	nighttime
LULC	0.16**	0.23***	0.34*	0.38***
Climate	0.13***	0.29***	0.22*	0.35***
Season	0.32***	0.13***	0.34**	0.48***
Latitude	0.09***	0.25***	0.27**	0.36***
DEM	0.01	0.05**	0.19*	0.36***
SM	0.18***	0.04	0.25	0.08
SZA	0.65**	0.07	0.74***	0.25
NDVI	0.09**	0.08**	0.11	0.37***

\*means  $p < 0.05$ ; \*\* means  $p < 0.01$ ; \*\*\* means  $p < 0.001$ .

#### 4.3.3.2 The influence of the interaction between two determinants on $\Delta T_g$

GeoDetector is capable to detect spatial heterogeneity and can detect and calculate the interaction between two determinants. To further determine whether the driving factors of  $\Delta T_g$  are independent of each other or interact with each other, this study used the interaction detector to detect the interaction of determinants on contribution to  $\Delta T_g$ , and quantified the intensity of interaction between the determinants. Fig 4.46 shows the results of the interaction between determinants of  $\Delta T_g$  during daytime/nighttime in the northern and southern hemisphere, respectively. The interaction of determinants shows

that the contribution of two determinants combined is higher than that of one single determinant. There are two types of interaction between two determinants, i.e., bi-factor enhancement and nonlinear enhancement.

During daytime in the northern hemisphere, SZA has the strongest contribution to  $\Delta T_g$  as single determinant, the combinations of SZA with other determinants also show a prominent contribution, among which most of the combinations show bi-factor enhancement pattern except for the combination with latitude.  $q$  values of its combinations with LULC and season can reach as high as 0.75, and  $q$  values of its combinations with latitude, SZA, and SM are higher than 0.7. Season is the second strongest determinant. There are some combinations that have  $q$  values higher than 0.6, i.e., combinations with LULC and SZA. LULC, though with a weak contribution to  $\Delta T_g$  as single determinant, is an ideal amplifier when combining with other determinants.  $q$  values of its combination with SZA, season and SM are higher than 0.5.

During daytime in the southern hemisphere, SZA is also the strongest determinant contributing to  $\Delta T_g$ .  $q$  value of SZA itself is already as high as 0.74. Therefore, though  $q$  values of all the combinations are higher than  $q$  value of SZA itself., the enhancement is not significant, showing as bi-factor enhancement pattern with  $q$  values ranging from 0.76 to 0.84. LULC and season are the second-tier determinants, however their combinations show different patterns. The combination of LULC and other weak determinants does not have significant impact on  $q$  values while the combination of season with other determinants shows stronger increase in  $q$  values. The result indicates that season has higher promotion in contributions to  $\Delta T_g$  when combining with other determinants.

$Q$  values during daytime in the southern hemisphere are higher for single determinant than those in the northern hemisphere. Similarly,  $q$  values are still higher in the southern hemisphere when using combinations of determinants. Nonlinear enhancement pattern is more common in the northern hemisphere than in the southern hemisphere. During daytime, the combination between SZA with NDVI or LULC show the highest overall contribution to  $\Delta T_g$ .

During nighttime in the northern hemisphere, there are no determinant showing dominant contribution to  $\Delta T_g$  and the average of  $q$  values is the lowest in the four categories. Though climate, latitude and LULC are the determinants with highest  $q$  values, their combinations between each other do not show significant improvements

in  $q$  values. The strongest combo is the combination between LULC and SM, with  $q$  value of 0.53, followed by the combination between climate and season, with  $q$  value of 0.52. Due to the low  $q$  values of one single determinant during nighttime in the northern hemisphere, the enhancement using combinations of determinants is apparent, with the highest proportion of nonlinear enhancement pattern in the four categories.

During nighttime in the southern hemisphere, season is the one and only determinant with high  $q$  values in both conditions when taking account season itself or using its combinations.  $q$  value of season itself is 0.48, with a leading advantage of 0.13 compared with other determinants. Its combinations are of greater leading advantage in terms of  $q$  value comparing with other combinations, indicating that LULC improves the contribution of other determinants to  $\Delta T_g$  when combining with each other.

Due to the existence of season as the only dominant determinant during nighttime in the southern hemisphere, the  $q$  values of combinations during nighttime in the southern hemisphere are significantly higher than those in the northern hemisphere. Considering the overall  $q$  values in both northern and southern hemisphere, the combination between season and LULC or climate is the strongest among all the combinations during nighttime. In terms of the overall contribution, the combination between season and LULC presents the best performance among all the combinations in all four categories.

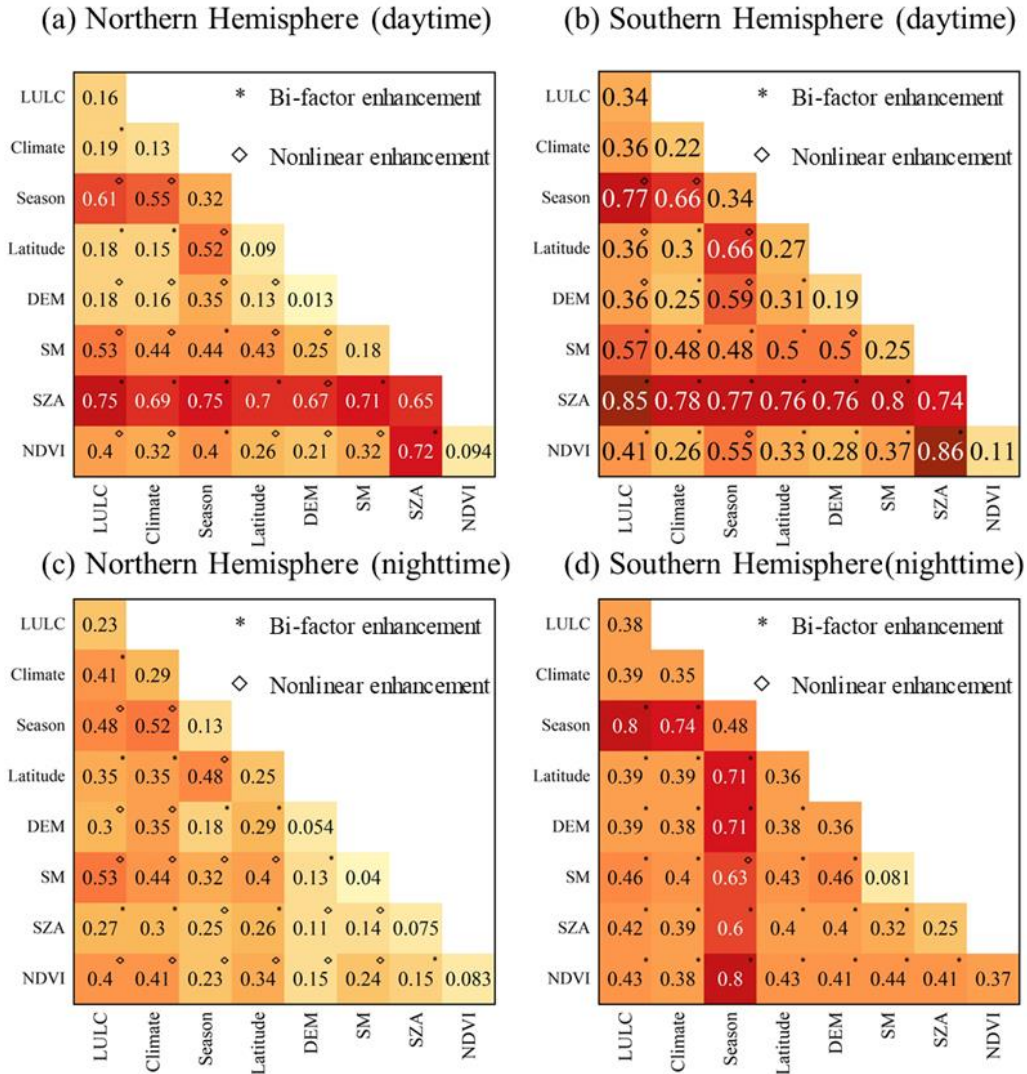


Fig 4.46 Interactions between determinants of spatial differentiation on  $\Delta T_g$ , (a) and (b) for daytime of northern/southern hemisphere, (c) and (d) for nighttime of northern/southern hemisphere, respectively.

### 4.3.3.3 Identification of sensitive areas of $\Delta T_g$ influenced by various factors

To further obtain the spatial difference in the response of  $\Delta T_g$  to various factors, risk detector was used to detect the sensitive areas of  $\Delta T_g$  to each determinant during daytime/nighttime in the northern and southern hemisphere. The results are shown in Fig 4.47-4.50 during daytime/nighttime in the northern and southern hemisphere, respectively. The values on the diagonal represent the average of the  $\Delta T_g$  for each factor. The significance of differences of  $\Delta T_g$  of two determinants are given as Y/N with Y representing significance ( $p < 0.05$  in Student's test) and N representing

insignificance ( $p > 0.05$ ). The higher proportion of Y, the larger the difference of  $\Delta T_g$  within various factor ranges is.

Fig 4.47 gives the  $\Delta T_g$  in terms of different determinants during daytime in the northern hemisphere.  $\Delta T_g$  of SNO area is 0.4, which is the lowest among the LULC types. Meanwhile, the significance of differences  $\Delta T_g$  between SNO and other LULC types is high, indicating that distribution of  $\Delta T_g$  of SNO is significantly different with other LULC types. ENF has the second lowest  $\Delta T_g$ , with significant difference with other six LULC types.  $\Delta T_g$  of GRA is the highest, with significant difference with other seven LULC types. Fig 4.47(b) indicates that  $\Delta T_g$  within different SM ranges do not vary significantly except for SM range [0.4, 0.5]. Fig 4.47 (c) indicates that there is significant difference of  $\Delta T_g$  in different seasons. There is a high significance between  $\Delta T_g$  in Spring and Autumn. Similarly, climate and latitude also have significant impact on  $\Delta T_g$  as shown in Fig 4.47 (d) and (f). As shown in Fig 4.47 (c),  $\Delta T_g$  in different DEM ranges is similar, and  $\Delta T_g$  in different DEM ranges correlate highly with each other. In terms of SZA as shown in Fig 4.47 (g),  $\Delta T_g$  and SZA has a negative correlation. And  $\Delta T_g$  in adjacent SZA ranges has significant differences, while  $\Delta T_g$  in distanced SZA ranges is correlated.  $\Delta T_g$  in different NDVI ranges show opposite pattern as those in SZA. In adjacent NDVI ranges,  $\Delta T_g$  is correlated with each other well.

Fig 4.48 illustrates the  $\Delta T_g$  in terms of different determinants during daytime in the southern hemisphere. Comparing to  $\Delta T_g$  in the northern hemisphere,  $\Delta T_g$  show similar pattern in terms of different determinants. SNO has the lowest value of  $\Delta T_g$  and the significance of difference with other LULC types is high as shown in Fig 4.48 (a).  $\Delta T_g$  gets higher with the increase of SM, and high SM ranges has significant difference on  $\Delta T_g$  comparing with low SM ranges (Fig 4.48 (b)). Inferring from Fig 4.48 (c), (d), (e), (f) and (g),  $\Delta T_g$  present down warding pattern with those determinants, and high significance of differences often appears when  $\Delta T_g$  is relatively low. The results indicate that during daytime, low  $\Delta T_g$  values often come with high difference significance.

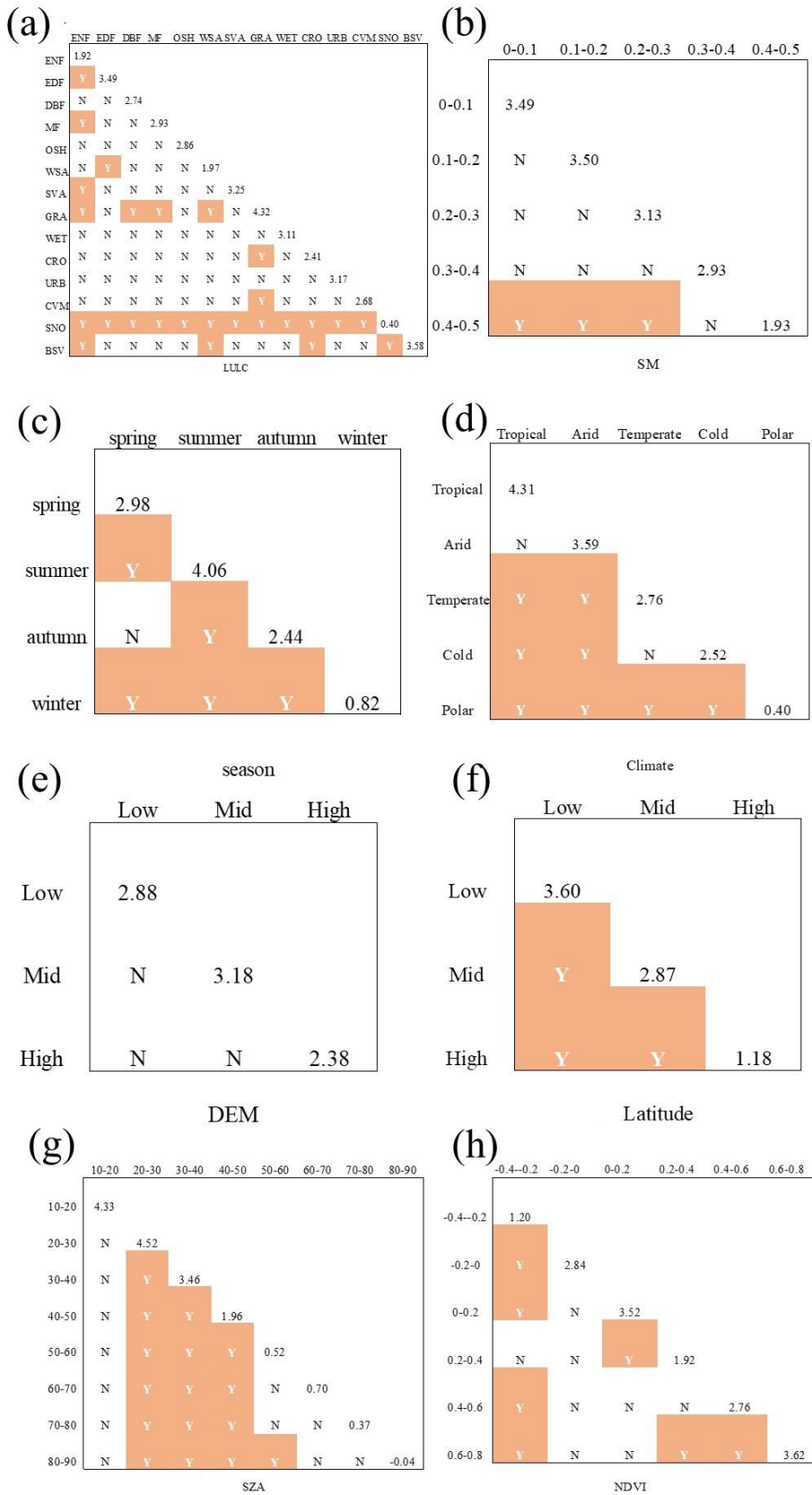


Fig 4.47 Mean values of  $\Delta T_g$  in different subregions for each determinant during daytime at northern hemisphere.

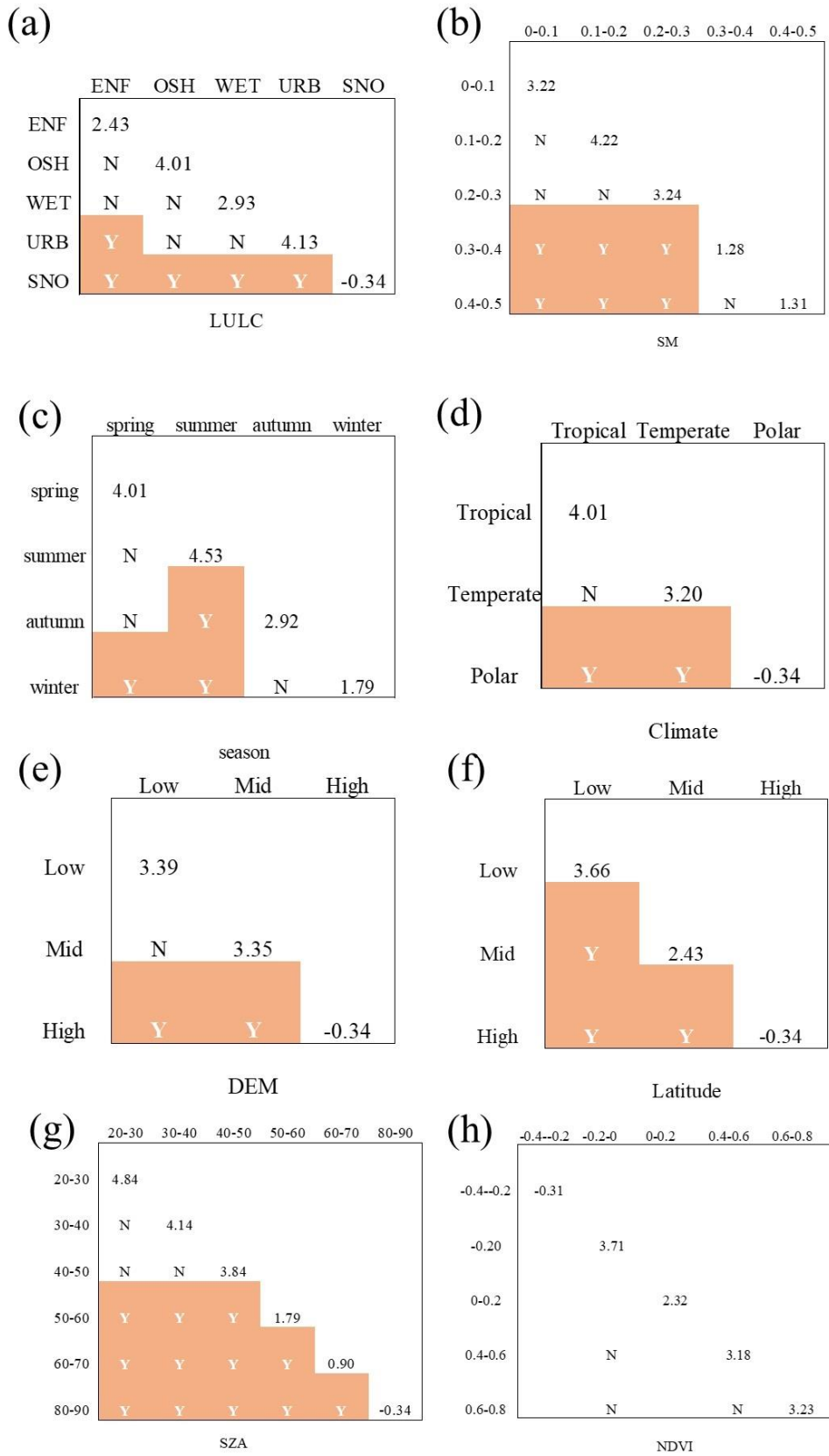


Fig 4.48 Mean values of  $\Delta T_g$  in different subregions for each determinant during daytime at southern hemisphere.

Fig 4.49 illustrates the  $\Delta T_g$  and its significance in terms of different determinants during nighttime in the northern hemisphere. As shown in Fig 4.49 (a),  $\Delta T_g$  of SNO has significant difference comparing with other LULC types, while  $\Delta T_g$  of CVM has the weakest significance of difference. The overall value of  $\Delta T_g$  during nighttime is lower than that during daytime, therefore, the gradient of  $\Delta T_g$  in different ranges of determinants is relatively small. The gradient of  $\Delta T_g$  with latitude during nighttime in northern hemisphere shows a downward trend.

Fig 4.50 demonstrates the  $\Delta T_g$  and its significance in terms of different determinants during nighttime in the southern hemisphere. There are only five available LULC types for analysis in the southern hemisphere. SNO, as always, has the smallest  $\Delta T_g$  and the most significant differences in  $\Delta T_g$ . ENF, due to its weak temporal variance, has the second smallest  $\Delta T_g$  (Fig 4.50 (a)).  $\Delta T_g$  does not always present a decreasing trend with the increasing of SM, SZA and NDVI (Fig 4.50 (b), (g) and (h)). In terms of  $\Delta T_g$  in different DEM, and latitude ranges as shown in Fig 4.50 (e) and (f),  $\Delta T_g$  in DEM and latitude different ranges show a descending gradient. Only in high DEM or latitude ranges,  $\Delta T_g$  has a strong significance of difference.

Chapter 4. Angular effects of surface brightness temperatures observed from SLSTR data

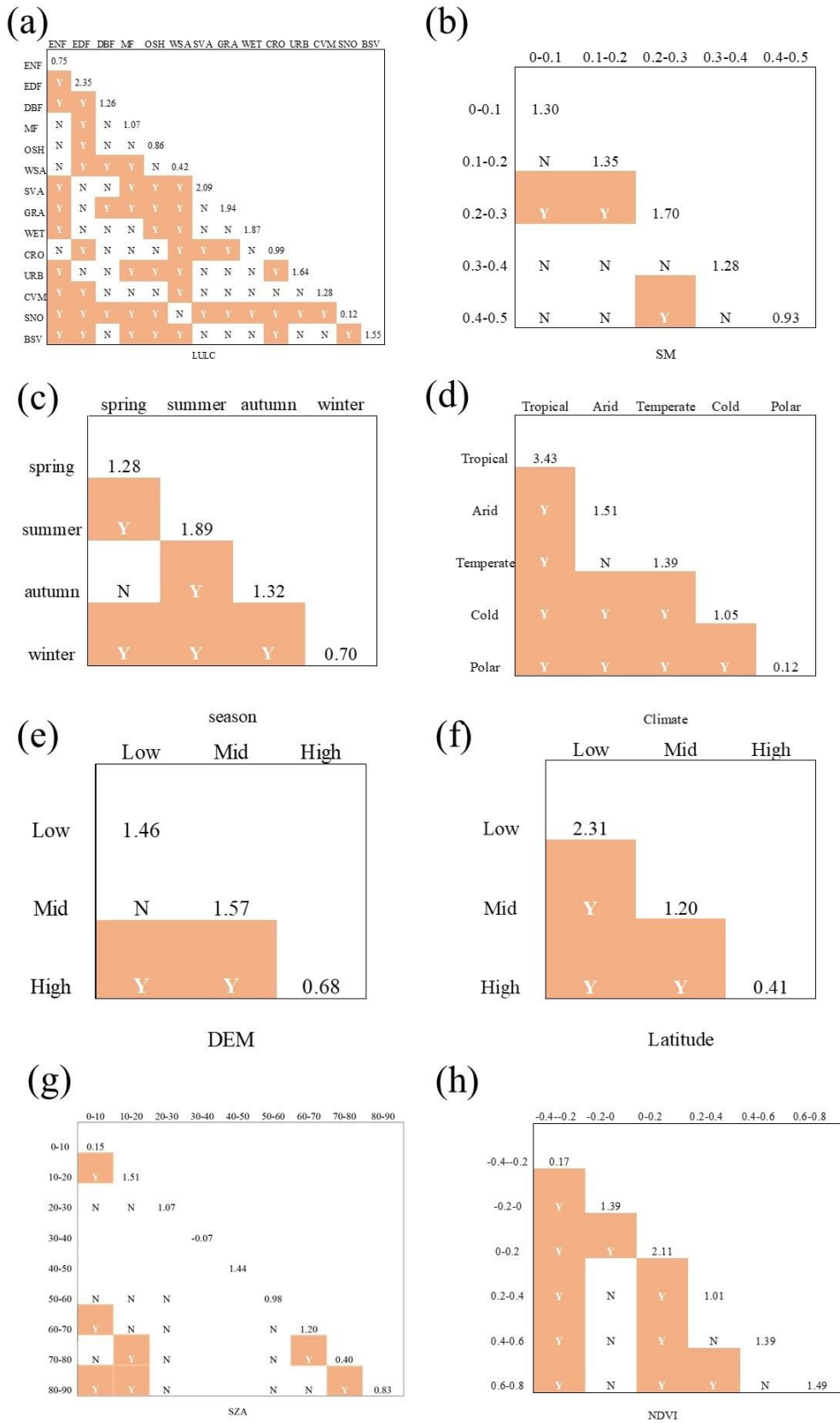


Fig 4.49 Mean values of  $\Delta T_g$  in different subregions for each determinant during nighttime at northern hemisphere.

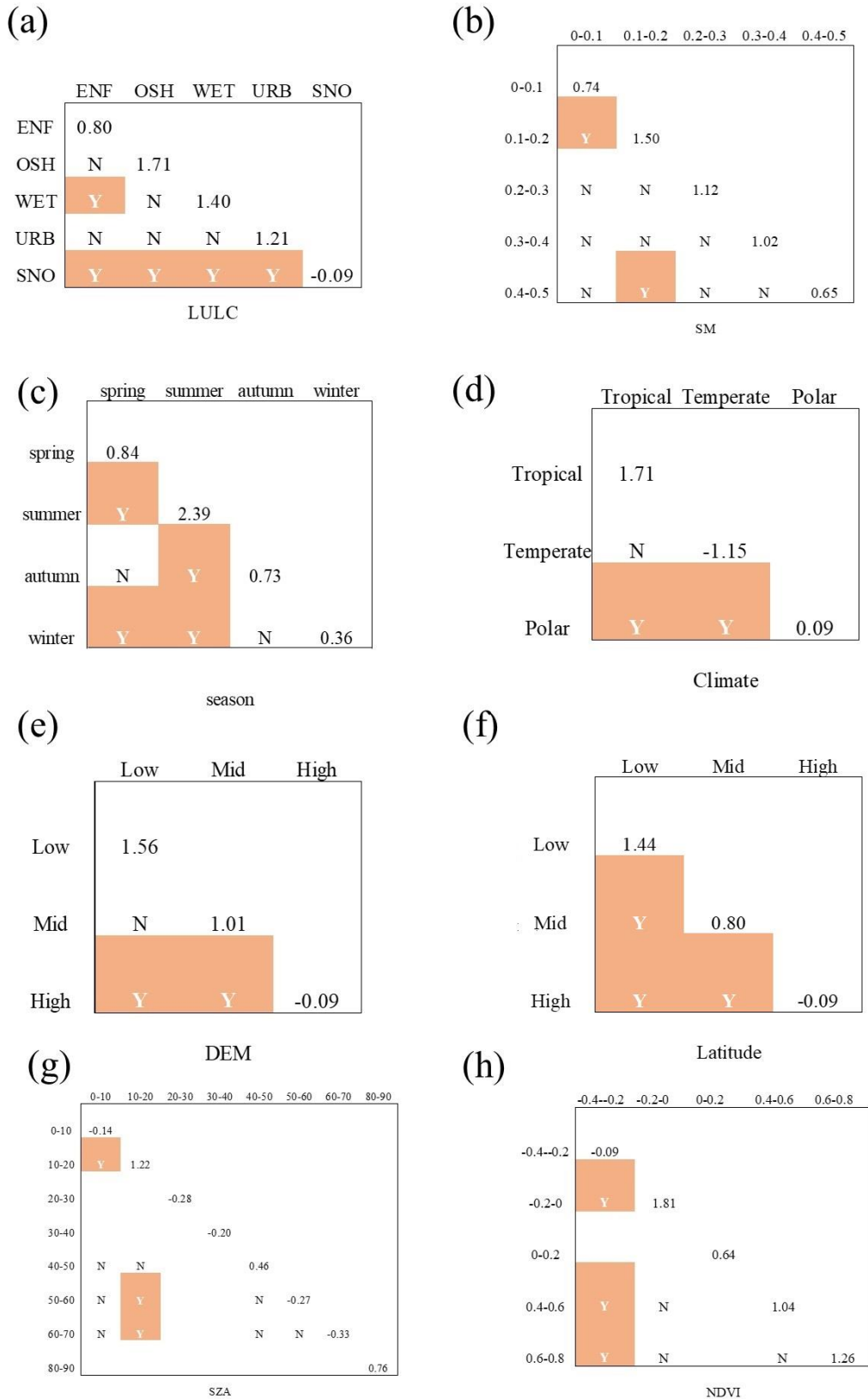


Fig 4.50 Mean values of  $\Delta T_g$  in different subregions for each determinant during nighttime at southern hemisphere.

## 4.4 Conclusion

This chapter uses MOD12Q1 and SRTM data to determine 42 sites located at 14 different land cover types. The differences between the surface brightness temperature observed at nadir and oblique are analyzed for different land cover types, seasons, latitudes, solar zenith angles and climates. GeoDetector is used to analyze the main driving factors of the angular effects. The specific conclusions are summarized as follows.

Overall, the difference in surface brightness temperature is between -3 and 9K. The maximum difference in surface brightness temperature occurs in URB. During the daytime, the mean  $\Delta T_g$  of various land cover types fluctuates monthly but tends to peak under hot, dry conditions and during the vegetation growing season. This is mainly due to solar radiation and the observed ratio of shadow and sunlight. At night, the mean  $\Delta T_g$  for most sites is concentrated between 0 and 2 K, with much less temporal variability than during the daytime. However, low-latitude sites such as EBF, SVA, and WET exhibit temporal fluctuation, with mean  $\Delta T_g$  reaching up to 6 K.

In the northern hemisphere, the mean  $\Delta T_g$  during the daytime in spring and summer is generally higher than that in autumn and winter. The seasonal change at night is not significant. In the southern hemisphere, the seasonal variation in daytime  $\Delta T_g$  is not as significant as in the northern hemisphere, with mean  $\Delta T_g$  similar in spring, summer, and autumn, and smallest in winter. The seasonal fluctuations of mean  $\Delta T_g$  during nighttime in the southern hemisphere are slightly more obvious, and the differences of mean  $\Delta T_g$  for most land cover types can reach 3 K in summer and winter during nighttime.

The mean  $\Delta T_g$  is higher in low-latitude regions than in high-latitude regions in general. The mean  $\Delta T_g$  values are similar between the northern and southern hemispheres in low-latitude areas. In mid-latitude regions, the mean  $\Delta T_g$  in the Southern Hemisphere is greater than in the northern hemisphere. In high-latitude regions, the mean  $\Delta T_g$  in the northern hemisphere is greater than in the southern hemisphere, as SNO is the only land cover type present at high latitudes in the southern hemisphere. The standard deviation of  $\Delta T_g$  is generally higher in the northern hemisphere than in the southern hemisphere.

In general, the mean values of  $\Delta T_g$  show a decreasing trend with increasing solar zenith angle. In particular, the decreasing trend of  $\Delta T_g$  is obvious when the solar zenith angle is between  $20^\circ$  and  $70^\circ$ . When the solar zenith angle is larger than  $70^\circ$ ,  $\Delta T_g$  remains stable, which indicates that the angular effects of surface brightness temperature is negligible when the solar zenith angle is large. In different latitude bands, the mean  $\Delta T_g$  values all show a decreasing trend with increasing solar zenith angle.

The mean  $\Delta T_g$  shows a decreasing trend in the order of tropical, arid, temperate, cold, and polar climates, both during the daytime and at nighttime. The mean  $\Delta T_g$  shows the widest variation in the arid climate and the smallest in the polar climate.

This study explored the contribution of each factor to  $\Delta T_g$  using GeoDetector. SZA is the main determinant, contributing the most to  $\Delta T_g$  during daytime in both the northern and southern hemispheres. Season is the second strongest determining factor, with a  $q$ -value of approximately 0.35. NDVI and DEM contribute the least to  $\Delta T_g$  during the daytime, possibly due to the selection of study areas with relatively uniform elevation. At night, no single determinant contributes more significantly than others, and the four determinants (LULC, climate, season, and latitude) have similar  $q$ -values. SM is the weakest determining factor for  $\Delta T_g$  at night in both hemispheres. Comparing the results of the northern and southern hemispheres, the contribution of each factor is greater in the southern hemisphere, indicating that  $\Delta T_g$  in the southern hemisphere is more sensitive to external influences.

There are two types of interaction between two determinants in this study, bi-factor enhancement and nonlinear enhancement. Nonlinear enhancement pattern is more common in the northern hemisphere, while bi-factor enhancement pattern is more common in the southern hemisphere. In both the northern and southern hemispheres, SZA showed the strongest contribution to  $\Delta T_g$  during the day as a single determinant, and combinations of SZA with other determinants also showed significant contributions. In the northern hemisphere at night, no single determinant shows a dominant contribution to  $\Delta T_g$ . Season is the dominant determinant at night in the southern hemisphere. In terms of overall contribution, the combination of season and LULC performs best in all cases.

Risk detector was used to detect the sensitive areas of  $\Delta T_g$  to each determinant during daytime/nighttime in the northern and southern hemisphere. The significance of differences of  $\Delta T_g$  between different ranges of determinants were also analyzed using

p value in Student's test. SNO, ENF and GRA show relatively distinctive significance rather than other LULC types during daytime. SNO is the only determinant showing significance during nighttime.  $\Delta T_g$  of SM range [0.4,0.5] is lower than other SM ranges, with significant difference with p value smaller than 0.05. The p values in different seasons, climate zones and latitude zones are small than 0.05 in most cases, indicating that differences of  $\Delta T_g$  are quite significant in different ranges of those properties.

## 5. Conclusions and prospectives

### 5.1 The conclusions

This study utilizes Sentinel-3A/SLSTR L1 products as the data source. Based on the two thermal infrared channels of SLSTR, the split-window algorithm was used to retrieve surface brightness temperature from both nadir ( $0^\circ$ ) and oblique ( $55^\circ$ ) observations. The accuracy of the split-window algorithm is validated using a simulation database. The study investigates whether there are differences in surface brightness temperature between the two angles, which land cover types exhibit these differences, and the potential causes for these discrepancies. The following conclusions were drawn from the analysis:

(1) The SLSTR brightness temperatures were retrieved using the SW algorithm at nadir and oblique views. The SW algorithm offers simplicity, high accuracy, and effective atmospheric correction capabilities. The coefficients of  $0^\circ$  and  $55^\circ$  observations were fitted using the least squares method. The accuracy of SW algorithm was validated using a simulation database. The RMSE is 0.74 K at nadir observations and 1.23 K at oblique observations. When atmospheric water vapor content is high, the algorithm may produce larger errors. The total uncertainty in surface brightness temperature is composed of contributions from the surface brightness temperature retrieval model and the TOA brightness temperature. The uncertainty caused by TOA brightness temperature is 1.44 K at nadir observations and 1.14 K at oblique observations. And the total uncertainties of nadir and oblique observations are 1.62 K and 1.68 K, respectively.

(2) The surface brightness temperature at  $0^\circ$  and  $55^\circ$  was compared across 42 sites across 14 different land cover types (ENF, EBF, DBF, MF, OSH, WSA, SVA, GRA, WET, CRO, URB, CVM, SNO, BSV). Results show that, regardless of day or night and across both northern and southern hemispheres, the differences of surface brightness temperature range from -3 K to 9 K. The angular effects on surface brightness temperature are generally present over land surfaces. Seasonal variations in the mean  $\Delta T_g$  are pronounced during daytime, with the largest difference observed in

summer (up to 6 K) and the smallest difference in winter, ranging from 0 K to 4 K. At nighttime, the mean  $\Delta T_g$  of most sites are smaller and do not vary with the seasons, indicating that the angular effect on SBT is less significant at nighttime. The mean  $\Delta T_g$  shows a decreasing trend with increasing latitude and solar zenith angle. Besides, the mean  $\Delta T_g$  exhibits the greatest variation in arid climate and the smallest variation in polar climate.

(3) The main driving factors of the angular effects of surface brightness temperature were analyzed by three detectors of GeoDetector, including factor detector, interaction detector, and risk detector. This study selected LULC, season, latitude, SZA, climate, NDVI, DEM and SM as determinants for analysis. During daytime, SZA contribute the most to  $\Delta T_g$  in both hemispheres. During nighttime, no single determining factor contributes more significantly than others. There are two types of interaction between two determinants increasing the contribution to  $\Delta T_g$  in this study, bi-factor enhancement and nonlinear enhancement. Nonlinear enhancement is more prevalent in the northern hemisphere, while bi-factor enhancement is more prevalent in the southern hemisphere. The results of risk detector show that the significance of differences of  $\Delta T_g$  between different ranges of seasons, climate zones, and latitude zones is high, with p values smaller than 0.05. SNO, ENF and GRA are the LULC types with highest significance of differences with other LULC types.

The above research results show that the surface brightness temperatures have angular effects observed from Sentinel-3A/SLSTR Data at 1 km scale. The angular effects of the surface brightness temperatures are affected by many factors and have regional differences.

## 5.2 Prospective

In this dissertation research, we used a split-window algorithm to retrieve land surface brightness temperature from two viewing angles: nadir view and oblique view. The differences of surface brightness temperatures between different viewing angles were analyzed in terms of different seasons, land cover types, latitudes, climates and SZA. The influencing factors of angular effect and their correlations were further discussed.

However, there are several remaining works to be done in future research. Regarding the algorithms, a classic split-window algorithm was used in this study to

retrieve surface brightness temperature. The coefficients of the split-window algorithm are uniform throughout the entire water vapor range. A more advanced split-window algorithm with segmented coefficients for different water vapor may be helpful for more accurate retrieval of surface brightness temperature. TIR-based algorithms often have high error and bias over barren/sparsely vegetated surfaces due to the special physical and radiative parameters. Sometimes the negative deviation can reach several degrees during daytime. To promote the accuracy when estimating surface brightness temperature under these conditions, a particular set of coefficients may be beneficial.

The validation of dual-angle surface brightness temperature is challenging. Normally, LST can be evaluated using in-situ measurements collected from longwave radiometers. But those radiometers are often mounted for nadir view. It is difficult to obtain in-situ measurements from an oblique view. Therefore, the establishment of in-situ sites with dual-angle observations is urgently needed. R-based validation is another commonly used method to evaluate the accuracy of LST. Probably it is applicable to validate dual-angle observation in the future. Discrete Anisotropic Radiative Transfer (DART) model is a complex three-dimensional radiative transfer model that can build natural surface through geomorphic data, simulating the radiative transfer process between the surface and atmosphere in TIR bands. It plays an important role in analyzing the effects of mixed pixels and terrain undulations on radiation. It is also applicable to simulate radiation from nadir and oblique view, the comparison between simulated and observed surface brightness temperature may also help improve the understanding of angular effects over different terrains.

In terms of the contributing factors of the differences of surface brightness temperature between nadir and oblique view ( $\Delta T_g$ ), the impact of topographic factors was excluded from analysis. Further consideration of how slope and aspect factors interact with angular effect is needed. Data integrity also affects the completeness and reliability of analysis. There are plenty of missing data in several land cover types, e.g., WSA and SNO, leading to discontinuous annual curve of  $\Delta T_g$ . The research is also based on data collected in one year period, lacking long-term data collection. Therefore, the patterns of  $\Delta T_g$  may need further validation to reach a more robust conclusion. Though a cloud filtering method was applied to Sentinel-3 SLSTR data using quality control flag, the existence of residual cloud or cloud shadow pixels is inevitable. A

more comprehensive cloud filtering method, e.g., Fmask method, may be beneficial to the selection of cloud-free pixels from massive original data.

## Reference

- Adderley, C., Christen, A., and Voogt, J. A. (2015). The effect of radiometer placement and view on inferred directional and hemispheric radiometric temperatures of an urban canopy. *Atmospheric Measurement Techniques*, 8(7), 2699-2714.
- Anderson, M. C., Allen, R. G., Morse, A., and Kustas, W. P. (2012). Use of landsat thermal imagery in monitoring evapotranspiration and managing water resources. *Remote Sensing of Environment*, 122, 50-65.
- Baldrige, A. M., Hook, S. J., Grove, C. I., and Rivera, G. (2009). The aster spectral library version 2.0. *Remote Sensing of Environment*, 113(4), 711-715.
- Beck, H. E., Zimmermann, N. E., McVicar, T. R., Vergopolan, N., Berg, A., and Wood, E. F. (2018). Present and future koppen-geiger climate classification maps at 1-km resolution. *Scientific Data*, 5(1), 180214.
- Becker, F., and Li, Z.-L. (1990). Temperature-independent spectral indices in thermal infrared bands. *Remote Sensing of Environment*, 32(1), 17-33.
- Becker, F., and Li, Z.-L. (2007). Towards a local split window method over land surfaces. *International Journal of Remote Sensing*, 11(3), 369-393.
- Berk, A., Anderson, G., Acharya, P., and Shettle, E. J. I., Burlington, MA. (2011). *Modtran 5.2. 2 user's manual spectral sciences*. 69.
- Bian, Z., Roujean, J.-L., Cao, B., Du, Y., Li, H., Gamet, P., Fang, J., Xiao, Q., and Liu, Q. (2021). Modeling the directional anisotropy of fine-scale tir emissions over tree and crop canopies based on uav measurements. *Remote Sensing of Environment*, 252, 112150.
- Bright, R. M., Davin, E., O'Halloran, T., Pongratz, J., Zhao, K., and Cescatti, A. (2017). Local temperature response to land cover and management change driven by non-radiative processes. *Nature Climate Change*, 7(4), 296-302.
- Cao, B., Bian, Z., Xiao, Q., Fang, J., Huang, H., Bai, J., Fan, W., Du, Y., Li, H., and Liu, Q. (2018, 22-27 July 2018). Evaluation the spatial-temporal average method in the multi-angle information extraction based on near surface observation sensors. Paper presented at the IGARSS 2018 - 2018 IEEE International Geoscience and Remote Sensing Symposium.
- Cao, B., Liu, Q., Du, Y., Roujean, J.-L., Gastellu-Etchegorry, J.-P., Trigo, I. F., Zhan, W., Yu, Y., Cheng, J., Jacob, F., Lagouarde, J.-P., Bian, Z., Li, H., Hu, T., and Xiao, Q. (2019). A review of earth surface thermal radiation directionality observing and modeling: Historical development, current status and perspectives. *Remote Sensing of Environment*, 232, null.
- Chedin, A., and Scott, N. A. (1985). Initialization of the radiative transfer equation inversion problem from a pattern recognition type approach: Application to the satellites of the tiros-n series. *Advances in Remote Sensing Retrieval Methods*, 495-515.
- Chedin, A., Scott, N. A., and Berroir, A. (1982). A single-channel, double-viewing angle method for sea surface temperature determination from coincident meteosat and tiros-n radiometric measurements. *Journal of Applied Meteorology and Climatology*, 21(4), 613-618.
- Chedin, A., Scott, N. A., Claud, C., Bonnet, B., Escobar, J., Dardaillon, S., Cheruy, F., and Husson, N. (1994). Global scale observation of the earth for climate studies. *Advances in Space Research*, 14(1), 155-159.
- Chebouni, A., Nouvellon, Y., Kerr, Y. H., Moran, M. S., Watts, C., Prevot, L., Goodrich, D. C., and Rambal, S. (2001). Directional effect on radiative surface

- temperature measurements over a semiarid grassland site. *Remote Sensing of Environment*, 76(3), 360-372.
- Chen, X., Peng, J., Song, Z., Zheng, Y., and Zhang, B. (2022). Monitoring persistent coal fire using landsat time series data from 1986 to 2020. *IEEE Transactions on Geoscience and Remote Sensing*, 60, 1-16.
- Chen, Y., Duan, S.-B., Ren, H., Labeled, J., and Li, Z.-L. (2017). Algorithm development for land surface temperature retrieval: Application to chinese gaofen-5 data. *Remote Sensing*, 9(2).
- Coll, C., and Caselles, V. (1997). A split - window algorithm for land surface temperature from advanced very high resolution radiometer data: Validation and algorithm comparison. *Journal of Geophysical Research: Atmospheres*, 102(D14), 16697-16713.
- Coll, C., Caselles, V., Sobrino, J. A., and Valor, E. (1994). On the atmospheric dependence of the split-window equation for land surface temperature. *International Journal of Remote Sensing*, 15(1), 105-122.
- Coll, C., Caselles, V., Sobrino, J. A., and Valor, E. (2007). On the atmospheric dependence of the split-window equation for land surface temperature. *International Journal of Remote Sensing*, 15(1), 105-122.
- Coll, C., Galve, J. M., Niclòs, R., Valor, E., and Barberà, M. J. (2019). Angular variations of brightness surface temperatures derived from dual-view measurements of the advanced along-track scanning radiometer using a new single band atmospheric correction method. *Remote Sensing of Environment*, 223, 274-290.
- Dash, P., Göttsche, F. M., Olesen, F. S., and Fischer, H. (2010). Land surface temperature and emissivity estimation from passive sensor data: Theory and practice-current trends. *International Journal of Remote Sensing*, 23(13), 2563-2594.
- Dorigo, W., Preimesberger, W., Stradiotti, P., Kidd, R., van der Schalie, R., van der Vliet, M., Rodriguez-Fernandez, N., Madelon, R., and Baghdadi, N. (2023). Esa climate change initiative plus - soil moisture algorithm theoretical baseline document (atbd) supporting product version 08.1 (version 1.1). Zenodo.
- Duan, S.-B., Li, Z.-L., Wang, C., Zhang, S., Tang, B.-H., Leng, P., and Gao, M.-F. (2018). Land-surface temperature retrieval from landsat 8 single-channel thermal infrared data in combination with ncep reanalysis data and aster ged product. *International Journal of Remote Sensing*, 40(5-6), 1763-1778.
- Friedl, M. A. (2002). Forward and inverse modeling of land surface energy balance using surface temperature measurements. *Remote Sensing of Environment*, 79(2-3), 344-354.
- Friedl, M. A., Sulla-Menashe, D., Tan, B., Schneider, A., Ramankutty, N., Sibley, A., and Huang, X. (2010). Modis collection 5 global land cover: Algorithm refinements and characterization of new datasets. *Remote Sensing of Environment*, 114(1), 168-182.
- Fuchs, M., Kanemasu, E. T., Kerr, J. P., and Tanner, C. B. (1967). Effect of viewing angle on canopy temperature measurements with infrared thermometers. *Agronomy Journal*, 59(5), 494-496.
- Garcia-Santos, V., Cuxart, J., Jimenez, M. A., Martinez-Villagrasa, D., Simo, G., Picos, R., and Caselles, V. (2019). Study of temperature heterogeneities at sub-kilometric scales and influence on surface-atmosphere energy interactions. *IEEE Transactions on Geoscience and Remote Sensing*, 57(2), 640-654.

- Gillespie, A., Rokugawa, S., Matsunaga, T., Cothern, J. S., Hook, S., and Kahle, A. B. (1998). A temperature and emissivity separation algorithm for advanced spaceborne thermal emission and reflection radiometer (aster) images. *IEEE Transactions on Geoscience and Remote Sensing*, 36(4), 1113-1126.
- He, X., Xu, T., Bateni, S. M., Ek, M., Liu, S., and Chen, F. (2020). Mapping regional evapotranspiration in cloudy skies via variational assimilation of all-weather land surface temperature observations. *Journal of Hydrology*, 585.
- Hu, L., Monaghan, A., Voogt, J. A., and Barlage, M. (2016). A first satellite-based observational assessment of urban thermal anisotropy. *Remote Sensing of Environment*, 181, 111-121.
- Hu, T., Renzullo, L. J., van Dijk, A. I. J. M., He, J., Tian, S., Xu, Z., Zhou, J., Liu, T., and Liu, Q. (2020). Monitoring agricultural drought in australia using mtsat-2 land surface temperature retrievals. *Remote Sensing of Environment*, 236, 111419.
- Hu, X., Ren, H., Tansey, K., Zheng, Y., Ghent, D., Liu, X., and Yan, L. (2019). Agricultural drought monitoring using european space agency sentinel 3a land surface temperature and normalized difference vegetation index imageries. *Agricultural and Forest Meteorology*, 279.
- Hulley, G. C., and Hook, S. J. (2011). Generating consistent land surface temperature and emissivity products between aster and modis data for earth science research. *IEEE Transactions on Geoscience and Remote Sensing*, 49(4), 1304-1315.
- Hulley, G. C., Hughes, C. G., and Hook, S. J. (2012). Quantifying uncertainties in land surface temperature and emissivity retrievals from aster and modis thermal infrared data. *Journal of Geophysical Research: Atmospheres*, 117(D23).
- Islam, T., Hulley, G. C., Malakar, N. K., Radocinski, R. G., Guillevic, P. C., and Hook, S. J. (2017). A physics-based algorithm for the simultaneous retrieval of land surface temperature and emissivity from viirs thermal infrared data. *IEEE Transactions on Geoscience and Remote Sensing*, 55(1), 563-576.
- Jiang, L., Zhan, W., Tu, L., Dong, P., Wang, S., Li, L., Wang, C., and Wang, C. (2022). Diurnal variations in directional brightness temperature over urban areas through a multi-angle uav experiment. *Building and Environment*, 222, 109408.
- Jimenez-Munoz, J. C., Cristobal, J., Sobrino, J. A., Soria, G., Ninyerola, M., Pons, X., and Pons, X. (2009). Revision of the single-channel algorithm for land surface temperature retrieval from landsat thermal-infrared data. *IEEE Transactions on Geoscience and Remote Sensing*, 47(1), 339-349.
- Jimenez-Munoz, J. C., Sobrino, J. A., Mattar, C., Hulley, G., and Gottsche, F.-M. (2014). Temperature and emissivity separation from msg/seviri data. *IEEE Transactions on Geoscience and Remote Sensing*, 52(9), 5937-5951.
- Jiménez - Muñoz, J. C., and Sobrino, J. A. (2003). A generalized single - channel method for retrieving land surface temperature from remote sensing data. *Journal of Geophysical Research: Atmospheres*, 108(D22), 9.
- Jiménez - Muñoz, J. C., and Sobrino, J. A. (2007). Error sources on the land surface temperature retrieved from thermal infrared single channel remote sensing data. *International Journal of Remote Sensing*, 27(5), 999-1014.
- Kalma, J. D., McVicar, T. R., and McCabe, M. F. (2008). Estimating land surface evaporation: A review of methods using remotely sensed surface temperature data. *Surveys in Geophysics*, 29(4-5), 421-469.
- Keenan, T. F., and Riley, W. J. (2018). Greening of the land surface in the world's cold regions consistent with recent warming. *Nat Clim Chang*, 8(9), 825-828.

## Reference

- Kimes, D. S. (1980). Effects of vegetation canopy structure on remotely sensed canopy temperatures. *Remote Sensing of Environment*, 10(3), 165-174.
- Kimes, D. S. (1981). Remote sensing of temperature profiles in vegetation canopies using multiple view angles and inversion techniques. *IEEE Transactions on Geoscience and Remote Sensing*, GE-19(2), 85-90.
- Kimes, D. S., and Kirchner, J. A. (2007). Directional radiometric measurements of row-crop temperatures. *International Journal of Remote Sensing*, 4(2), 299-311.
- Lagouarde, J.-P., Ballans, H., Moreau, P., Guyon, D., and Coraboeuf, D. (2000). Experimental study of brightness surface temperature angular variations of maritime pine (*pinus pinaster*) stands. *Remote Sensing of Environment*, 72(1), 17-34.
- Lagouarde, J.-P., Dayau, S., Moreau, P., and Guyon, D. (2014). Directional anisotropy of brightness surface temperature over vineyards: Case study over the medoc region (sw france). *IEEE Geoscience and Remote Sensing Letters*, 11(2), 574-578.
- Lagouarde, J. P., Hénon, A., Kurz, B., Moreau, P., Irvine, M., Voogt, J., and Mestayer, P. (2010). Modelling daytime thermal infrared directional anisotropy over toulouse city centre. *Remote Sensing of Environment*, 114(1), 87-105.
- Lagouarde, J. P., and Irvine, M. (2008). Directional anisotropy in thermal infrared measurements over toulouse city centre during the capitoul measurement campaigns: First results. *Meteorology and Atmospheric Physics*, 102(3-4), 173-185.
- Lagouarde, J. P., Kerr, Y. H., and Brunet, Y. (1995). An experimental study of angular effects on surface temperature for various plant canopies and bare soils. *Agricultural and Forest Meteorology*, 77(3-4), 167-190.
- Li, H., Li, R., Tu, H., Cao, B., Liu, F., Bian, Z., Hu, T., Du, Y., Sun, L., and Liu, Q. (2023). An operational split-window algorithm for generating long-term land surface temperature products from chinese fengyun-3 series satellite data. *IEEE Transactions on Geoscience and Remote Sensing*, 61, 1-14.
- Li, J., Li, Z.-L., Wu, H., and You, N. (2022). Trend, seasonality, and abrupt change detection method for land surface temperature time-series analysis: Evaluation and improvement. *Remote Sensing of Environment*, 280.
- Li, R., Li, H., Hu, T., Bian, Z., Liu, F., Cao, B., Du, Y., Sun, L., and Liu, Q. (2023). Land surface temperature retrieval from sentinel-3a slstr data: Comparison among split-window, dual-window, three-channel, and dual-angle algorithms. *IEEE Transactions on Geoscience and Remote Sensing*, 61, 1-14.
- Li, Y., Li, Z.-L., Wu, H., Zhou, C., Liu, X., Leng, P., Yang, P., Wu, W., Tang, R., Shang, G. F., and Ma, L. (2023). Biophysical impacts of earth greening can substantially mitigate regional land surface temperature warming. *Nature Communications*, 14(1), 121.
- Li, Z.-L., Tang, B.-H., Wu, H., Ren, H., Yan, G., Wan, Z., Trigo, I. F., and Sobrino, J. A. (2013). Satellite-derived land surface temperature: Current status and perspectives. *Remote Sensing of Environment*, 131, 14-37.
- Li, Z. L., Wu, H., Duan, S. B., Zhao, W., Ren, H., Liu, X., Leng, P., Tang, R., Ye, X., Zhu, J., Sun, Y., Si, M., Liu, M., Li, J., Zhang, X., Shang, G., Tang, B. H., Yan, G., and Zhou, C. (2023). Satellite remote sensing of global land surface temperature: Definition, methods, products, and applications. *Reviews of Geophysics*, 61(1), null.
- Liu, M., Zhu, Y., Yang, H., Pu, R., Qiu, C., Zhao, F., Han, S., Xu, W., Meng, Y., Long, H., and Yang, G. (2022). Prediction of apple first flowering date using daily

## Reference

- land surface temperature spatio-temporal reconstruction and machine learning. *Computers and Electronics in Agriculture*, 202, 107366.
- Liu, Q., Yan, C., Xiao, Q., Yan, G., and Fang, L. (2012). Separating vegetation and soil temperature using airborne multiangular remote sensing image data. *International Journal of Applied Earth Observation and Geoinformation*, 17, 66-75.
- Malakar, N. K., and Hulley, G. C. (2016). A water vapor scaling model for improved land surface temperature and emissivity separation of modis thermal infrared data. *Remote Sensing of Environment*, 182, 252-264.
- Malakar, N. K., Hulley, G. C., Hook, S. J., Laraby, K., Cook, M., and Schott, J. R. (2018). An operational land surface temperature product for landsat thermal data: Methodology and validation. *IEEE Transactions on Geoscience and Remote Sensing*, 56(10), 5717-5735.
- Masoudi, M., and Tan, P. Y. (2019). Multi-year comparison of the effects of spatial pattern of urban green spaces on urban land surface temperature. *Landscape and Urban Planning*, 184, 44-58.
- Mcmillin, L. M. (1975). Estimation of sea surface temperatures from two infrared window measurements with different absorption. *Journal of Geophysical Research*, 80(36), 5113-5117.
- Meerdink, S. K., Hook, S. J., Roberts, D. A., and Abbott, E. A. (2019). The ecostress spectral library version 1.0. *Remote Sensing of Environment*, 230, 111196.
- Morrison, W., Grimmond, S., and Kotthaus, S. (2023). Simulating satellite urban land surface temperatures: Sensitivity to sensor view angle and assumed landscape complexity. *Remote Sensing of Environment*, 293, 113579.
- Paw U, K. T., Ustin, S. L., and Zhang, C.-A. (1989). Anisotropy of thermal infrared exitance in sunflower canopies. *Agricultural and Forest Meteorology*, 48(1-2), 45-58.
- Peng, J., Ma, J., Liu, Q., Liu, Y., Hu, Y., Li, Y., and Yue, Y. (2018). Spatial-temporal change of land surface temperature across 285 cities in china: An urban-rural contrast perspective. *Science of The Total Environment*, 635, 487-497.
- Prata, A. J. (2012). Land surface temperatures derived from the advanced very high resolution radiometer and the along - track scanning radiometer: 1. Theory. *Journal of Geophysical Research: Atmospheres*, 98(D9), 16689-16702.
- Price, J. C. (2012). Land surface temperature measurements from the split window channels of the noaa 7 advanced very high resolution radiometer. *Journal of Geophysical Research: Atmospheres*, 89(D5), 7231-7237.
- Qin, Z., Dall'Olmo, G., Karnieli, A., and Berliner, P. (2001). Derivation of split window algorithm and its sensitivity analysis for retrieving land surface temperature from noaa - advanced very high resolution radiometer data. *Journal of Geophysical Research: Atmospheres*, 106(D19), 22655-22670.
- Qin, Z., Karnieli, A., and Berliner, P. (2010). A mono-window algorithm for retrieving land surface temperature from landsat tm data and its application to the israel-egypt border region. *International Journal of Remote Sensing*, 22(18), 3719-3746.
- Rasmussen, M. O., Gottsche, F.-M., Olesen, F.-S., and Sandholt, I. (2011). Directional effects on land surface temperature estimation from meteosat second generation for savanna landscapes. *IEEE Transactions on Geoscience and Remote Sensing*, 49(11), 4458-4468.

## Reference

- Ren, H., Yan, G., Chen, L., and Li, Z.-L. (2011). Angular effect of modis emissivity products and its application to the split-window algorithm. *ISPRS Journal of Photogrammetry and Remote Sensing*, 66(4), 498-507.
- Ru, C., Duan, S.-B., Jiang, X.-G., Li, Z.-L., Huang, C., and Liu, M. (2023). An extended sw-tes algorithm for land surface temperature and emissivity retrieval from ecostress thermal infrared data over urban areas. *Remote Sensing of Environment*, 290, 113544.
- Ru, C., Duan, S.-B., Jiang, X.-G., Li, Z.-L., Jiang, Y., Ren, H., Leng, P., and Gao, M. (2022). Land surface temperature retrieval from landsat 8 thermal infrared data over urban areas considering geometry effect: Method and application. *IEEE Transactions on Geoscience and Remote Sensing*, 60, 1-16.
- Sabol, J. D. E., Gillespie, A. R., Abbott, E., and Yamada, G. (2009). Field validation of the aster temperature–emissivity separation algorithm. *Remote Sensing of Environment*, 113(11), 2328-2344.
- Shi, B., Tu, L., Jiang, L., Zhang, J., and Geng, J. (2023). A quantitative study of a directional heat island in hefei, china based on multi-source data. *Sensors*, 23(6).
- Sobrino, J. A., and Jiménez-Muñoz, J. C. (2005). Land surface temperature retrieval from thermal infrared data: An assessment in the context of the surface processes and ecosystem changes trough response analysis (spectra) mission. *Journal of Geophysical Research Atmospheres*, 110(D16), -.
- Sobrino, J. A., Sòria, G., and Prata, A. J. (2004). Surface temperature retrieval from along track scanning radiometer 2 data: Algorithms and validation. *Journal of Geophysical Research: Atmospheres*, 109(D11).
- Sobrino, J. A., Zhao-Liang, L., Stoll, M. P., and Becker, F. (1994). Improvements in the split-window technique for land surface temperature determination. *IEEE Transactions on Geoscience and Remote Sensing*, 32(2), 243-253.
- Tang, R., Li, Z.-L., Liu, M., Jiang, Y., and Peng, Z. (2022). A moisture-based triangle approach for estimating surface evaporative fraction with time-series of remotely sensed data. *Remote Sensing of Environment*, 280, 113212.
- Voogt, J. A. (2008). Assessment of an urban sensor view model for thermal anisotropy. *Remote Sensing of Environment*, 112(2), 482-495.
- Voogt, J. A., and Oke, T. R. (2003). Thermal remote sensing of urban climates. *Remote Sensing of Environment*, 86(3), 370-384.
- Wang, C., Duan, S.-B., Zhang, X., Wu, H., Gao, M.-F., and Leng, P. (2018). An alternative split-window algorithm for retrieving land surface temperature from visible infrared imaging radiometer suite data. *International Journal of Remote Sensing*, 40(5-6), 1640-1654.
- Wang, D., Chen, Y., Hu, L., Voogt, J. A., Gastellu-Etchegorry, J.-P., and Krayenhoff, E. S. (2021). Modeling the angular effect of modis lst in urban areas: A case study of toulouse, france. *Remote Sensing of Environment*, 257, 112361.
- Wang, J.-F., and Hu, Y. (2012). Environmental health risk detection with geogdetector. *Environmental Modelling & Software*, 33, 114-115.
- Wang, J.-F., Zhang, T.-L., and Fu, B.-J. (2016). A measure of spatial stratified heterogeneity. *Ecological Indicators*, 67, 250-256.
- Wang, J. F., Li, X. H., Christakos, G., Liao, Y. L., Zhang, T., Gu, X., and Zheng, X. Y. (2010). Geographical detectors - based health risk assessment and its application in the neural tube defects study of the heshun region, china. *International Journal of Geographical Information Science*, 24(1), 107-127.

## Reference

- Yan, G., Ren, H., Hu, R., Yan, K., and Zhang, W. (2012, 22-27 July 2012). A portable multi-angle observation system. Paper presented at the 2012 IEEE International Geoscience and Remote Sensing Symposium.
- Zhang, S., Duan, S.-B., Li, Z.-L., Huang, C., Wu, H., Han, X.-J., Leng, P., and Gao, M. (2019). Improvement of split-window algorithm for land surface temperature retrieval from sentinel-3A SLSTR data over barren surfaces using aster ged product. *Remote Sensing*, 11(24).
- Zhao-Liang, L., Stoll, M. P., Renhua, Z., Li, J., and Zhongbo, S. (2001). On the separate retrieval of soil and vegetation temperatures from atsr data. *Science in China Series D: Earth Sciences*, 44(2), 97-111.
- Zheng, X., Li, Z.-L., Nerry, F., and Zhang, X. (2019). A new thermal infrared channel configuration for accurate land surface temperature retrieval from satellite data. *Remote Sensing of Environment*, 231, 111216.
- Zheng, Y., Ren, H., Guo, J., Ghent, D., Tansey, K., Hu, X., Nie, J., and Chen, S. (2019). Land surface temperature retrieval from sentinel-3A sea and land surface temperature radiometer, using a split-window algorithm. *Remote Sensing*, 11(6).
- Zhengming, W., and Dozier, J. (1996). A generalized split-window algorithm for retrieving land-surface temperature from space. *IEEE Transactions on Geoscience and Remote Sensing*, 34(4), 892-905.
- Zhengming, W., and Zhao-Liang, L. (1997). A physics-based algorithm for retrieving land-surface emissivity and temperature from eos/modis data. *IEEE Transactions on Geoscience and Remote Sensing*, 35(4), 980-996.
- Zhou, D., Xiao, J., Bonafoni, S., Berger, C., Deilami, K., Zhou, Y., Frolking, S., Yao, R., Qiao, Z., and Sobrino, J. A. (2018). Satellite remote sensing of surface urban heat islands: Progress, challenges, and perspectives. *Remote Sensing*, 11(1), 48.
- Zhu, X., Duan, S.-B., Li, Z.-L., Zhao, W., Wu, H., Leng, P., Gao, M., and Zhou, X. (2021). Retrieval of land surface temperature with topographic effect correction from landsat 8 thermal infrared data in mountainous areas. *IEEE Transactions on Geoscience and Remote Sensing*, 59(8), 6674-6687.

# Shuting ZHANG

## Angular Effects of Surface Brightness Temperature Observed from Sentinel-3A/SLSTR Data

### Résumé

Ce travail de thèse utilise les données TIR de SLSTR comme source principale pour extraire la température de brillance de la surface (SBT) en appliquant l'algorithme split-window, afin d'analyser l'effet angulaire sur la SBT. En se basant sur une base de données de simulation, une méthode d'extraction de la SBT a été développée et appliquée aux observations à double angle de SLSTR. L'étude a ensuite examiné l'amplitude et les caractéristiques des différences de SBT entre les vues nadir et obliques, en tenant compte de facteurs tels que l'occupation du sol /la couverture terrestre, la saison, la latitude et le climat. Enfin, l'outil GeoDetector a été utilisé pour effectuer une analyse d'attribution des effets angulaires sur la SBT.

### Résumé en anglais

This study adopts SLSTR TIR data as the main data source and retrieves surface brightness temperature using split-window algorithm to analyze the angular effect of surface brightness temperature (SBT). Based on the simulation database, SBT retrieval method is developed and applied to SLSTR dual-angle SBT extraction. Then the magnitude and characteristics of SBT differences between nadir and oblique views were observed, considering factors such as land use/land cover, season, latitude and climate. Finally, GeoDetector tool was used to perform attribution analysis of SBT angular effects.